4th International Workshop on Photonics applied to Electromagnetic Measurements

PEM 2021

November 29–30, 2021 Online Workshop

Technical Digest

https://www.ieice.org/~pem/link/5_pem2021/pem2021.html

Sponsored by
Technical committee on Photonics-applied Electromagnetic Measurement

IEICE
Communications
Society

Workshop Outline

Dates:

November 29(Mon.)–30(Tue.), 2021 (online)

Major Topic Areas:

1. Basic theory/techniques related to PEM
2. Systems for PEM
3. Applications of PEM
4. Competitive/complementary technologies to PEM

Awards:

The PEM best paper award is given to researcher for outstanding contributed papers presented in the workshop. The student best presentation award is given to a student for outstanding contributed papers presented in the PEM workshop 2021.

Presentation Time (including discussion)**:**

Keynote Address: 45 min.

Invited Talk: 35 min.

Regular Talk: 20 min.

Sponsor:

Technical committee on Photonics-applied Electromagnetic Measurement, IEICE Communications Society

Website:

`https://www.ieice.org/~pem/link/5_pem2021/pem2021.html`

Workshop Committees

Workshop Chair: Teruo Onishi (NICT, Japan)

Local Steering Committee: Takashi Hikage (Hokkaido University, Japan)

Finance Chair: Akihisa Tsuchiya (KISTEC, Japan)

Secretaries: Yuto Shimizu (NICT, Japan)
Jun Katsuyama (Yokogawa Electric, Japan)

Technical Program Committee:
Ai-ichiro Sasaki (Chair, Kindai University, Japan)
Michitaka Ameya (AIST, Japan)
Junji Higashiyama (NTT DOCOMO, INC., Japan)
Atsushi Kanno (NICT, Japan)
Sven Kühn (IT'IS Foundation, ETH Zürich, Switzerland)
Dong-Joon Lee (KRISS, South Korea)
Shuji Taue (Kochi University of Technology, Japan)
Yusuf Nur Wijayanto (NICT, Japan)

Advisory Committee：
Qiang Chen (Tohoku University, Japan)
Satoru Kurokawa (AIST, Japan)
Niels Kuster (ETH Zürich, Switzerland)
Maya Mizuno (NICT, Japan)
Hiroshi Murata (Mie University, Japan)

Exhibitors:
７G aa Co. LTD.
ANRITSU CORPORATION
IEC TC103WG6 Japan National Committee
Restar Communications Corporation
TOYO MEDIC CO., LTD.

Keynote & Invited Speakers

Keynote Speaker: **Prof. Akira Hirose** (The University of Tokyo)

Akira Hirose received the Ph.D. degree in electronic engineering from the University of Tokyo in 1991. In 1987, he joined Research Center for Advanced Science and Technology (RCAST), the University of Tokyo, as Research Associate. In 1991, he was appointed Instructor at RCAST. From 1993 to 1995, on leave of absence from the University of Tokyo, he joined the Institute for Neuroinformatics, University of Bonn, Bonn, Germany. He is currently Professor with the Department of Electrical Engineering and Information Systems, the University of Tokyo. The main fields of his research interests are wireless electronics and neural networks. In the fields, he published several books such as Complex-Valued Neural Networks, 2nd Edition (Springer 2012), Complex-Valued Neural Networks: Theories and Applications, Ed. (World Scientific, 2003) and Complex-Valued Neural Networks: Advances and Applications, Ed. (IEEE Press / Wiley, 2013) and Reservoir Computing, (G.Tanaka, R.Nakane, A.Hirose) (in Japanese) (Morikita Publishing Co. Ltd., 2021).

Previously he served as Founding President of Asia-Pacific Neural Network Society (APNNS) (2016), President of Japanese Neural Network Society (JNNS) (2013-2015), Vice President of the IEICE Electronics Society (ES) (2013-2015), Editor-in-Chief of the IEICE Transactions on Electronics (2011-2012), Associate Editor of journals such as the IEEE TRANSACTIONS ON NEURAL NETWORKS (2009-2011), IEEE GEOSCIENCE AND REMOTE SENSING NEWSLETTER (2009-2012), Chair of the Neurocomputing Technical Group in the IEICE (2009-2010), IEEE GRSS All Japan Chapter Chair (2013-2015), IEEE CIS Tokyo Chapter Chair (2017-2018), and General Chair of IEEE International Geoscience and Remote Sensing Symposium (IGARSS) 2019 Yokohama, International Conference on Neural Information Processing (ICONIP) 2016 Kyoto and Asia-Pacific Conference on Synthetic Aperture Radar (APSAR) 2013 in Tsukuba. He currently serves as a member of IEEE Computational Intelligence Society (CIS) Neural Networks Technical Committee (NNTC) (2009-), Vice Chair of the NNTC Complex-Valued Neural Network Task Force (2021-) (Chair 2010-2020) and General Chair of IEEE World Congress on Computational Intelligence (WCCI) 2024 Yokohama.

Dr. Hirose is a Fellow of the IEEE and IEICE, and a member of JNNS, INNS and APNNS.

Invited Speaker: **Dr. Kyung Hyun Park** (ETRI)

Dr. Park is the director of Future & Basic Technology Research Division, ETRI. In 1996, he received his Ph. D in Physics from Yonsei University, Seoul, Korea. From 1996 to 1997, he worked on large scaled photonic integrated circuits in microelectronic science lab of Columbia University as a postdoctoral research fellow. From 1990 to 1999, he was with the Korea Institute of Science and Technology, Seoul Korea, as a member of research staff, where he was engaged in research on the functional photonic devices. Since 1999, he has joined the Electronics and Telecommunications Research Institute (ETRI), Daejeon, Korea, where he has been continuing his research on photonic devices. He was in charge of WDM photonic devices team and next generation photonic device team in ETRI. He demonstrated various photonic devices for the optical communications. He opened the terahertz photonics research center at ETRI, leading terahertz research for the past 10 years. His current focus is the pioneering of terahertz technology applications. He is a SPIE fellow and a member of the SPIE photonics west and advanced laser technology committees.

Invited Speaker: **Prof. Tetsuo Kobayashi** (Kyoto University)

Dr. Tetsuo Kobayashi was born in Hokkaido, Japan. He received his B.S, M.S. and Ph.D. degrees in electronic engineering in 1979, 1981 and 1984, respectively, all from Hokkaido University, Sapporo, Japan. In 1984–1992, he worked as an associate professor at Hokkaido Institute of Technology, Sapporo, Japan. In 1987–1988, he stayed at department of electrical engineering, University of Rochester, NY, USA as a visiting professor. In 1992, he moved to Hokkaido University, Sapporo, Japan as an associate professor of biomedical engineering. In 1996–1997, he stayed at Brain Behavior Laboratory, Simon Fraser University, BC, Canada as a visiting professor. Since 2004, he has been working as a full professor of biomedical engineering at Kyoto University, Kyoto, Japan.

He has been involved in the studies of MRI, Biomagnetism and Neuroimaging. His research interests also include Biomedical signal processing, Atomic Physics, and Cognitive Neuroscience. He is an author or co-author of more than 400 publications. In 2006, he started projects to develop super-sensitive optically pumped magnetometers and their biomagnetic applications.

At present, he is a councilor of International Society for Brain Electromagnetic Topography (ISBET), a councilor of Japanese Society of Biomagnetism, the past-Chair of the Japanese Chapter of International Society of Magnetic Resonance Imaging (ISMRM) and a Vice-President of Institute of Complex Medical Engineering (ICME). In addition, he is an editor of “International Journal of Magnetic Particle Imaging”. In 2018, he was awarded James Zimmerman Prize from International Federation of Medical and Biological Engineering (IFMBE) as the first Japanese winner of the Prize.

Invited Speaker: **Prof. Niels Kuster** (ETH Zürich)

Prof. Niels Kuster is the founder and Director of the Foundation for Research on Information Technologies in Society (IT’IS) in Zurich, Switzerland, and Associate Professor of the Department of Information Technology and Electrical Engineering at Swiss Federal Institute of Technology (ETH) in Zurich. His research covers many aspects of electromagnetics and computational life sciences, and focus, in particular, on the modeling of both internal and external physical factors that affect human physiology. These include electromagnetic fields (e.g. MR safety assessments), tissue heating and cooling (e.g. hyperthermia and ablation), acoustics in biology (e.g. focused ultrasound/pressure waves), biofluid dynamics (e.g. blood flow and aneurysm), biomechanics (e.g. bone, ligaments, and arterial walls), and dynamic tissue models (e.g. nerve models and tumor growth).

Prof. Kuster founded several spin-off companies to convert the most promising research results into high-quality commercial technologies, products, and services, and to provide researchers with a platform for innovative and productive research to develop and commercially exploit their knowledge. He has published over 200 peer-reviewed publications on measurement techniques, computational electromagnetics, dosimetry, exposure assessments, and bioexperimentation. He is a member of several standardization bodies and serves as a consultant on the safety of mobile communications for government agencies around the globe.

Invited Speaker: **Prof. Takanori Sato** (Hokkaido University)

Takanori Sato received his Ph.D. degree in the field of media and network technologies from Hokkaido University, Japan, in 2018. He was a Research Fellow of Japan Society for the Promotion of Science (JSPS) from 2017 to 2019. In 2019, he moved to University of Hyogo as an assistant professor. Since 2020, he has been an associate professor at Hokkaido University.

He has engaged in the study of optical communication and optical computing. His research interests also include the theoretical and numerical studies of optical fibers and photonic circuits using the coupled-mode theory and the finite element method. His now challenging topic is the analog radio-over-fiber (RoF) system based on the universal optical linear circuit for 6G. He is a member of the IEICE, JSAP, IEEE, and OSA. He is also a vice chair in IEEE Sapporo Young Professionals Affinity Group.

Invited Speaker: **Dr. Chao Wang** (University of Kent)

Chao Wang received his Ph.D. degree in Electrical and Computer Engineering from the University of Ottawa, Canada, in 2011. From 2011 to 2012, he was a Postdoctoral Fellow with the Photonics Laboratory, University of California at Los Angeles, Los Angeles, CA, USA. He is currently a Senior Lecturer at the School of Engineering, University of Kent, United Kingdom. His research interests include microwave photonics, ultrafast imaging and optical signal processing. He has authored over 100 papers in peer-review journals and leading international conferences.

Dr. Wang was the recipient of the NSERC Postdoctoral Fellowship, and the EU Marie-Curie Career Integration Grant award. He is an Associate Editor of IEEE Photonics Technology Letters. He is a Technical Program Committee (TPC) Co-Chair of the 2019 Optoelectronics Global Conference (OGC). He also served as a TPC member of 2017 and 2019 MWP conferences. He is a Chartered Engineer (CEng) by IET and a Fellow of Higher Education Academy (HEA), UK.

PEM 2021 Workshop Program

Monday, November 29, 2021

09:00 **Opening Remarks**

Teruo Onishi (National Institute of Information and Communications Technology)

Session 1 Nov. 29 (Mon.) 9:05–10:30

Chair: Teruo Onishi (NICT)

M-1 **[Keynote Address]**

09:05 **Physical Reservoir Computing for Sensor Network Society with Energy Efficient Intelligence --- The use of various spatiotemporal dynamics in wave nature ---**

Akira Hirose, Ryosho Nakane, Gouhei Tanaka (The University of Tokyo); Jean Benoit Heroux, Toshiyuki Yamane, Hidetoshi Numata, Daiju Nakano (IBM Research)

M-2 **[Regular Talk]**

09:50 **Intense Electromagnetic Pulse Measurements using an Electro-optic Probing System**

Dong-Joon Lee, Young-Pyo Hong (Korea Research Institute of Standards and Science); Hae-Jin Kwon (Hanwha Corporation); Kiho Kim (Agency for Defense Development)

M-3 **[Regular Talk]**

10:10 **Antenna Factor Measurement for Linear Polarized Electric-Field Sensor for 28 GHz Band of 5G**

Satoru Kurokawa (National Institute of Advanced Industrial Science and Technology); Sayaka Matsukawa (National Institute of Advanced Industrial Science and Technology and Mie University); Michitaka Ameya (National Institute of Advanced Industrial Science and Technology); Masahiro Sato, Masatoshi Onizawa (SEIKOH GIKEN Co., Ltd.); Hiroshi Murata (Mie University)

10:30–10:45 **Coffee break**

Session 2 Nov. 29 (Mon.) 10:45–12:00

Chair: Yusuf Nur Wijayanto (NICT)

M-4 **[Invited Talk]**

10:45 **Progress and Challenges Towards Continuous Wave Terahertz System for Field-Trials**

Kyung Hyun Park, Eui-Su Lee, Jun-Hwan Shin, Dong-Woo Park, Mugeon Kim, Da-Hye Choi, Younghoon Kim, Dong Hun Lee, JinChul Cho, Jungsoo Kim, Il-Min Lee (Electronics and Telecommunications Research Institute)

M-5 **[Regular Talk]**

11:20 **Investigation of Dielectric Property of Skin Tissue Phantom Added Glycerin Using Terahertz TDS**

Tetsuta Tomizawa (National Institute of Information and Communications Technology and Aoyama Gakuin University); Shota Yamazaki, Maya Mizuno (National Institute of Information and Communications Technology); Ryosuke Suga Osamu Hashimoto (Aoyama Gakuin University); Tomoaki Nagaoka (National Institute of Information and Communications Technology)

M-6 **[Regular Talk]**

11:40 **Calculation of Electromagnetic Field Distribution for Predicting Indoor 28 GHz Millimeter-Wave Propagation Characteristics in Residential House Environment**

Sango Nagamoto, Manabu Omiya (Hokkaido University)

12:00–13:30 **Lunch break**

Session 3 Nov. 29 (Mon.) 13:30–14:45

Chair: Ai-ichiro Sasaki (Kindai Univ.)

M-7 **[Invited Talk]**

13:30 **Development of Optically Pumped Atomic Magnetometers towards Next Generation Brain Imaging**

Tetsuo Kobayashi (Kyoto University)

M-8 **[Regular Talk]**

14:05 **Magnetic Domain Transition Applied to Electromagnetic Shielding and Measurements**

Tomoo Nakai (Industrial Technology Institute, Miyagi prefectural Government)

M-9 **[Regular Talk]**

14:25 **Uncertainty Evaluation of Optical Electric-Field Probe Calibration for Human Exposure Assessment at 85 kHz**

Yuto Shimizu (National Institute of Information and Communications Technology); Eishi Oho (National Institute of Information and Communications Technology, Tokyo University of Agriculture and Technology); Jerdvisanop Chakarothai, Tomoaki Nagaoka (National Institute of Information and Communications Technology); Takuji Arima, Toru Uno (Tokyo University of Agriculture and Technology)

14:45–15:00 **Coffee break**

Company Exhibition Nov. 29 (Mon.) 15:00–16:30

Chair: Akihisa Tsuchiya (KISTEC)

Tuesday, November 30, 2021

09:00 **Opening Remarks**
Takashi Hikage (Hokkaido University)

Session 4 Nov. 30 (Tue.) 9:05–10:20

Chair: Takashi Hikage (Hokkaido Univ.)

T-1 **[Invited Talk]**
09:05 **Reactive Near-Field Sensors: Requirements, Technology, and Applications**
Sven Kühn (Foundation for Research on Information Technologies in Society); Niels Kuster (Foundation for Research on Information Technologies in Society and ETH Zürich)

T-2 **[Regular Talk]**
09:40 **Fiber-Optic System for S-parameter Measurement of Electrically Small Antennas**
Sven Kühn (Foundation for Research on Information Technologies in Society); Beyhan Kochali (Schmid&Partner Engineering AG); Niels Kuster (Foundation for Research on Information Technologies in Society)

T-3 **[Regular Talk]**
10:00 **Alternative Cable to Antenna Gain Measurement System Using Optical Fiber Link Technologies**
Yuanfeng She, Michitaka Ameya, Satoru Kurokawa (National Institute of Advanced Industrial Science and Technology)

10:20–10:35 **Coffee break**

Session 5 Nov. 30 (Tue.) 10:35–11:55

Chair: Yuto Shimizu (NICT)

T-4 **[Regular Talk]**
10:35 **Electromagnetic Environment for a Wireless Medical Telemeter Due to Surrounding Walls**
Isao Kayano, Hisashi Miyazaki, Takakiyo Yamamoto, Naoki Takahashi (Kawasaki University of Medical Welfare); Aya Takayama (Kawasaki Medical School Hospital); Seiichi Mochizuki (Kawasaki University of Medical Welfare)

T-5 **[Regular Talk]**
10:55 **Exposure Polarization Dependency of Active Implantable Medical Device EMI in 5G Frequency Band**
Takuji Nishikawa, Atsuki Ohtsuka, Takashi Hikage, Manabu Yamamoto (Hokkaido University)

T-6 **[Regular Talk]**

11:15 **Characterization of Human Body Blockage in 5G Frequency Bands for Epidemiologic Research on Association Between Radio Frequency Wave Exposure and Children Health**

Kohei Yamamoto, Ryunosuke Ozaki, Takashi Hikage, Keiko Yamazaki, Atsuko Araki, Chihiro Miyashita, Naomi Tamura, Reiko Kishi (Hokkaido University)

T-7 **[Regular Talk]**

11:35 **Numerical Estimation of Indoor Propagation Characteristics Considering Shadowing due to Human Bodies in Local-5G Frequency Band**

Kazuki Yoshida, Takashi Hikage, Manabu, Yamamoto, Manabu Omiya (Hokkaido University)

11:55–13:30 **Lunch break**

Session 6 Nov. 30 (Tue.) 13:30–14:45

Chair: Jun Katsuyama (Yokogawa Electric)

T-8 **[Invited Talk]**

13:30 **Optical MIMO Signal Processing Based on Planar Lightwave Circuit**

Takanori Sato (Hokkaido University)

T-9 **[Regular Talk]**

14:05 **Binary Classification of Uplink-Channel States for Secure Body-Coupled Communication**

Akinori Ban, Ai-ichiro Sasaki (Kindai University)

T-10 **[Regular Talk]**

14:25 **Measurement of Reflected Microwave Guided-Mode Signal Propagating along FRPM Pipe-Wall Using Electro-Optic Sensor for Non-Destructive Remote Pipeline Inspection**

Kosuke Yoshida (Mie University); Sayaka Matsukawa (Mie University and National Institute of Advanced Industrial Science and Technology); Satoru Kurokawa (National Institute of Advanced Industrial Science and Technology); Tadahiro Okuda (Mie University and Kurimoto Ltd.); Masaya Hazama (Kurimoto Ltd.); Hiroshi Murata (Mie University)

14:45–15:00 **Coffee break**

Session 7 Nov. 30 (Tue.) 15:00–16:15

Chair: Atsushi Kanno (NICT)

T-11 **[Invited Talk]**

15:00 **Microwave Photonic Signal Processing Towards Remote RF Spectrum Sensing**

Chao Wang (University of Kent)

T-12 **[Regular Talk]**

15:35 **Millimeter-Wave D-band Antenna-Coupled Electrode Electro-Optic Modulator**

Shotaro Kodama, Takuto Mori, Yui Otagaki, Hiroshi Murata (Mie University)

T-13 **[Regular Talk]**

15:55 **28 GHz-Band Antenna-Coupled-Electrode Electro-Optic Modulator for Converting Two Orthogonal-Polarization Field Components Simultaneously for 5G Mobile Systems**

Yui Otagaki, Shunsuke Nakamori, Hiroto Yokohashi (Mie University); Sayaka Matsukawa (Mie University and National Institute of Advanced Industrial Science and Technology); Satoru Kurokawa (National Institute of Advanced Industrial Science and Technology); Masahiro Sato, Masatoshi Onizawa (SEIKOH GIKEN Co., Ltd.); Hiroshi Murata (Mie University)

16:15–16:45 **Coffee break**

Award Ceremony & Closing Remarks Nov. 30 (Tue.) 16:45–17:00

Company Exhibition Program

E-1 7G aa Co. LTD. (7th Generation in Automation and Antenna Measurement)

Satoru Kurokawa (7G aa Co.LTD.)

Abstract

7G aa is an AIST startup company. We can support your antenna measurements such as far-field antenna and near-field antenna measurements (IEEE 1720-2012 - IEEE Recommended Practice for Near-Field Antenna Measurements). We can provide a Radio over Fiber link system up to 40 GHz and an optical fiber ling microwave generator up to 100 GHz that is convenient for antenna measurement.

E-2 Recent Activities in IEC TC103 WG6

Satoru Kurokawa (AIST)

Abstract

IEC TC103 is the technical committee for the standardization of transmitting and receiving equipment for radiocommunication. Working Group 6 in this committee focuses on the radio over fibre (RoF) transceivers and provided the international standards and technical reports related to the specification of the transceivers, measurement methods, and RoF applications.

E-3 Unique solution for 5G mmW radio propagation

Takao Segawa (ANRITSU CORPORATION)

Abstract

Currently, 5G services have been launched and millimeter-wave services are planned in near future. In order to achieve stable communication, research on radio wave propagation is being conducted. This presentation will introduce a new solution to solve the problem of evaluating millimeter wave propagation.

E-4 Proposal of measuring probe and system using optical sensor

Kaoru Someno (Restar Communications Corporation)

Abstract

We introduce measuring instruments using optical sensors developed by Schmid & Partner Engineering AG. Products include TDS,OH4VNA, RFoF1P, SIM4LIFE Optics Solutions

E-5 Product overview of “Narda Safety Test solutions” for EMF Safety and RF Test measurement.

Yuki Usui (Toyo Medic Co., Ltd.)

Abstract

EMF Safety: SRM-3006, NBM-550/520, RadMan2, EHP-200A, EHP-50F, ELT-400

RF Test: SignalShark Real-Time Handheld Analyzer

[Keynote Address] Physical reservoir computing for sensor network society with energy efficient intelligence

The use of various spatiotemporal dynamics in wave nature

Akira Hirose[1*], Ryosho Nakane[1], Gouhei Tanaka[2], Jean Benoit Heroux[3],
Toshiyuki Yamane[3], Hidetoshi Numata[3], Daiju Nakano[3]
[1]Department of Electrical Eng. & Info. Sys., The University of Tokyo, Tokyo 113-8656, Japan
[2]International Research Center for Neurointelligence, The University of Tokyo, Tokyo 113-0033, Japan
[3]IBM Research - Tokyo, Kawasaki, Kanagawa 212-0032, Japan
*Corresponding author: ahirose@ee.t.u-tokyo.ac.jp

Abstract – This keynote speech focuses on physical reservoir computing, in particular on those utilizing spatiotemporal wave dynamics, such as optical waves and spin waves. They are expected to realize a low-power edge computing. They are also significant because of their intrinsic matching with the neural-network fundamentals. We discuss the physical and informational dynamics as well as the effectiveness in the near-future energy-efficient sensor-network society.

Keywords – Neural network hardware, edge computing

Keynote Summary

Reservoir computing attracts many researchers in these years [1-3]. It is a type of recurrent neural networks. Figure 1 illustrates the basic construction of a reservoir computing network. Reservoir is the recurrent part, and there the neural weights are fixed. Input signals results in an "echo," determined by neural nonlinearity and synaptic connection weights, which decays and vanishes in the end. The signals generated as reverberation are a set of signals transformed into a high dimensional information space, and they can be informationally rich. We can construct desirable time-serial signals from the readout of the reservoir neuron outputs by an adaptive weight-and-sum process. This output part does not include recurrence, resulting in a simple and fast learning.

One of the most important points in reservoir computing is the fact that it can be realized directly by physical phenomena [4]. Papers reported demonstrations, e.g., using a bucket filled with water [5] and soft matter [6]. Proposals aiming at practical computational devices include optical-wave [7-11] and spin-wave [12-19] devices. They utilize various spatiotemporal dynamics of the waves [20,21]. They will realize an extreme energy efficiency [22,23]. They also lead to an informational device framework perfectly consistent with neural network architecture [24].

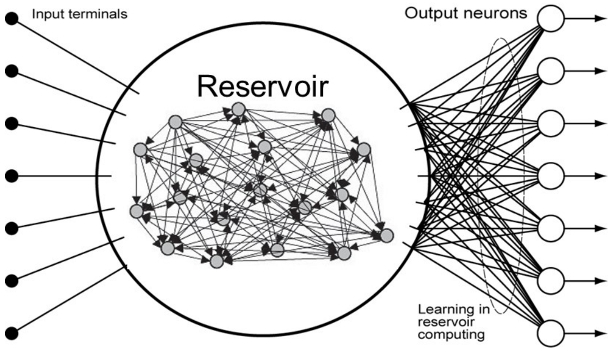

Figure 1. Basic construction of a reservoir computing neural network [22].

This keynote presents recent rise of physical reservoir computing and discusses the significance in the society.

Acknowledgement: This work was supported in part by the JSPS KAKENHI under Grant 18H04105, and in part by the New Energy and Industrial Technology Development Organization (NEDO) under Project JPNP16007.

References

[1] Jaeger, H. The "echo state" approach to analysing and training recurrent neural newtorks -- With an erratum note German National Research Center for Information Technology (GMD), 2001.

[2] Jaeger, H. & Haars, H. Harnessing Nonlinearity: Predicting Chaotic Systems and Saving Energy in Wireless Communication Science, 2004, 304, 78-80

[3] Maass, W.; Natschläger, T. & Markram, H. Real-time computing without stable states: A new framework for neural computation based on perturbations Neural Computation, 2002, 14, 2531-2560.

[4] Tanaka, G.; Yamane, T.; Héroux, J. B.; Nakane, R.; Kanazawa, N.; Takeda, S.; Numata, H.; Nakano, D. & Hirose, A. Recent Advances in Physical Reservoir Computing: A Review Neural Networks, 2019, 115, 100-123.

[5] Fernando, C. & Sojakka, S. Pattern Recognition in a Bucket Advances in Artificial Life, 2003, 588-597.

[6] Nakajima, K.; Hauser, H.; Li, T. & Pfeifer, R. Information processing via physical soft body Scientific Reports, 2015, 5, 10487.

[7] Shi, W.; Cao, J.; Zhang, Q.; Li, Y. & Xu, L. Edge Computing: Vision and Challenges IEEE Internet of Things Journal, 2016, 3, 637-646.

[8] Paquot, Y.; Duport, F.; Smerieri, A.; Dambre, J.; Schrauwen, B.; Haelterman, M. & Massar, S. Optoelectronic reservoir computing Scientific reports, Nature Publishing Group, 2012, 2, 287.

[9] Larger, L.; Soriano, M. C.; Brunner, D.; Appeltant, L.; Gutierrez, J. M.; Pesquera, L.; Mirasso, C. R. & Fischer, I. Photonic information processing beyond Turing: an optoelectronic implementation of reservoir computing Optics Express, 2012, 20, 3241-3249.

[10] Antonik, P.; Duport, F.; Smerieri, A.; Hermans, M.; Haelterman, M. & Massar, S. Online training of an opto-electronic reservoir computer International Conference on Neural Information Processing (ICONIP) 2015 Istanbul, 2015, 2, 233-240

[11] Héroux, J. B.; Numata, H.; Kanazawa, N. & Nakano, D. Delayed feedback reservoir computing with VCSEL International Joint Conference on Neural Networks (IJCNN) Rio de Janeiro, 2018, 594-602.

[12] Héroux, J. B.; Tanaka, G.; Yamane, T.; Kanazawa, N.; Nakane, R.; Numata, H.; Takeda, S. & Hirose, A. Time Delay Reservoir Computing with VCSEL International Conference on AI and Optical Data Sciences 2020, 2020, 11299, 1129908.

[13] Torrejon, J.; Riou, M.; Araujo, F. A.; Tsunegi, S.; Khalsa, G.; Querlioz, D.; Bortolotti, P.; Cros, V.; Yakushiji, K.; Fukushima, A.; Kubota, H.; Yuasa, S.; Stiles, M. D. & Grollier, J. Neuromorphic computing with nanoscale spintronic oscillators Nature, 2017, 547, 428-431.

[14] Furuta, T.; Fujii, K.; Nakajima, K.; Tsunegi, S.; Kubota, H.; Suzuki, Y. & Miwa, S. Macromagnetic Simulation for Reservoir Computing Utilizing Spin Dynamics in Magnetic Tunnel Junctions Phys. Rev. Applied, American Physical Society, 2018, 10, 034063

[15] Nakane, R.; Tanaka, G. & Hirose, A. Reservoir Computing With Spin Waves Excited in a Garnet Film IEEE Access, 2018, 6, 4462 - 4469.

[16] Nakane, R.; Tanaka, G. & Hirose, A. Demonstration of spin-wave-based reservoir computing for next-generation machine-learning devices International Conference on Magnetism (ICM) 2018 San Francisco, 2018, 26-27.

[17] Tsunegi, S.; Taniguchi, T.; Nakajima, K.; Miwa, S.; Yakushiji, K.; Fukushima, A.; Yuasa, S. & Kubota, H. Physical reservoir computing based on spin torque oscillator with forced synchronization Applied Physics Letters, American Institute of Physics, 2020, 114, 164101

[18] Nakane, R.; Tanaka, G. & Hirose, A. Numerical Analysis on Wave Dynamics in a Spin-Wave Reservoir for Machine Learning IEEE/INNS International Joint Conference on Neural Networks (IJCNN) 2019 Budapest, 2019.

[19] Ichimura, T.; Nakane, R.; Tanaka, G. & Hirose, A. A Numerical Exploration of Signal Detector Arrangement in a Spin-Wave Reservoir Computing Device IEEE Access, 2021, 9, 72637-72646

[20] Nakane, R.; Hirose, A. & Tanaka, G. Spin waves propagating through a stripe magnetic domain structure and their applications to reservoir computing Physical Review Research, 2021, 3, 033243.

[21] Yamane, T.; Katayama, Y.; Nakane, R.; Tanaka, G. & Nakano, D. Wave-Based Reservoir Computing by Synchronization of Coupled Oscillators International Conference on Neural Information Processing (ICONIP) 2015 Istanbul, 2015, 3, 198-205.

[22] Hirose, A.; Tanaka, G.; Takeda, S.; Yamane, T.; Numata, H.; Kanazawa, N.; Héroux, J. B.; Nakano, D. & Nakane, R. Proposal of carrier-wave reservoir computing International Conference on Neural Information Processing (ICONIP) 2018 Siem Reap, 2018, 616-624.

[23] Katayama, Y.; Yamane, T.; Nakano, D.; Nakane, R. & Tanaka, G. Wave-Based Neuromorphic Computing Framework for Brain-Like Energy Efficiency and Integration IEEE Transactions on Nanotechnology, 2016, 15, 762-769.

[24] Hirose, A.; Takeda, S.; Yamane, T.; Numata, H.; Kanazawa, N.; Héroux, J. B.; Nakano, D.; Nakane, R. & Tanaka, G. Physical reservoir computing: Possibility to resolve the inconsistency between neuro-AI principles and its hardware Australian Journal of Intelligent Information Processing Systems (AJIIPS) (Open Access ICONIP Proceedings), 2019, 16, 49-54.

Intense Electromagnetic Pulse Measurements using an Electro-optic Probing System

Dong-Joon Lee*[1], Young-Pyo Hong[1], Hae-Jin Kwon[2], and Kiho Kim[3]
[1]Division of Physical Metrology, Korea Research Institute of Standards and Science, 34113 Daejeon, Korea
[2]R&D Team2, Hanwha Corporation, 39370 Gumi, Korea
[3]The 1st R&D Institute, Agency For Defense Development, 34186 Daejeon, Korea

*Corresponding author: dongjoonlee@kriss.re.kr

Abstract – Intense electromagnetic pulses are measured with an electro-optic probing technique. Commercial and customized electro-optic probes are used to measure the transient electric fields generated from broad- and narrow-band pulse generators. Both generators yield results approximately on the kilovolt/meter field scale in the gigahertz range. The measured waveforms with each electro-optic probe are compared with those of a conventional D-dot sensor measurement method.

Keywords – electromagnetic pulse; electro-optic probe; waveform measurement; high power microwave

1. Introduction

The electro-optic (EO) sensing technique is a mature photonics-applied electromagnetic measurement technique. EO sensing has served as a breakthrough technology where conventional electrical probing becomes challenging. The electrical probes used with this method contain a good deal of metallic and electronic parts and are thus vulnerable during intense field measurements. The characteristics of the EO scheme enable us to overcome this challenge. EO probes are made of a dielectric material that is inherently immune to electricity, allowing minimally invasive field measurements without probe damage. We employ a commercially available EO probe and a custom-made probe. The dynamic range and bandwidth of the probe are evaluated by a calibration process. Each probe measures intense electromagnetic pulses and the results are compared with that of the conventional technique.

2. EO probing system and measurement

Fig.1 illustrates the basic principle of an EO probe for time-domain pulse measurements. It is basically a Mach-Zehnder (MZ) waveguide fabricated on an x-cut $LiNbO_3$ substrate. A periodic interdigitated electrode is installed symmetrically onto the Y-shaped waveguide, which is terminated with a highly reflective surface to form a folded MZ scheme [1].

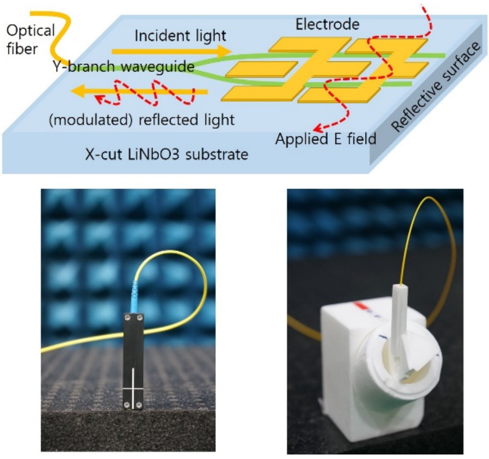

Figure 1. (a) Structure of the folded waveguide EO probe, and (b) commercial (left) and custom (right) EO probe

An interdigitated pattern is widely adapted where efficient electrodes are required in a limited area. When an external electric field is applied to a probe, these types of arrayed electrodes serve as an antenna that alters the optical length of each split waveguide path in the opposite direction. The shape, dimensions, and number of patterns used determine the efficiency of the electrode. Detailed information of our probe is to be covered in a separate paper.

To activate the EO probes, we implemented the probe control system presented in Fig. 2. Light from a Fabry-Perot laser diode with a wavelength of 1550 nm is delivered to the EO probe via a programmable polarization controller. The MZ waveguide probe is basically a polarizer; the probe’s performance strongly depends on the degree of incident polarization. Each probe has its own optimum incident polarization status, and this condition can be realized and maintained by means of real-time power monitoring with respect to the polarization control scheme used.

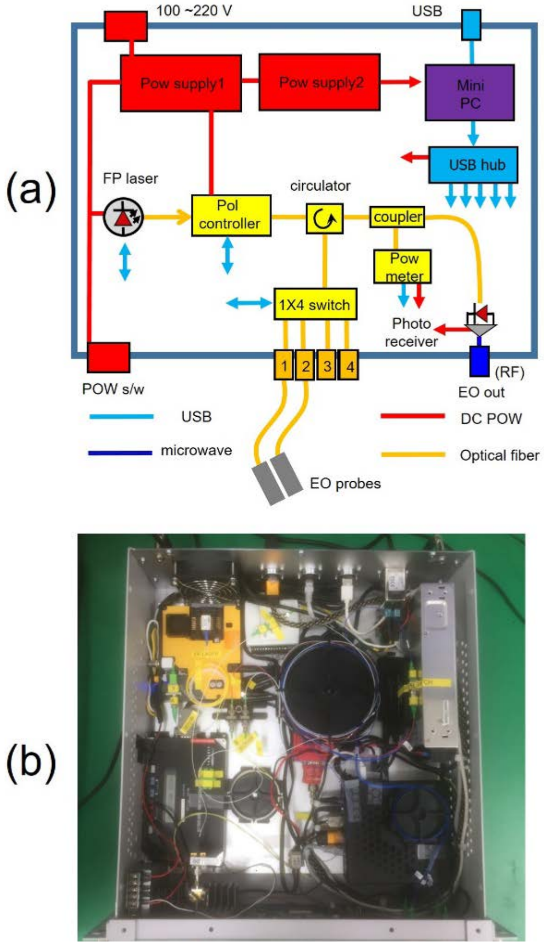

Figure 2. (a) Block diagram of the EO probe control system, and (b) implemented system

As the probe is exposed to an electric field, the incident light is modulated in accordance with the applied field. The modulated light is then reflected back to the control system and delivered to the photo receiver via a circulator. Finally, the photo receiver demodulates the sensing light and renders an electrical signal to a read-out instrument.

The performance of an EO probe can be evaluated by a calibration process. We placed our EO probe inside a TEM cell (model: CC-105SEXX) capable of generating a calculable electric field at an arbitrary strength [2]. The EO probe associated with the control system was set to the optimum condition for the best sensitivity. Fig. 3 (a) shows the field-calibrated EO signal with respect to the power applied to the TEM cell.

The signal was measured with a spectrum analyzer that detects minute signals below -100 dBm for a fairly enclosed environment such as a TEM cell. The signal emerges from the ~1 mV/m level and increases linearly to 7 V/m. A commercial probe (Seikoh-Giken: SH-10MS) is reported to be good up to 1 kV/m [3]. In fact, it was found here that the SH-10MS and the proposed probe (KRISS) were both good for kV/m scale measurements if adjusting the probe operation condition with a proper control system.

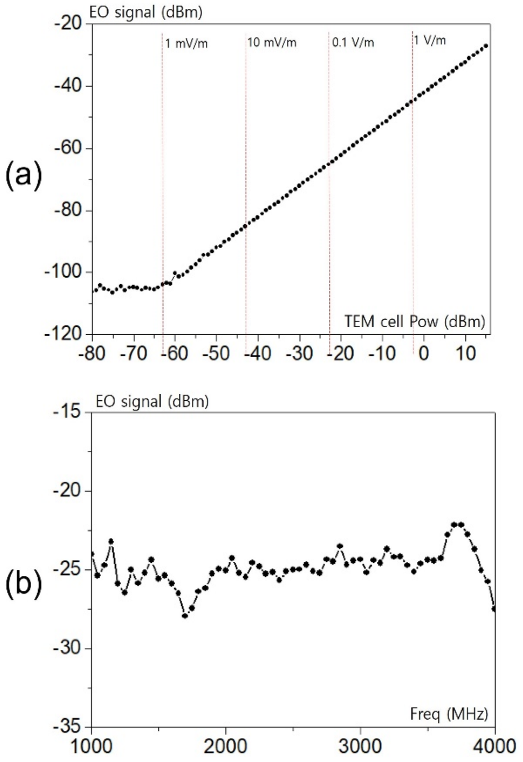

Figure 3. (a) Dynamic range of the KRISS EO probe, and (b) spectral response at the 10 V/m level

The spectral response is characterized in an anechoic chamber. A standard horn antenna generates an electric field of 10 V/m in the 1 GHz – 4 GHz range. The 10 V/m field was confirmed with a commercial field probe (Amplifier Research: FL7018). Because the EO probe scarcely interacts with the field probe, it was mounted onto the field probe apex during the calibration process.

Our EO probe (KRISS) can measure a weak electric field as low as < 10 mV/m up to a bandwidth of 4 GHz. The commercial probe (SH-10MS) used here is reported to have comparable sensitivity with a wider bandwidth up to 10 GHz [3]. Such low field sensing is feasible for frequency-domain sensing with a spectrum analyzer.

In case time-domain sensing is preferred, the field level must exceed approximately 10 V/m in order to be observed through a real-time oscilloscope. Most high-power pulse generators for military applications operate at least on the kV/m scale of field strength. Although a transient signal at such level can be readily detected with an oscilloscope, the signal waveforms tend to be distorted. This occurs because light modulation with respect to the applied field at the probe becomes non-linear beyond a certain field strength value.

The MZ-style probes utilize interferometric patterns, which can be manipulated with a probe controller. The operation bias points are set within the linear region of the fringe patterns. While linear modulation is attained at low or moderate field strength levels, the linearity begins to degrade beyond a ‘moderate level’. Thus, it is crucial to find the moderate level and operate the probe below that level to avoid non-linearity.

The MZ-style EO probes also work as polarizers. Their transmission along the optical waveguide on a $LiNbO_3$ wafer heavily depends on the status of polarization. For an x-cut $LiNbO_3$ wafer, the transmission is maximized as the incident polarization is set along the extra-ordinary axis. This means that the ‘probe quality’ can be manipulated with polarization. By reducing the polarization component along the extra-ordinary axis, the reflected light from the waveguide probe is diminished, resulting in lower sensitivity. The polarization status can be controlled and indirectly monitored by a polarization controller and with coupled power, as shown in Fig. 2.

We measured broadband pulses from a high-power generator. First, we measured the pulses with a D-dot sensor, with the result being a pear-to-peak field of 6.2 kV/m 4.2 meters away from the generator. The typical rise time and duration of the bipolar pulses are 100 – 120 ps and ~1 ns, respectively.

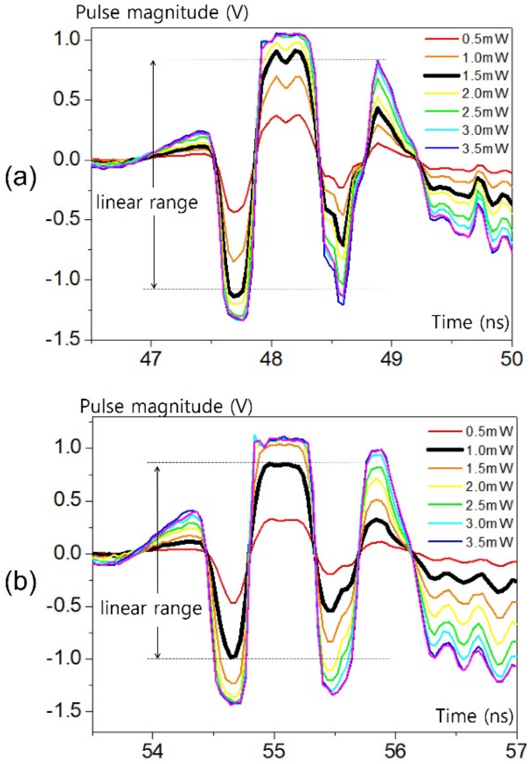

Figure 4. Measured pulses with various polarization conditions: (a) with a commercial probe, and (b) with the KRISS probe (Each pulse is an average of 30 time measurements.)

Fig. 4(a) shows the pulses measured with a commercial probe (SH-10MS). We controlled the incident polarization state by adjusting the reflected power from the probe to the photo receiver in a range of 0.5 mW to 3.5 mW in 0.5 mW steps. The commercial probe shows typical polarization dependency for an optical waveguide fabricated by a proton-exchange technique. As shown in Fig. 4(a), the pulse waveform grows as the power level is increased. However, the waveform does not linearly follow the power increase beyond a certain level, 1.5 mW in this case. This means that

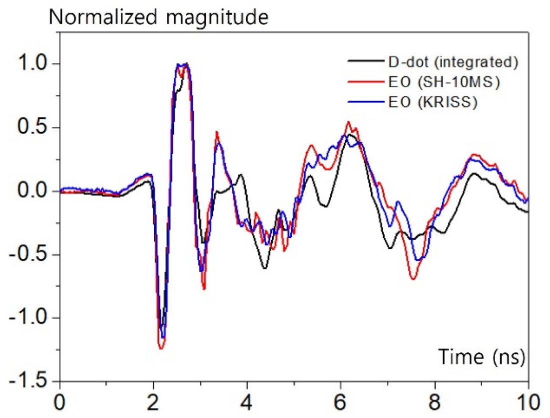

Figure 5. Comparison of broadband pulses measured with three probes

the incident polarization must be managed so that it has reflected power within the linear modulation range of the probe. We iterated the pulse measurement with the custom-made (KRISS) probe, as shown in Fig. 4(b). The KRISS probe shows non-linearity over 1 mW.

To compare this proposed EO probing technique with a conventional D-dot sensor(Prodyn:AD-80), the two waveforms previously measured with each EO probe (black lines in Fig. 4) and the D-dot sensor are normalized and overlapped in the same time window for comparison. The primary bipolar pulse is most important for broadband high-power applications. All three measurements are found to be within the pulse specifications (rise time: 100 – 120 ps, duration: 1 ns).

The proposed EO technique can also be applied to measure narrow-band pulses. Our pulse source generates 1 MW of power at 3 GHz with a 1μs duration [4]. We placed the three probes used in Fig. 5 where a field level of approximately 4 – 6 kV/m is expected.

Fig. 6 presents the narrow-band pulse measurements with the three probes. The entire pulse envelope is displayed on top of oscilloscope screen shot. The pulse set is measured with a D-dot and an EO probe. (The integrated D-dot resembles the D-dot result because the pulse is filled with a sinusoidal carrier.) The 3 GHz carrier components measured with the D-dot and EO probe are displayed in the 4 ns window below the envelope.

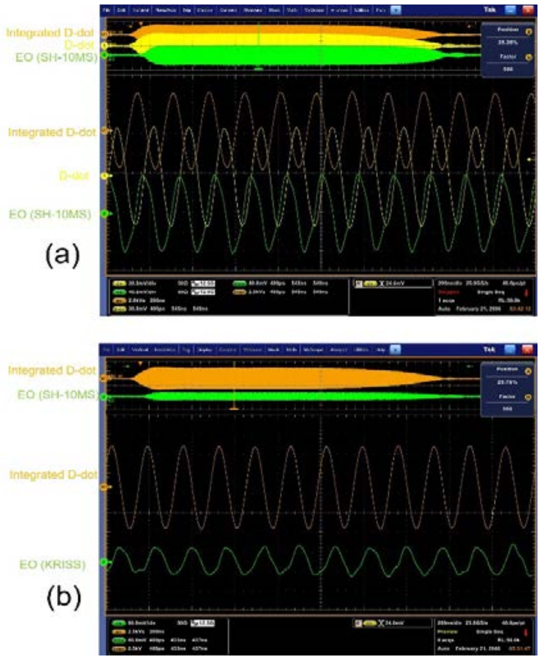

Figure 6. Comparison of narrow-band pulses measured with three probes: (a) D-dot vs SH-10MS, and (b) D-dot vs KRISS

3. Conclusion

We have demonstrated that an EO probing technique can be applied to intense electromagnetic pulse measurements on the kV/m and GHz scales. The performance of the proposed method was compared with that of a conventional method and showed comparable results. The advantages of the photonics-applied electromagnetic measurement technique introduced here over the conventional approach are to be discussed in a conference presentation.

Acknowledgement

This work was supported by Institute of Information & communications Technology Planning & Evaluation (IITP) grant funded by the Korea government(MSIT) (No.2021-0-00228, Development of measurement system for electromagnetic exposure to human base on electro-optic(EO) sensor at 100 GHz band)

References

[1] Zeng R, Wang B, Niu B, Yu Z. Development and Application of Integrated Optical Sensors for Intense E-field Measurements. Sensors. 2012; 12: 11406–11434.

[2] Lu H, Li Y, Zhang J. Design and Analysis of a Broadband LiNbO3 Optical Waveguide Electric Field Sensor with a Tapered Antenna. Sensors. 2021; 21: 3672–3685.

[3] https://www.seikoh-giken.co.jp/en/products/pdf/mix4_05.pdf

[4] Kim J, Cha S, Yoon Y, Ryu J, Choi J. Analysis of the Transient Radiation Pattern of a High-Power Bipolar Short-Pulsed Array Antenna. IET Microwaves, Antennas & Propagation. 2017; 11(14): 2043–2048.

Antenna Factor Measurement for Linear Polarized Electric-Field Sensor for 28 GHz Band of 5G

Satoru KUROKAWA[1*], Sayaka MATSUKAWA[1,3], Michitaka AMEYA[1], Masahiro SATO[2],
Masatoshi ONIZAWA[2] and Hiroshi MURATA[3]

[1] National Metrology Institute of Japan, National Institute of Advanced Industrial Science and Technology, 305-8563, Tsukuba, Ibaraki, Japan
[2] Seiko Giken Co., LTD, 270-2214. Matsuda, Chiba, Japan
[3] Institution Name Graduate School of Engineering, Mie University, 514-8507, Tsu, Mie, Japan
* satoru-kurokawa@aist.go.jp

Abstract – We have estimated a far field antenna factor of an antenna-coupled-electrode electric-field sensor system for 28 GHz-band using an amplitude center modified Friis transmission formular. Estimated far field antenna factor of the electric field sensor system is 68.4 dB/m to 76.1 dB/m for the frequency range from 27 GHz to 30 GHz.

Keywords – Electric field sensor, 5th generation mobile communication, antenna factor, Friis transmission formular, Amplitude center

1. Introduction

5th generation mobile communication (5G) uses 28 GHz band in Japan. In the case of using an electric field sensor for estimating the electric field intensity, we use a far field antenna factor for the electric field sensor. We have already developed an antenna coupled electrode electric field sensor for 28 GHz band as an electric-field sensor (EO sensor) [1]. For estimating the far field antenna factor for an antenna under test, we have already proposed an amplitude center modified Friis transmission formula [2]. In the case of using the formula, we can estimate the far-field antenna factor of the antenna under test at the near distance.

In this paper, we have newly estimated the far-field antenna factor of the EO sensor using the amplitude center modified Friis transmission formula. The amplitude center modified Friis transmission formula is first explained. Next, the estimated far field antenna factor for the EO sensor system is explained.

2. Amplitude center modified antenna factor equation

In order to estimate the antenna factor at near antenna distance, two antennas are set face to face and same polarization in antenna distance=z. In the case of using amplitude center location, frequency domain receiving signal $s_{21}(\omega,z)$ is shown equation (1) as

$$|s_{21}(\omega,z)| = \frac{\eta_0 \cdot k_0}{Z_0} \frac{1}{af_{t\_\mathrm{far}}(\omega)} \frac{1}{af_{r\_\mathrm{far}}(\omega)} \frac{1}{z+d_1(\omega)+d_2(\omega)} \quad (1)$$

where $af_{\mathrm{t\_far}}(\omega)$ and $af_{\mathrm{r\_far}}(\omega)$ are the far field antenna factors of the transmitting and receiving antennas, respectively. $d_1(\omega)$ and $d_2(\omega)$ are the distance from the aperture to the amplitude center of the transmitting and receiving antennas, respectively. In the case of antenna distances between transmitting and receiving antenna are $z = z_1$ and z_2, measured frequency responses are $s_{21}(\omega,z_1)$ and $s_{21}(\omega,z_2)$, the far field antenna factors can be estimated the following equation,

$$af_{\mathrm{t\_far}}(\omega) \cdot af_{\mathrm{r\_far}}(\omega) = \frac{\eta_0 \cdot k_0}{Z_0} \left(\frac{1}{|s_{21}(\omega,z_1)|} - \frac{1}{|s_{21}(\omega,z_2)|} \right) \frac{1}{z_1 - z_2} \quad (2)$$

In the case of using the transmitting antenna factor $af_{\mathrm{t\_far}}(\omega)$, we can estimate the far field antenna factor for the receiving antenna $af_{\mathrm{r\_far}}(\omega)$ using the equation (2). For estimating the antenna factor of the EO sensor, we can use a calibrated WR-28 standard gain horn antenna as a transmitting antenna.

3. Antenna factor measurement for the EO sensor

A. *Basic structure of the EO sensor*

The basic structure of the EO sensor is shown in Figure 1. The EO sensor is fabricated on a z-cut LiNbO$_3$ film about 50 μm thickness that is stacked on a base substrate of SiO$_2$ glass about 250 μm thickness. Two square patch antennas as a receiving antenna are connected to a standing-wave resonant electrode by use of micro-strip feeding lines to form an antenna-coupled electrode on the EO sensor. An optical waveguide as a phase modulator is fabricated on the reverse side of the LiNbO3 film. Along the optical waveguide, two antenna-coupled electrodes for a single polarized receiving signal are aligned to form an array antenna. Size of our developed EO modulator with plastic case and absorbing material for back side is radius R=10 cm x thickness=10 mm. Figure 2 shows the photo of the EO sensor.

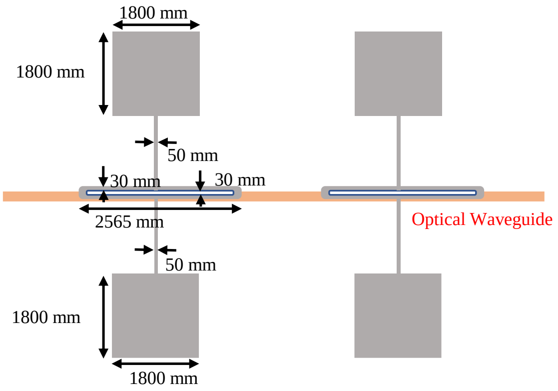

Figure 1. Structure of the antenna coupled electrode electro optic modulator.

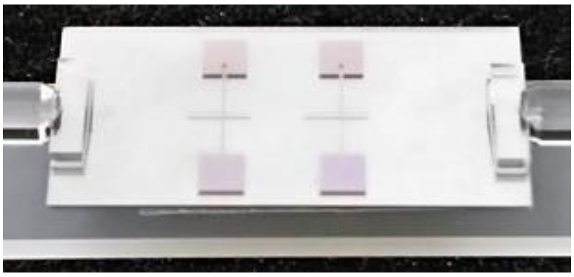

Figure 2. Photo of the antenna coupled electrode electro optic modulator.

B. *Measurment setup for the antenna factor measurement of the EO sensor*

In order to measure the antenna factor of the EO sensor, antenna distance between a aperture of a WR-28 standard gain horn antenna as a transmitting antenna and a EO sensor as a receiving antenna set z = 10 cm to 150 cm every 10 cm. Fig. 3 shows the antenna factor measurement setup. For estimating the antenna factor of the EO sensor, we use the calibrated far field antenna factor of the WR-28 standard gain horn antenna for the equation (2). Figure 4 shows measured $S_{21}(\omega, z)$s after removing the ambient reflection waves.

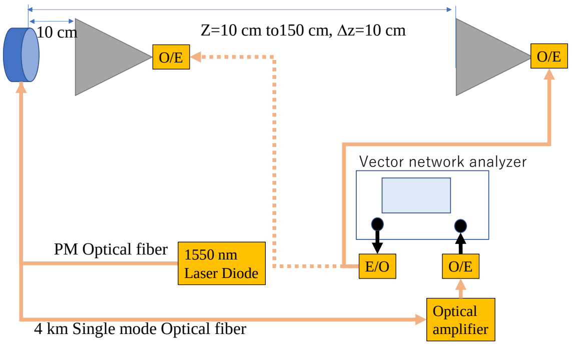

Figure 3. Antenna factor measurement setup for the EO sensor.

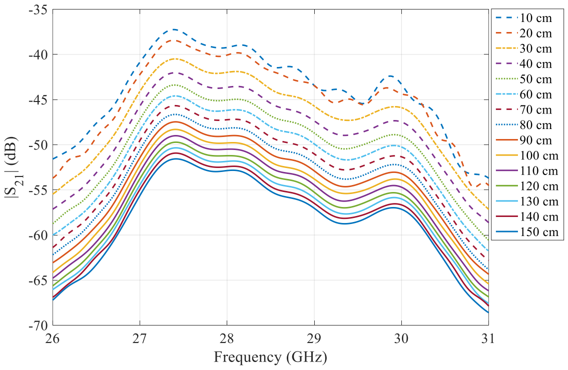

Figure 4. Measured $S_{21}(\omega,z)$s after removing the ambient reflection waves.

C. *Measurment setup for the antenna factor measurement of the EO sensor*

After measuring the $S_{21}(\omega,z)$s, we can estimate the far field antenna factor of the EO sensor using the equation (2). Figure 5. shows the estimated far field antenna factors of the EO sensor system using the measured $S_{21}(\omega,z)$s of z= 50 cm and 140 cm for the equation (2). The estimated antenna factor of the EO sensor is 68.4 dB/m to 76.1 dB/m for the frequency range from 27 GHz to 30 GHz. Figure 6. shows the difference of antenna factors between using the measured $S_{21}(\omega,z)$s of z= 50 cm, 140 cm and z= 50 cm, z_2 cm (z_2=60, 70, 80, 90, 100, 110, 120, 130 cm). These results show the fact that we can estimate the antenna factor using the measured $S_{21}(\omega,z)$s of z= 50 cm, 70 cm for the equation (2) within 0.3 dB difference for the antenna factor of the EO sensor using the measured $S_{21}(\omega,z)$s of z= 50 cm, 140 cm.

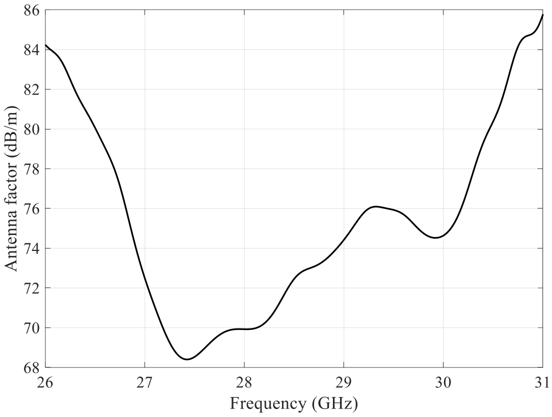

Figure 5. Estimated far field antenna factor of the EO sensor using the measured $S_{21}(\omega,z)$s of z= 50 cm and 140 cm for the equation (2).

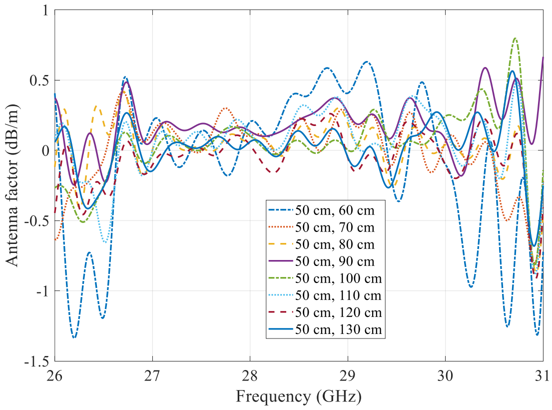

Figure 6. Difference of antenna factors between using the measured $S_{21}(\omega,z)$s of z= 50 cm, 140 cm and z= 50 cm, z_2 cm (z_2=60, 70, 80, 90, 100, 110, 120, 130 cm).

4. Conclusions

We have shown our newly estimated the far field antenna factor of the linear polarized antenna coupled electrode electro optic modulator for the 28 GHz frequency band of 5th generation mobile communication using the amplitude center modified Friis transmission formula. The estimated far field antenna factor of the EO sensor is 68.4 dB/m to 76.1 dB/m for the frequency range from 27 GHz to 30 GHz. Further, we have shown that the far field antenna factor of the EO sensor can estimate using the measured $S_{21}(\omega,z)$s of z= 50 cm, 70 cm for the equation (2) within 0.3 dB difference for the antenna factor of the EO sensor using the measured $S_{21}(\omega,z)$s of z= 50 cm, 140 cm.

References

[1] S. Kurokawa, S. Matsukawa, H. Murata, et. al. “Receiving Performance of Antenna-Coupled Electrode Electro-Optic Modulators for 5G Frequency Band,” in Proc. of IEEE2019CAMA, Oct. 2019.

[2] S. Kurokawa, M. Ameya, and M. Hirose, “Far filed gain estimation method for Japanese broadband antenna standard using time-frequency analysis,” in Proc. PIERS 2013, Stockholm, Sweden, Aug. 12-15, 2013, pp. 838-842

[Invited Talk] Progress and Challengs Towards Continuous Wave Terahertz System for Field-Trials

Kyung Hyun Park[1*], Eui-Su Lee[1], Jun-Hwan Shin[1], Dong-Woo Park[1], Mugeon Kim[1], Da-Hye Choi[1], Younghoon Kim[1], Dong Hun Lee[2], JinChul Cho[1], Jungsoo Kim[1] and Il-Min Lee[1]

[1]Future & Basic Technology Research Division, Electronics and Telecommunications Research Institute (ETRI),
34129 Daejeon, KOREA
[2]Photonics/Wireless Devices Research Division, Electronics and Telecommunications Research Institute (ETRI)
34129 Daejeon, KOREA
* khp@etri.re.kr

Abstract – The continuously increasing interest on the continuous-wave (CW) terahertz (THz) technologies in recent years is based on their potential in a wide variety of applications such as wireless communications, spectroscopy, sensing, and imaging. For the wide adoptions of the THz technologies to the industry, the importance of highly-efficient and compact THz module with a reasonable cost has been growing. Since the optimized performance of a THz module depends not only on the device itself but also on the configuration of a module, various approaches have been investigated to implement high-performance THz platforms as the main building blocks of a THz system. WE believe that the bright future of THz systems is envisaged by the compact and cost-effective photonics technologies.

Keywords – Terahertz imaging, Terahertz communication, Terahertz nondestructive evaluation. Terahertz electronics, Terahertz photonics.

1. Introduction

Terahertz (THz) technologies have attracted great interest in their possibilities over a wide variety of industrial applications such as wireless communications, spectroscopy, and imaging. According to one of the recent market forecasting reports, the market of the terahertz components and systems will grow dramatically in the approaching decades [1]. Although terahertz time-domain spectroscopy (THz-TDS) has demonstrated possibilities of THz technology [2], the widespread industrial application has been hampered by the obstructions in their price, size, and measurement speed. Consequently, compact and low-cost THz devices are getting more important to the wide fields of applications. Thanks to the last 10 years of efforts to develop cost-effective and easy-to-use systems, we envisage the industrial applications of THz technologies.

For the last few years, we have developed and enhanced monolithically-integrated single cavity dual-mode laser (DML) which ensures co-polarized, collinear and independently tunable dual-mode emission from a single laser chip, which significantly simplifies the optical alignment and reduces the required number of components [3]. Besides, we have proposed several different types of photomixers including low-temperature grown (LTG) GaAs photomixers, evanescently coupled waveguide photodiodes (ECPDs) and uni-traveling-carrier photo-diodes (UTC-PDs). Since the optimized performance of a module depends not only on the characteristics of the device itself but also on the configuration, various approaches have been investigated to implement high-performance modules as the THz platform and as the main building blocks of a THz system. Based on our THz continuous wave (CW) components, we have developed several systems including THz thickness measurement systems [4], transmission or reflection types of THz scanning imaging systems, THz spectroscopic systems, and their hybrids.

In this study, our recent studies in the field of CW THz systems based on photonics technologies including beating sources, THz generating and detecting devices [5-6] and their industrial applications such as THz imaging, THz wireless communications and THz spectroscopic measurements will be briefly reviewed.

2. Wireless THz link with photonics based Transmitter and receiver

In Korea, from this year, government-funded research projects to develop the key technologies of B5G (Beyond fifth-generations) or namely 6G (sixth-generations) have been launched. For the THz communications, electronics-based and photonics-based THz devices are in some kind of competition to become the leading technology. Photonics-based THz technologies have the advantageous feature that they can be natural or easier in providing a transparent connection to the fiber-optic links and providing the broadband and high-speed wireless links. With an aim of developing the whole devices for the photonics-based THz link frontend, we are developing the consisting devices such as the direct-modulating ridge waveguide type dual-mode laser (DM-rDML) as a tunable optical beating source, the uni-traveling-carrier photodiode (UTC-PD) as a THz emitting device, and the Schottky barrier diode (SBD)-based subharmonic mixer (SHM) as a THz receiver. Main components for THz wireless link are shown in Fig. 1.

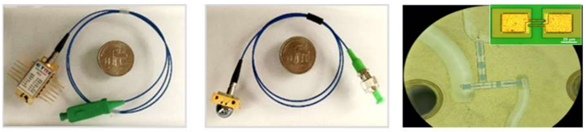

(a) (b) (c)

Figure 1. Fabricated terahertz modules for THz wireless link. (a) Dual-mode laser module (b)PM fiber pigtailed UTC-PD module (c) anti-parallel SBD chip and submount circuit for SHM

Using our devices such as UTC-PD as the THz emitter and the SBD SHM as the THz receiver, we have demonstrated a 50 Gbps THz transmissions over 2 m distance.

3. THz Imaging System for applications

Non-destructive terahertz (THz) imaging technology is highly promising in several industrial applications such as process monitoring, quality control and technical diagnostics [7-8]. However, still the commercially available THz cameras are either too expensive or not sufficient to the industrial applications. In particular, owing to the high noise equivalent power of the commercial THz camera compared to single detector in the range of a few hundred of gigahertz, the use of emitters based on photomixing as THz generators with a low output power, is difficult. Consequently, the application of the THz imaging technology to the industrial domain encounters several challenges such as the measurement time, system cost, and system size.

To overcome these issues, we developed a novel 2D scanner with a single detector and emitter, which has a higher speed and is more cost effective than the existing system. Fig. 2 shows the performance of our own developed THz imaging system.

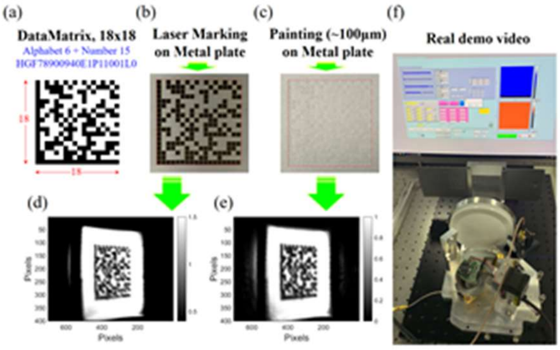

Figure 2. Demonstration of the THz tagging system. (a) Data matrix code of 18 × 18. (b) Sample A: laser marked metal plate. (c) Sample B: laser marked and painted metal plate. (d),(e) Measured THz images of Samples A and B. (f) Real demo video of Sample B.

4. Summary

The photonic technologies for the THz devices and systems to realize the industrial applications of the THz technologies can open the real opportunities in the industry because their unique strength in implementing small, compact, and cost-effectiveness. We are expecting our technology can find our unique way of applications such as the non-destructive evaluations in a mass-production lines, THz sensing in public places, and high-speed wireless communications for the connections of device-to-device.

References

[1] A. McWilliams, Terahertz Radiation Systems: Technologies and Global Markets (BCC Research, 2015).

[2] P.U. Jepen, D. G. Cooke, M. Koch. Terahertz Spectroscopy and Imaging – Modern techniques and applications. Laser Photon. Rev. 2011; 5: 124–166.

[3] N. Kim, J. Shin, E. Sim, C. W. Lee, D.-S. Yee, M. Y. Jeon, Y. Jang, and K. H. Park. Monolithic dual-mode distributed feedback semiconductor laser for tunable continuous-wave terahertz generation. Opt. Express 2009; 17: 13851–13859.

[4] I.-M. Lee, N. Kim, E. S. Lee, S.-P. Han, K. Moon, K. H. Park. Frequency modulation based continuous-wave terahertz homodyne system. Opt. Express 2015; 23: 846-858.

[5] S.-P. Han, H. Ko, N.Kim, W-H.. Lee, K. Moon, I.-M. Min Lee, E. S. Lee, D. H. Lee, Wangjoo Lee, S.-T. Han, S.-W. Choi, K. H. Park. Real-time continuous-wave terahertz line scanner based on a compact 1 × 240 InGaAs Schottky barrier diode array detector. Optics Express 2014; 22: 28977-28983.

[6] Jun-Hwan Shin, Dong Woo Park, Eui Su Lee, Mugeon Kim, Dong Hun Lee, Il-Min Lee, Kyung Hyun Park. Highly reliable THz hermetic detector based on InGaAs/InP Schottky barrier diode. Infraed Phys. &Technol. 2021; 115: 103736.

[7] Eui Su Lee et al., “Semiconductor-Based Terahertz Photonics for Industrial Applications,” IEEE J. Lightwave Technol., 2018; 36(2): 274-284.

[8] Eui Su Lee et al., “High-Speed and Cost-Effective Reflective Terahertz Imaging System Using a Novel 2D Beam Scanner, IEEE J. Lightwave Technol., 2020; 38(16): 4237-4243.

Investigation of Dielectric Property of Skin Tissue Phantom Added Glycerin Using Terahertz TDS

Tetsuta Tomizawa[1,2*], Shota Yamazaki[1], Maya Mizuno[1]
Ryosuke Suga[2], Osamu Hashimoto[2], Tomoaki Nagaoka[1]
[1]Radio Research Institute, National Institute of Information and Communications Technology, Tokyo 184-8795, Japan
[2]Department of Electrical and Electronic Engineering, Aoyama Gakuin University, Kanagawa 252-5258, Japan
*Corresponding author: tomizawa@ee.aoyama.ac.jp

Abstract – The dielectric properties of skin tissue phantoms with glycerin concentrations from 0% to 60% were investigated in a terahertz region. Their complex relative permittivities were measured by the terahertz time-domain spectrometer between 0.1 THz and 0.8 THz. The complex relative permittivities decreased with the increase of the glycerin concentration. On the basis of the property it was found out that the permittivities of the phantom with 35% glycerin were close to that of skin.

Keywords – terahertz; phantom; time-domain spectroscopy; glycerin

1. Introduction

In recent years, terahertz (THz) technologies over 0.1 THz are emerging for higher speed wireless communications [1], [2]. For this practical use, it is necessary to study the thermal effect of THz waves in body surface tissues such as skin and eyes, and to evaluate an exposure condition and a temperature elevation in the tissue using a phantom that has the complex relative permittivities similar to those of the tissue. In previous research, the skin tissue phantom for frequencies below 0.1 THz was developed [3].

In this study for the frequencies over 0.1 THz, the phantoms were prepared using ultrapure water, glycerin, and agar as in the case of below 0.1 THz. Since the complex relative permittivity of the tissue depends on the frequency, the value of the phantom must be changed. Therefore, the phantoms added glycerin with various concentrations were prepared and their complex relative permittivities were measured to find out a glycerin concentration suitable for the development of the skin tissue phantom.

2. Mesurement system

Figure 1 shows the appearance of the THz Time-Domain Spectrometer (TDS) system (TAS7500TS, ADVANTEST). A bowtie-type photoconductive antenna (PCA) and a dipole-type PCA were used as the THz emitter and receiver, respectively. Using an attenuated total reflection (ATR)-type of the THz-TDS, the complex relative permittivities of phantoms were measured in the frequency range from 0.1 THz to 0.8 THz.

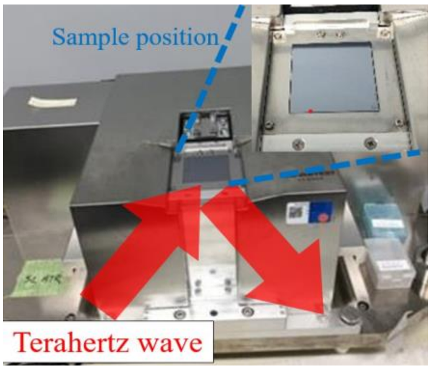

Figure 1. Appearance of THz-TDS

3. Tissue phantom specimens

The phantoms were composed of ultrapure water, glycerin, and agar. The materials are well used for producing the phantom in a GHz region [4]. Specimens with six different glycerin concentrations were prepared as listed in Table 1.

The ultrapure water and glycerin were dispensed by micropipette and mixed in a beaker glass. Then, 1.5% agar was added and stirred well using a spatula. The beaker glass was wrapped, and the solution was heated up to 100°C by a microwave oven at 500 W and then was stirred. This process was continued until the agar was completely dissolved (approximately 3 times). After its temperature returned to approximately 45°C with stirring, the solution was poured into a cube mold and left at 23°C for 30 minutes.

Table 1. Materials of tissue phantom and their concentration

Material	Concentration					
Ultrapure water (%)	98.5	78.5	68.5	58.5	48.5	38.5
Glycerin (%)	0	20	30	40	50	60
Agar (%)	1.5					

4. Measurement results and discussion

Figures 2 and 3 show the real and imaginary parts of the complex relative permittivities of the phantoms measured 9 averaged. As shown in those figures, they were gradually decreased with the increase of the glycerin concentration and frequency. Figure 4 shows the complex relative permittivity versus glycerin concentration at frequency 0.28 THz as an example. Here, means and 95% confidence intervals (error bars) of 9 measurements were represented. The error bars were below 5%. The dotted lines indicate the approximate straight lines. The relative permittivities of the human skin (5.0 -j3.3) are indicated by dashed lines as a reference [5]. The phantom permittivities with approximately 35% glycerin are close to the reference values. The phantom with 35% glycerin was therefore prepared and measured additionally. The measurement result indicated that the suitable glycerin concentration could be predicted by the linear approximation.

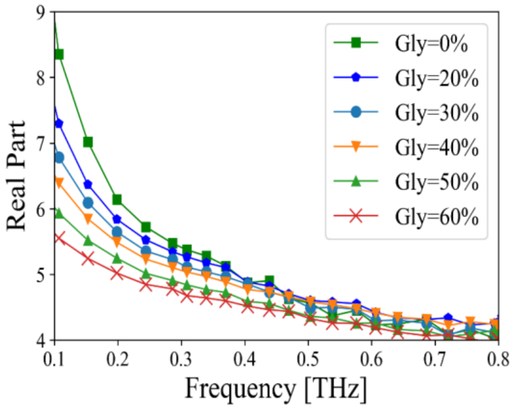

Figure 2. Real part data of complex relative permittivity of phantoms produced at different concentrations of glycerin.

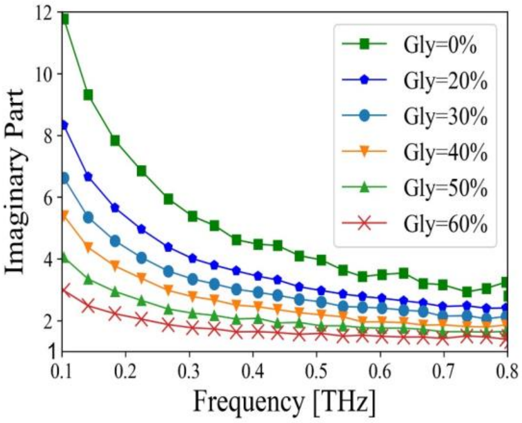

Figure 3. Imaginary part data of the complex relative permittivity of phantoms produced at different concentrations of glycerin.

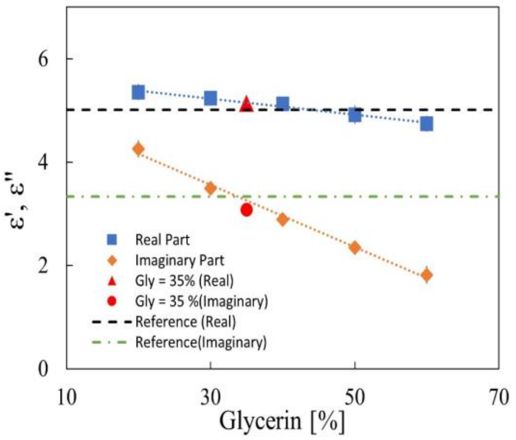

Figure 4. Relationship between complex relative permittivity and glycerin concentration at 0.28 THz. Dashed line indicates approximate straight line.

5. Summary

The dielectric properties of the skin tissue phantoms with the various glycerin concentrations were measured by using the THz-TDS. The complex relative permittivities depended on the glycerin concentration and decreased with the increment of the glycerin concentration. The permittivities of the phantom with 35% glycerin were close to that of the skin tissue at 0.28 THz.

For a step closer to the skin tissue, it is necessary to modify the complex relative permittivities by adding other materials such as sodium chloride and polyethylene, which were used as materials for the gigahertz phantoms [4].

6. Acknowledgments

This work has been supported by the Ministry of Internal Affairs and Communications of Japan Grant Number JPMI10001.

References

[1] World Radiocommunication Conference 2019 (WRC-19) Final Acts, Available from: http://handle.itu.int/11.1002/pub/813b5921-en

[2] IEEE Std 802.15.3d-2017, “IEEE Standard for High Data Rate Wireless Multi-Media Networks Amendment 2: 100 Gb/s Wireless Switched Point-to-Point Physical Layer,” Available from: https://ieeexplore.ieee.org/document/8066476

[3] Kawabata K, Sasaki K, Li K, Suga R, Watanabe S, Hashimoto O, “Design of Human-Skin Equivalent Phantom for Evaluating the Surface Temperature Elevation due to Millimeter Wave Exposure," Proceedings of URSI Asia-Pacific Radio Science Conference (AP-RASC) Mar. 2019

[4] Yoshinobu O, Ito K, Kawai H. “Solid Phantom Composed of Glycerin and its Application to SAR Estimation.” IEICE Transactions on Communications. 2000; B(J83): 534–543.

[5] Y. He, K. Liu, and. C. Au, “Determination of terahertz permittivity of dehydrated biological samples,” Italic IPEM. Phys. Med. Biol. 62, pp.8882-8893, Nov. 2017

Calculation of Electromagnetic Field Distribution for Predicting Indoor 28 GHz Millimeter-wave Propagation Characteristics in Residential House Environment

Sango NAGAMOTO[1] and Manabu OMIYA[2*]
[1]Graduate School of Information, Science and Technology, Hokkaido University, 060-0814 Sapporo, Japan
[2]Information Initiative Center, Hokkaido University, 060-0811 Sapporo, Japan
*omiya@iic.hokudai.ac.jp

Abstract – To predict indoor 28 GHz millimeter-wave propagation characteristics in residential house environment, this paper carries out large-scale numerical electromagnetic field simulations based on the FDTD technique with a high-performance computer system and visualizes indoor and outdoor electromagnetic field distributions. They are useful to evaluate path loss model parameters such as path loss exponent, shadow fading and cross-polarization discrimination, and to design wireless networks for the 5G mobile communication system.

Keywords – 5G mobile communication; millimeter wave; indoor radio wave propagation; FDTD

1. Introduction

The fifth generation (5G) mobile communication system is attracted much attention because of its excellent properties such as high data rate and system capacity. They are realized using the 28 GHz millimeter wave (mm-wave) frequency band with the relatively broad bandwidth [1]. An emergent subject solved for 5G mobile communication system is modeling indoor propagation at the frequency which the several articles reported [2]-[4]. They measured and calculated propagation characteristics in the indoor scenarios such as a conference rooms and office environment. However, another scenario such as a residential house [5] should be discussed for coverage and data throughput.

The paper studies indoor 28 GHz mm-wave propagation characteristics in typical Japanese two-story wooden residential house environment using large-scale electromagnetic field simulations based on the parallel finite difference time domain (FDTD) technique running on the high-performance computer system [6,7]. Indoor and outdoor electromagnetic field distributions are visualized and discussed for vertical and horizontal components. They are useful to predict indoor and indoor-to-outdoor mm-wave propagation characteristics and plan a wireless network with wider coverages.

2. Computer Simulations of MM-wave Propagation in a Residential House

Fig. 1 depicts a geometry and dimensions of a two-story wooden residential house which is a typical Japanese house. Its dimension is 9.4 m × 8.3 m × 7.3 m. Also, Fig. 2 shows the plan of ground floor and the arrangement of furniture. There are many rooms and spaces separated by interior partitions and wooden doors. The material classes and their electric constants at 28 GHz are determined appropriately referring to [8]. In Fig. 2, TX indicates location of a transmitter (TX) including a vertical half-wavelength dipole antenna whose height is 1.7 m above the floor. The TX antenna is excited by a sinusoidal signal at the frequency of 28 GHz.

The numerical electromagnetic field simulator ***Jet FDTD*** being developed by the authors is employed to predict indoor propagation characteristics. Assuming the spatial resolution of 1 mm, the FDTD problem space consists of 800 billion cells. Then, calculations performed by the high-performance computer system in Hokkaido University require the memory capacity of 60 TB and the processing time of 150 hours until transient behaviors of electromagnetic field component vanish in the problem space.

3. Calculation Results and Discussions

Fig. 3 visualizes magnitude distributions of the vertical component E_z (co-pol.) and the horizontal component E_{xp} (cross-pol.). The observation plane corresponds to an xy-plane whose height is 1 m above the floor in the house and 1.86 m above the outdoor ground. These figures reveal following results. The vertical components appear in both of line-of-sight (LOS) and non-line-of-sight (NLOS) environment. On the other hand, the horizontal components are mainly observed in LOS environment near TX and attenuated easily away from TX. Also, they are not observed in NLOS environment.

4. Conclusion

To predict indoor 28 GHz mm-wave propagation characteristics in residential house environment, the paper carried out the large-scale numerical electromagnetic field simulations based on the FDTD technique with the high-performance computer system and visualized the indoor and outdoor distributions of vertical and horizontal electric field components. They are useful to determine path loss model parameters such as path loss exponent, shadow fading and cross-polarization discrimination, and to design wireless networks for the 5G mobile communication system.

Acknowledgment

This work was supported by JSPS KAKENHI Grant Number 19K04385. The large-scale numerical analysis was conducted using the high-performance computer system in Information Initiative Canter, Hokkaido University.

References

[1] Jiang W, Han B, Habibi MA, and Schotten HD. The Road Towards 6G: A Comprehensive Survey. IEEE Open Journal of the Communications Society 2021; (2): 334-366.

[2] MacCartney Jr. GR, Rappaport TS, Sun S, and Deng S. Indoor Office Wideband Millimeter-wave Propagation Measurements and Channel

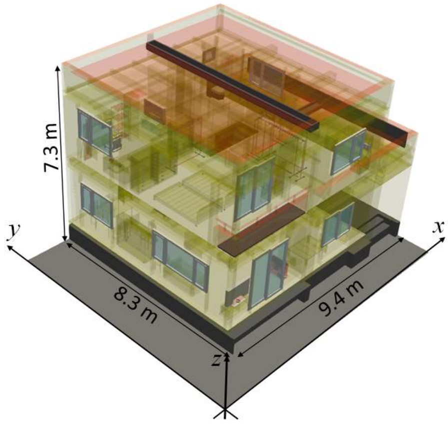

Figure 1. Geometry and dimension of a residential house.

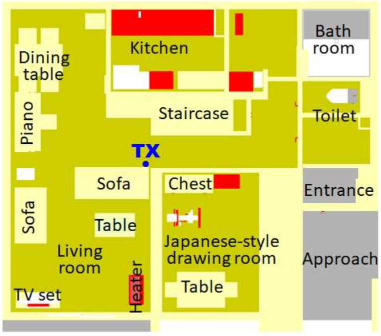

Figure 2. Floor plan.

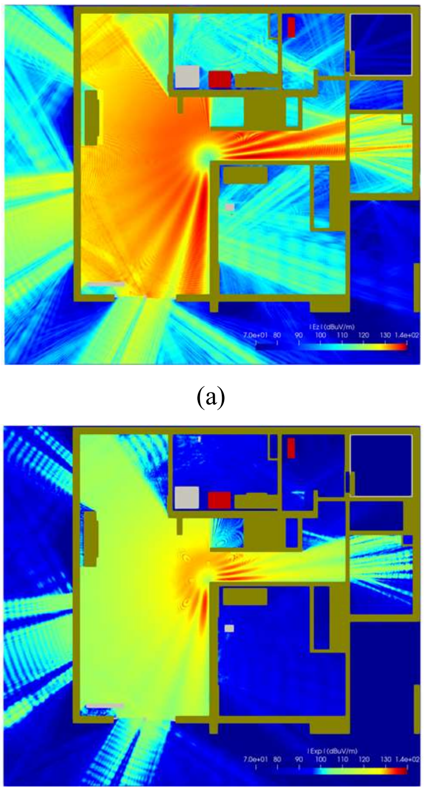

(a)

(b)

Figure 3. Magnitude distributions of the vertical electric field component E_z (a) and the horizontal one E_{xp} (b).

Models at 28 and 73 GHz for Ultra-dense 5G Wireless Networks. IEEE Access 2015; (3): 2388-2424.

[3] Huang F, Tian L, Zheng Y, and Zhang J. Propagation Characteristics of Indoor Radio Channel from 3.5 GHz to 28 GHz. 2016 IEEE 84th Vehicular Technology Conference (VTC-Fall) Sept. 18-21, 2016, Montreal, QC, Canada.

[4] Zhou Y, Sun X, Zhang P, Wang H, Hu Z, Wang H. Multi-frequency Millimeter-wave Large-scale Path Loss Characterization for Indoor Environment. 2019 International Symposium on Antennas and Propagation (ISAP) Oct. 27-30, 2019, Xi'an, China.

[5] Zhang CGY and Jiang X. Simulation and Analysis of 28 GHz Millimeter-wave Propagation Characteristics in Typical Residential House Environment. 2018 11th UK-Europe-China Workshop on Millimeter Wave and Teraherts Technologies (UCMMT) Sept. 5-7, 2018, Hang Zhou, China.

[6] Yu W, Mittra R, Su T, Liu Y, and Yang X, Parallel Finite-Difference Time-Domain Method; Norwood, Artech House, 2006.

[7] Suzuki Y and Omiya M. Computer Simulations for a Site-specific Modeling of Indoor Radio Wave Propagation. 2016 IEEE Region 10 Conference (TENCON) Nov. 22-25, 2016, Singapore, pp. 123–126.

[8] Recommendation ITU-R P.2040-1. Effects of Building Materials and Structures on Radiowave Propagation above About 100 MHz. Jul. 2015.

[Invited Talk] Title: Development of Optically Pumped Atomic Magnetometers towards Next Generation Brain Imaging

Tetsuo KOBAYASHI[1*]

1 Graduate School of Engineering, Kyoto University, 615-8510 Kyoto, Japan

*Corresponding author: kobayashi.tetsuo.2c@kyoto-u.ac.jp

Abstract – Optically pumped atomic magnetometers (OPMs) using alkali metal vapors contained in glass cells are capable of measuring extremely small magnetic fields. In recent years, it was found that OPMs operating under spin-exchange relaxation-free (SERF) condition as well as high-density SERF-like condition have reached sensitivities comparable to and even surpassing those of superconducting quantum interference devices (SQUIDs). At present, the most sensitive OPM has achieved the sensitivity of sub-femto tesla (10^{-16} T) range. We have been developing the SERF and high-density SERF-like OPMs with pump-probe arrangement since 2006. In 2011, we proposed the first high-density K-Rb spin-exchange hybrid OPM. In the hybrid OPM, a circularly polarized pump beam and a linearly polarized probe beam crossed orthogonally in a cell including two vaporized K and Rb atoms together. The homogeneity of the sensing characteristics of the hybrid OPMs is able to be increased inside the cell [1, 2] and its sensitivity is also be improved by setting the optimal densities of the K and Rb atoms as well as their optimal density ratio [3].

Meanwhile, since sensitivity of OPMs does not depend on frequency, OPMs are suitable to be used as receiving sensors for ultra-low field MRI systems. In 2017, for the first time, we reported that MRI and NMR signals could be acquired with an OPM operating at a Larmor frequency of 5 kHz without the use of any cryogenics [4]. These results demonstrate the feasibility of ultra-sensitive OPMs for detecting tiny magnetic fields towards innovative neuromagnetic imaging systems. We believe that the applicability of new neuroimaging systems based on the OPMs might provide important advancements in neuroscience and improve the clinical diagnosis of neurological and psychiatric disorders as well.

Keywords – OPM; MRI; MEG;

References

[1] Y. Mamishin, Y. Ito and T. Kobayashi, *IEEE Trans. on Magnetics*, 53(5), 1-6 (2017)
[2] K. Nishi, Y. Ito and T. Kobayashi, *Optics Express*, 26(2), 1988-1996 (2018)
[3] S. Ito, Y. Ito and T. Kobayashi, *Optics Express*, 27(7), 8037-8047 (2019)
[4] I. Hilschenz, T. Kobayashi, et al., *Journal of Magnetic Resonance*, 274, 89-94 (2017)

Magnetic Domain Transition Applied to Electromagnetic Shielding and Measurements

Tomoo Nakai[1]*

[1]Industrial Technology Institute, Miyagi prefectural Government, Sendai-city 981-3206, Japan
*Corresponding author: nakai-to693@pref.miyagi.lg.jp

Abstract – A magnetic momentum in a magnetic thin film behaves as if it is restricted in a 2-D sheet, due to the strong demagnetizing force along the thickness direction of the film. The momentum in the film clustered by the exchange force and forms a certain pattern of magnetic domain. A formation and variation of the pattern of magnetic domain is dominated by magnetic energy which is affected by the external field, the anisotropy energy, and the 2-D shape of the film. In this study, we utilize the magnetic domain transition appeared from the quasi-2D property of magnetic thin film for the target of electromagnetic devices and of electromagnetic measurements using its specific magnetic phenomenon.

Keywords – magnetic domain; domain transition; thin film; uniaxial easy axis; distributed normal field

1. Introduction

The previous research of us shows that a narrow rectangular shaped thin film element with inclined in-plane easy axis in 70 degrees has a typical characteristic of magnetic domain transition (1). The transition phenomenon also can be controlled by a normal magnetic field (2)(3). Figure 1 shows schematics which explains the phenomenon of domain transition of our study and the effect of normal field for it. We also confirmed that this controlling method is possible to apply to parallel line adjacent many-body configuration of elements having the typical transition property in each element (4). In this case, there is a mutual magnetic interaction existing within the many-body elements. This trial and the obtained results were important for realizing a high-density device using this phenomenon. In this report, a proposal of application is carried out using the domain transition phenomenon, such as an electromagnetic shielding based on a complex permeability and also an electromagnetic measurement

based on a photo optical interference and polarization of the element.

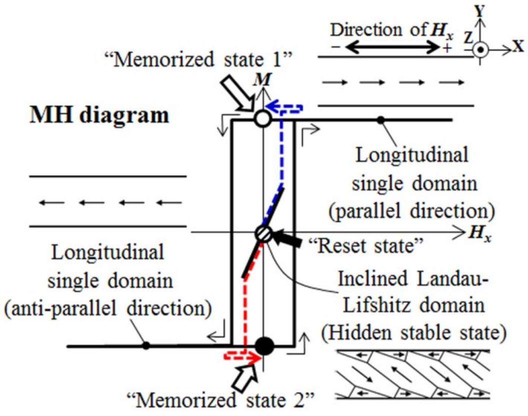

(a) Without normal magnetic field.

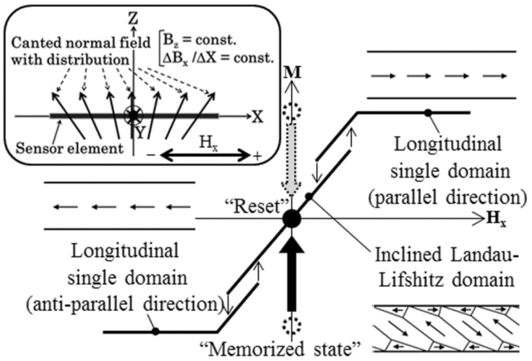

(b) With distributed normal magnetic field.

Figure 1. Magnetization diagram of single element with hidden multi-domain state.

2. Fundamental and experiment

Figure 2 shows a schematic explanation of the layout of the many-body elements and the direction of easy axis. It also shows

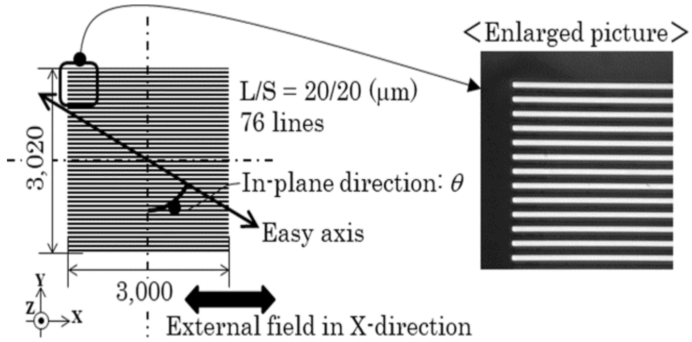

Figure 2. Structure of many body elements.

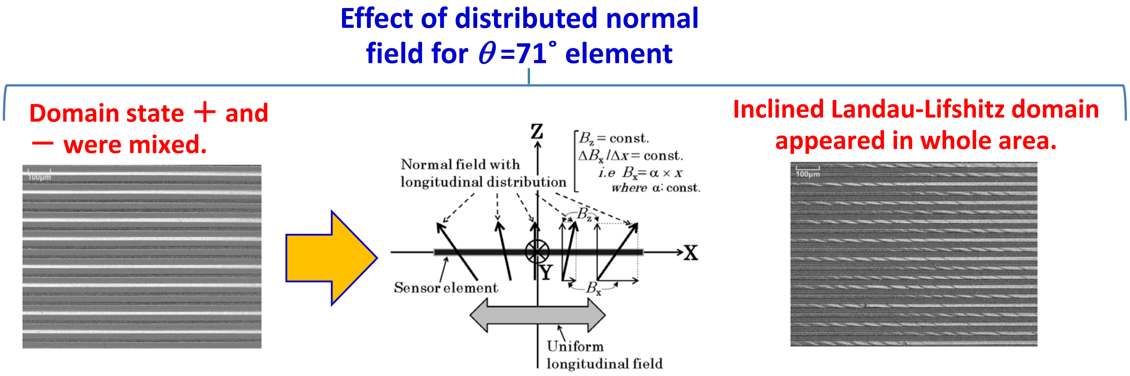

Figure 3. Effect of distributed field for the many-body elements.
(Left: Without normal field, Right: With applying a distributed normal field)

an enlarged view of a part of a fabricated element. The element, which is made by an amorphous $Co_{85}Nb_{12}Zr_3$ film, was fabricated by a thin-film process. The single element of it had dimensions as 20 μm width, 3,000 μm length and 2.1 μm thickness. The multiple elements were made by this element adjacently arranged in 76 lines with the L/S as 20 μm and 20 μm. The in-plane uniaxial magnetic anisotropy was induced by magnetic field annealing. The direction of easy axis θ was controlled by the magnetic field direction while annealing.

Figure 3 shows a result of experiment. The multi-domain state having an inclined Landau–Lifshitz domain appeared in the whole area of many-body elements by applying the distributed normal field in spite of existing a mutual interaction. This result shows a possibility of this phenomenon to apply not only to a sensor but also to electromagnetic devices with high-density configuration.

Figure 4 and Figure 5 introduces a measured results of high frequency permeability obtained for the multiple-element. The three different cases of easy axis direction were fabricated, and the measured magnetic domain structure using a Kerr microscope was shown in Figure 4. Both the Edge part and the middle part of the multiple elements were shown here. The white and the gray line indicate an element that has a parallel or anti-parallel magnetic moment in the element. The striped pattern indicates the area of the Landau-Lifshitz domain having a contiguous different direction of magnetic moment. In case of the θ=61 °, it was consisted of both the parallel domain and the Landau-Lifshitz domain. In case of the θ=90 °, it was consisted of both the parallel domain and the anti-parallel domain. In case of the

θ=71°, it was consisted of both the parallel domain and the anti-parallel domain in the middle area of the element, and a mixture of the three different domains near the edge area. The element of θ=71° is the controllable one using the distributed normal field.

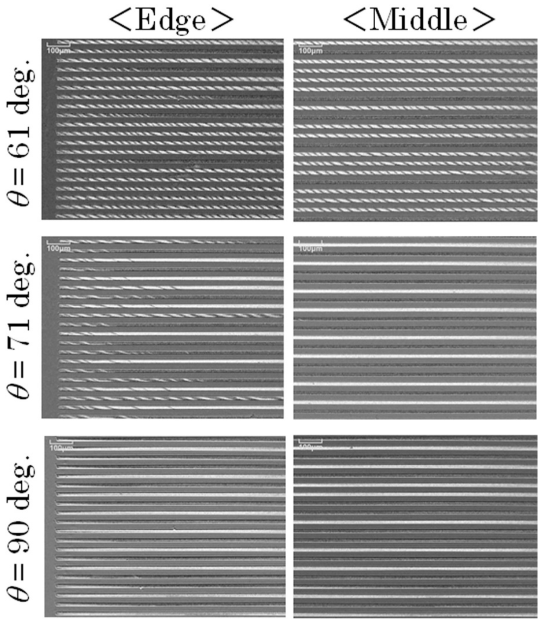

Figure 4. Magnetic domain in three cases of different magnetic easy axis direction θ.

Figure 5 shows a high-frequency permeability of the element corresponding to the element in Figure 4. The element having the Landau-Lifshitz domain has a certain value of permeability, whereas the element with parallel and anti-parallel has a slight permeability. Based on this result, the artificial domain transition of the element is able to realize a functional device which has a function of the switched high frequency permeability.

3. Summary

A proposal of application using the domain transition phenomenon is carried out. A certain possibility of applying a electromagnetic device such as an electromagnetic shielding based on a switched complex permeability and also an electromagnetic measurement based on a switched photo optical interference and polarization of the element were shown.

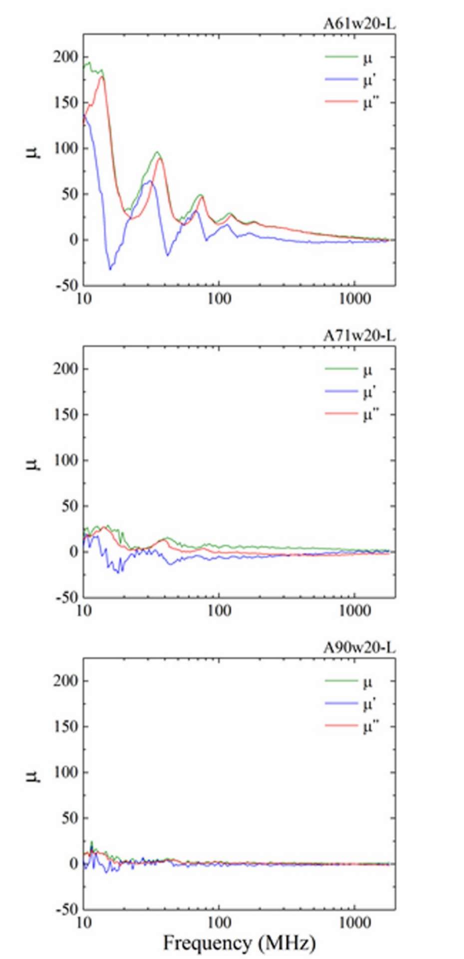

Figure 5. High frequency permeability of the elements in Figure 4. (Upper: θ=61°, Middle: θ=71°and Bottom: θ=90°)

References

[1] T. Nakai, K. Takada and K. Ishiyama, “Existence of Three Stable States of Magnetic Domain for the Stepped Giant Magneto-impedance Element and Proposal for Sensor With Memory Function”: IEEE Trans. Magn. , 45, No. 10 (2009), pp.3499-3502.

[2] T. Nakai: “Magnetic Domain of Stepped Magneto-Impedance Sensor Controlled by a Normal Magnetic Field”, IEEJ Trans. Sensors and Micromachines, Vol. 138, No. 1(2018), 23-29.

[3] T. Nakai: “Magnetic domain transition controlled by distributed normal magnetic field for stepped magneto-impedance sensor”, International Journal of Applied Electromagnetics and Mechanics, 59 (2019) 105–114.

[4] Magnetic Domain Transition of Adjacent Narrow Thin Film Strips with Inclined Uniaxial Magnetic Anisotropy, Tomoo Nakai, Micromachines, 11, 279 (2020).

Uncertainty Evaluation of Optical Electric-Field Probe Calibration for Human Exposure Assessment at 85 kHz

Yuto SHIMIZU[1*], Eishi OHO[1,2], Jerdvisanop CHAKAROTHAI[1], Tomoaki NAGAOKA[1],
Takuji ARIMA[2] and Toru UNO[2]
[1]National Institute of Information and Communications Technology,
4-2-1 Nukui-kitamachi, Koganei, Tokyo 184-8795, Japan
[2]Tokyo University of Agriculture and Technology,
2-24-16 Naka-cho, Koganei, Tokyo 184-8588, Japan
*Corresponding author: y_shimizu@nict.go.jp

Abstract –The electromagnetic field in the intermediate frequency band (300 Hz–10 MHz) emitted from wireless power transfer (WPT) systems for electric vehicles is relatively strong, and thus human exposure assessment for these systems is required. We have developed an optical electric-field probe calibration method to measure the electric field at 85 kHz in a tissue-equivalent liquid. In this study, we evaluated the uncertainty of the calibration method to ensure the reliability of the calibration. The expanded uncertainty of the calibration method is about 10%. In addition, we analyzed the dominant uncertainty source. From this analysis, the dominant source is the probe position of the z-axis, the uncertainty of which is about 4%. We found that the sources with high uncertainty, including the probe position of the z-axis, are related to the electric field degradation.

Keywords – exposure assessment; optical electric-field probe; calibration, uncertainty

1. Introduction

In recent years, high-power wireless power transfer (WPT) systems operating in the intermediate frequency band, which ranges from 300 Hz to 10 MHz, for electric vehicles have been rapidly developed. These systems emit a relatively strong electromagnetic field, and thus human exposure assessment for these systems is required. Below 10 MHz, an induced electric field is used for safety criteria [1]. In Japan, 85 kHz is the candidate frequency of WPT systems for electric vehicles. For this reason, we developed a calibration method for the optical electric-field probe in a tissue-equivalent liquid in the intermediate frequency band, particularly 85 kHz, to measure the electric field inside the liquid [2]. In this study, to ensure the reliability of the calibration, we evaluated the uncertainty of the calibration system at 85 kHz. In addition, we analyzed the result of the uncertainty evaluation and determined the dominant source of the uncertainty.

2. Caribration Method for Optical Electric-Field Probe

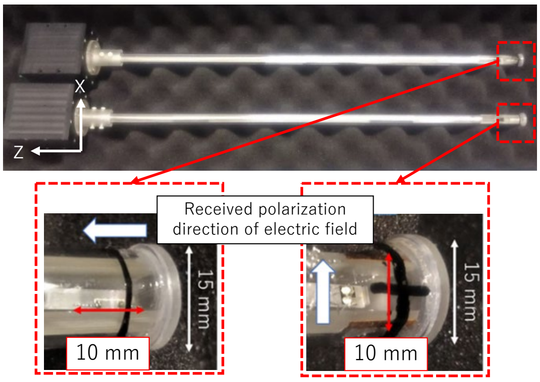

Figure 1. Structure of optical electric-field probe.

Figure 1 shows the optical electric-field probe calibrated in this study. The dipole antenna with a length (l_{opt}) of 10 mm is connected to the electric-to-optical (E/O) converter and covered with a plastic cylinder, whose diameter and length are 15 mm and 500 mm, respectively. When we measure the electric field with the optical electric-field probe, firstly, the dipole antenna receives the electric field and excites the received voltage. The received voltage is converted into an optical signal by the E/O converter. The optical signal is then transmitted to the optical-to-electric (O/E) converter via an optical fiber and converted to electric signals

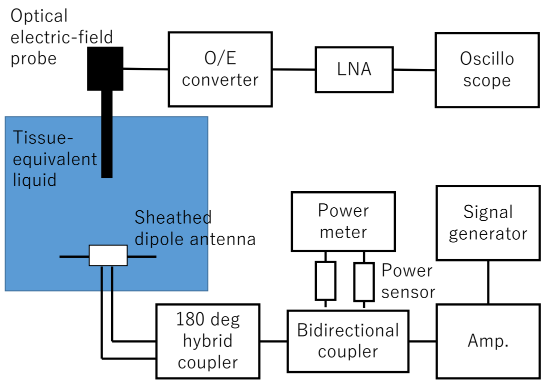

Figure 2. Probe calibration system

by the O/E converter. The oscilloscope measures the output voltage from the electric signal. Finally, we obtain the electric field intensity from the product of the received signal and conversion factor.

To measure the electric field by this procedure, the conversion factor between the received voltage and the electric field is required. In this study, to measure all three components (x-, y- and z- axes) of the electric fields, we should calibrate two types of optical electric-field probe as shown in Figure 1. The probe shown on the left side of Figure 1 can receive the horizontal electric field, and the other one can receive the vertical electric field. To calibrate the probe, we employed the reference antenna method [3], in which the conversion factor is determined by comparing the distance characteristics of the electric field and output voltage. Figure 2 shows the calibration system using the reference antenna. In this study, a sheathed dipole antenna [3] was employed as a reference antenna. The calibration method consists of three parts as follows:

1) Measure the distance characteristics of the *S* parameter between the transmitting and receiving antennas, which have the same characteristics, in the tissue-equivalent liquid. From these characteristics, the transmitting antenna factor F^e is estimated. The detailed estimation scheme is described in [4].

2) Set the reference antenna at the bottom of the water tank and the probe above the reference antenna. Pull up the probe and measure the distance characteristic of the output voltage excited by the electric field from the reference antenna.

3) Calculate the average electric fields $|E_x|$ and $|E_z|$ in the probe using the following equations (1) and (2):

$$|E_x(x,y,z)| = \frac{\sqrt{P_{in}}|F^e|}{\sqrt{2}|l^e|l_{opt}} \int_{-l_{opt}/2}^{l_{opt}/2} |e'_x(x,y,z)|dx, \tag{1}$$

$$|E_z(x,y,z)| = \frac{\sqrt{P_{in}}|F^e|}{\sqrt{2}|l^e|l_{opt}} \int_{-l_{opt}/2}^{l_{opt}/2} |e'_z(x,y,z)|dz, \tag{2}$$

where P_{in} and l^e denote the antenna input power and the effective length of the reference antenna, respectively. e'_x and e'_z are electric fields of the x-axis and z-axis components, respectively, from the reference antenna. Finally, the conversion factor is obtained by dividing the estimated electric field intensity by the measured output voltage.

3. Uncertainty Evaluation of Probe Calibration

From the calibration method mentioned in Section 2, the uncertainty source of the probe consists of the uncertainties of the output voltage and the electric field intensity. In this study, we focused on the uncertainty of the electric field intensity. Tables 1 and 2 show the uncertainty budgets of the electric fields of the x-axis and z-axis components, respectively. The uncertainty budget was based on [4]. The probe position, antenna length, conductivity and relative permittivity are related to the terms e'_x and e'_z in equations (1) and (2). We evaluated the uncertainties caused by those uncertainty sources by Monte Carlo simulations, since e'_x and e'_z are calculated using numerical integration, the sensitivity coefficients of which are too difficult to derive. The number of trials for the Monte Carlo simulation was

Table 1. Uncertainty budget of horizontal component calibration.

Uncertainty source	Tolerance [%]	Probability distribution	Divisor	Sensitivity coefficient	Standard uncertainty [%]
Probe position x	5	Rectangular	-	-	0.03
Probe position y	5	Rectangular	-	-	0.05
Probe position z	5	Rectangular	-	-	4.07
Antenna length	2	Rectangular	-	-	0.19
Liquid conductivity	2	Normal	-	-	1.00
Liquid permittivity	2	Normal	-	-	0.00
$\lvert S_{21}\rvert$	1.2	Normal	2	0.50	0.30
$\lvert S_{11}\rvert$	5.6	Normal	2	0.08	0.22
$\lvert S_{22}\rvert$	4.9	Normal	2	0.10	0.25
Antenna input power	2.3	Normal	2	0.50	0.58
Combined standard uncertainty					4.3
Expanded uncertainty (*k*=2)					8.6

Table 2. Uncertainty budget of vertical component calibration.

Uncertainty source	Tolerance [%]	Probability distribution	Divisor	Sensitivity coefficient	Standard uncertainty [%]
Probe position x	5	Rectangular	-	-	1.18
Probe position y	5	Rectangular	-	-	0.10
Probe position z	5	Rectangular	-	-	4.87
Antenna length	2	Rectangular	-	-	0.04
Liquid conductivity	2	Normal	-	-	1.01
Liquid permittivity	2	Normal	-	-	0.00
$\lvert S_{21}\rvert$	1.2	Normal	2	0.50	0.30
$\lvert S_{11}\rvert$	5.6	Normal	2	0.08	0.22
$\lvert S_{22}\rvert$	4.9	Normal	2	0.10	0.25
Antenna input power	2.3	Normal	2	0.50	0.58
Combined standard uncertainty					5.2
Expanded uncertainty (*k*=2)					10.4

set to 5000. To obtain the tolerance of the uncertainty source, we used the data sheet of each measurement instrument provided by the manufacturer.

As shown in Tables 1 and 2, the expanded uncertainties (*k*=2) are 8.6% and 10.4%, respectively. We found that the most dominant uncertainty source is the probe position in the z-axis. The uncertainties are 4.07% and 4.87% in the calibration for the horizontal and vertical components, respectively. These values are higher than those of the other uncertainty sources. The electric field intensity from the reference antenna decreases along the z-axis in this calibration system as shown in Figure 2; thus, the deviation from the measurement points of the z-axis has a large effect on the electric field calculation. Moreover, E_z decreases along the x-axis; therefore, the uncertainty of the probe position of the x-axis is dominant in the probe calibration of the vertical component. The second dominant source is the electric conductivity, which is also related to the electric field degradation. From these results, we found that it is important to reduce the value of the uncertainty source related to electric field degradation in the employed calibration method.

4. Conclusion

In this study, we evaluated the uncertainty of an optical electric-field probe calibration system in a tissue-equivalent liquid. In particular, we focused on the uncertainty of the electric field. From the evaluation result, the expanded uncertainties are 8.6% and 10.4% in the calibration for the horizontal and vertical components, respectively. In addition, the most dominant uncertainty source is the probe position of the z-axis, the values of which are 4.1% and 4.9%, respectively. This source is related to the electric field degradation. The other source with high uncertainty is also related to it. Thus, it is important to reduce the source of the electric field degradation to reduce the uncertainty.

Acknowledgement

This study was supported by the Ministry of Internal Affairs and Communications, Japan (JPMI10001).

References

[1] ICNIRP, “Guidelines for limiting exposure to electromagnetic fields (100 kHz to 300 GHz),” *Health Phys.*, vol. 118, no. 5, pp. 483–524, May, 2020.

[2] E. Oho, Y. Shimizu, J. Chakarothai, K. Wake, T. Arima, and T Uno, “A study on a calibration method for an optical electric-field probe in a liquid phantom using a sheathed dipole antenna at 85 kHz-band,” *IEICE Tech. Rep.*, PEM 2020-06, pp. 7–12, Oct., 2020.

[3] H. Sato, N. Fujii, Q. Chen, N. Ishii, M. Takahashi, R. Suga, K. Uesaka, and H. Yoshida, “Dipole antenna with sheathed-cover for seawater use,” *Proc. 2017 International Symposium on Antennas and Propagation* (ISAP 2017), p. 1376, Puket, Thailand, Oct. 2017.

[4] N. Ishii, J. Chakarothai, K. Wake, and S. Watanabe, “Probe calibration in lossy liquid using small dipole antennas for megahertz-band specific absorption rate measurements,” *IEEE Trans. Instrum. Meas.*, vol. 69, no. 6, pp. 3078–3088, Jul. 2020.

[Invited Talk] Reactive Near-Field Sensors: Requirements, Technology, and Applications

Sven KÜHN[1] and Niels KUSTER[1,2*]

[1] Foundation for Research on Information Technologies in Society, 8004 Zurich, Switzerland
[2] Department of Information Technology and Electrical Engineering, ETH Zurich, 8092 Zurich, Switzerland

*Corresponding author: kuster@itis.swiss

Abstract – Measuring the reactive near-field of electromagnetic sources remains a significant challenge, as both the complex magnetic and electric components must be assessed without interacting with the source. Characterization of reactive-near fields is essential for electromagnetic compatibility, antenna design validation, and human exposure evaluations. This paper summarizes the requirements and technologies for reactive near-field measurements and provides examples of applications where these measurements are used.

Keywords – radiofrequency; electromagnetic compatibility, human exposure, specific absorption rate; measurement (5 maximum)

1. Introduction

Measurements in the reactive near-field are a critical element in radiofrequency (RF) electromagnetic compatibility (EMC) and antenna design assessment. Near-field measurements are used to evaluate the safety of electromagnetic (EM) sources against human exposure safety limits, e.g., [1,2,3]. Near-field measurements are also required to locate and assess RF interferences and emissions in electronic circuits and devices [4].

This paper derives the requirements for near-field probes based on their applications before discussing the suitability of different near-field probe technologies.

2. Applications and Requirements

The main applications for RF EM reactive near-field measurements include (i) safety testing of intentional transmitters with human exposure limits [1,2,3] and (ii) EMC testing for RF co-existence of intentional and unintentional transmitters, e.g., according to [4,5].

There are some global requirements for reactive near-field probes: (ii) fine spatial resolution to resolve EM fields and derived quantities, e.g., the specific absorption rate (SAR) and absorbed power density (APD), with sub-millimeter resolution; (ii) sub-millimeter positioning to resolve strong field gradients in the reactive near-field, and (iii) probe "EM-transparency" to avoid introducing artificial EM boundary conditions that alter the reactive near-field of the device under test (DUT).

Safety testing of exposures is highly regulated, and therefore most requirements for reactive near-field probes are defined by the underlying safety [1,2,3] and test standards [6,7,8]. The dynamic range of the probe is typically defined as a multiple of the underlying safety limit and ranges from a fraction (e.g., 1%) to a multiple of the limit (e.g., 10x). Safety standards distinguish between limits to prevent thermal hazards to the human body (e.g., >100 kHz for SAR, and >6 GHz for APD [3]) and nerve stimulations hazards (e.g., internal electric (E-) fields below 10 MHz [2]). This distinction manifests itself in the probe requirement. Below 10 MHz (unless sources transmit at single frequencies), the signal must be resolved in the time domain to test compliance with nerve stimulation safety limits. Above 100 kHz, for tests involving SAR and APD limits, it is sufficient if the probe can accurately assess the magnitude of the EMF. While this paper only discusses fields inside the human body, it is possible to test safety with EMF limits outside the human body, i.e., with derived limits or reference limits. However, these external limits may be too conservative. Furthermore, above a few MHz, the human body places significant loads on the DUT transmitter structure. Field evaluations without a phantom simulating the human body may not be representative of actual human exposure.

The requirements for reactive near-field probes used in EMC and RF co-existence tests are often driven by industry standards, e.g., the immunity level of one device weighing off the emission levels of another. Devices can be complete consumer products, such as hearing aids and mobile phones as tested in [5], or active circuits within a product, such as a global positioning system (GPS) receiver and the RF transmitters or digital clocks inside a mobile phone. Because of the much lower signal levels (e.g., as low as -125 to -150 dBm for GPS), a vital requirement of the probe for reactive EMC near-field testing is sensitivity. EM interference (EMI) susceptibility is typically frequency-dependent (e.g., 1575.42 and 1227.60 MHz for GPS), so EMC near-field probes are required to resolve signals in the frequency domain.

3. Near-field Probe Technologies

Broadband near-field probes for testing with thermal-based safety limits follow the designs shown in Figures 1 and 2. These probes follow the operating principle of an RF power meter: the EM field is detected by an electrically small EM field sensor and rectified by a detector diode. High-impedance transmission lines provide the isolation and "EM-transparency" of this probe design. The design allows for good sensitivity, high spatial resolution, and low measurement uncertainty at the expense of lacking information about the RF signal.

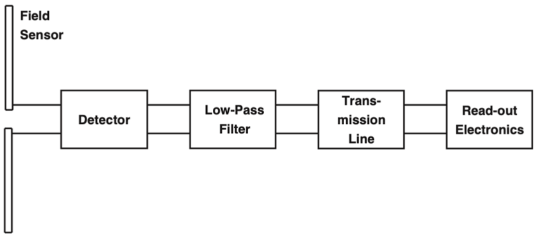

Figure 1. Simplified schematic of a broadband field probe.

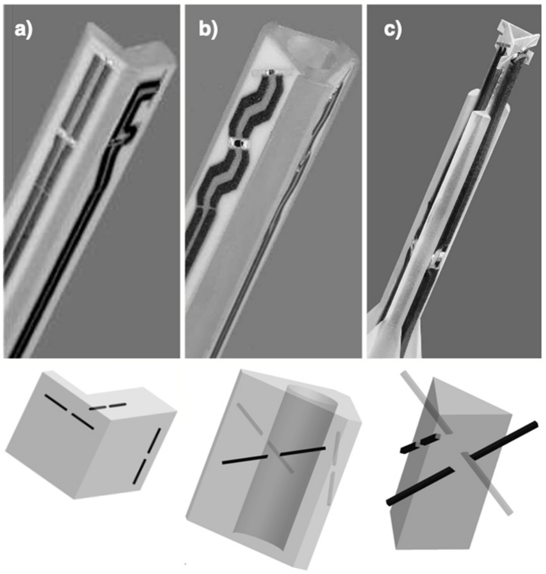

Figure 2. E-field probe configurations: a) E-field probe for measurements in air with one sensor aligned to the probe axis and two orthogonal sensors; b) dosimetric probe for E-field measurements in tissue-simulating liquid, allowing the integration of an optical proximity sensor in its center; c) miniature dosimetric probe with interleaved dipoles [9].

Electro-optical (EO) near-field probes overcome the limitation of broadband probes by modulating the RF signal onto an optical carrier signal and employing RF signal recovery in data acquisition. A distinction is made between active [10] and passive [11] designs. The main difference between the designs is sensitivity, typically 40 dB to 60 dB higher for active designs at the same spatial resolution. The sensitivity of active designs allows them to be used in EMC reactive near-field scanning of unintentional transmitters [12]. Passive EO probes are limited to near-field scanning of intentional transmitters due to their limited sensitivity.

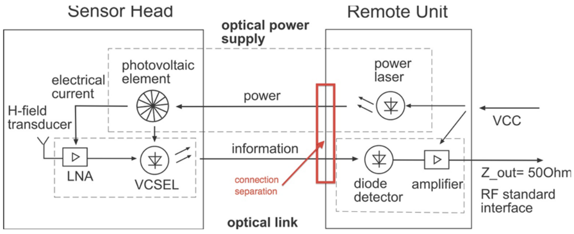

Figure 3. Schematic design of an active EO probe.

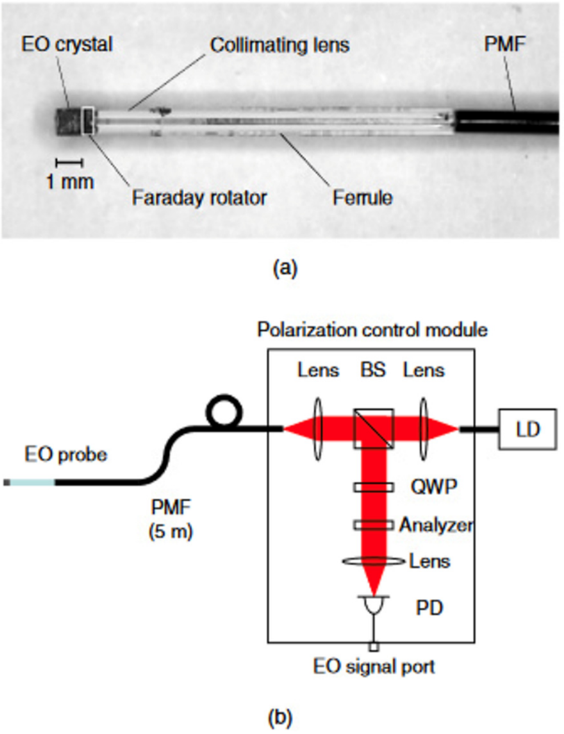

Figure 4. (a) Passive EO probe and (b) schematic design, source: [11].

Although EO probes operate <10 MHz [13], their high costs, large measurement uncertainties, and some designs offering insufficient sensitivity have been prohibitive for safety testing with nerve stimulation limits. In this frequency range, methods have been developed to measure the external electrical fields and test compliance with reference levels and/or extrapolation to internal fields [7].

4. Conclusions

Diode-loaded sensors are the first choice when accurate RMS values are the primary goal, e.g., in safety evaluations with thermally based limits. The phase in the reactive near-field can be reconstructed from phaseless measurements using plane-to-plane or source reconstruction methods [15]. EO near-field probes are the best choice when the full time-domain signal is needed for field analysis, e.g., EMC/EMI. High sensitivity in the reactive near-field requires active miniature broadband sensors, which pose a significant challenge to achieve stable probes at acceptable costs.

References

[1] International Commission on Non-Ionizing Radiation Protection. "ICNIRP statement on the "Guidelines for limiting exposure to time-varying electric, magnetic, and electromagnetic fields (up to 300 GHz)"." *Health physics* 97.3 (2009): 257-258.

[2] International Commission on Non-Ionizing Radiation Protection. "ICNIRP statement—protection of workers against ultraviolet radiation." *Health physics* 99.1 (2010): 66-87.

[3] International Commission on Non-Ionizing Radiation Protection. "Guidelines for limiting exposure to electromagnetic fields (100 kHz to 300 GHz)." *Health physics* 118.5 (2020): 483-524.

[4] IEC TS 61967-3:2014 Integrated circuits - Measurement of electromagnetic emissions - Part 3: Measurement of radiated emissions - Surface scan method

[5] IEEE/ANSI C63.19-2019 American National Standard -- Methods Of Measurement Of Compatibility Between Wireless Communications Devices And Hearing Aids

[6] IEC/IEEE 62209-1528:2020 Measurement procedure for the assessment of specific absorption rate of human exposure to radio frequency fields from hand-held and body-worn wireless communication devices - Human models, instrumentation and procedures (Frequency range of 4 MHz to 10 GHz)

[7] IEC PAS 63184:2021 Assessment methods of the human exposure to electric and magnetic fields from wireless power transfer systems - Models, instrumentation, measurement and numerical methods and procedures (frequency range of 1 kHz to 30 MHz)

[8] IEC/IEEE 63195-2 ED1: Determining the power density of the electromagnetic field associated with human exposure to wireless devices operating in close proximity to the head and body using computational techniques, 6 GHz to 300 GHz

[9] Kühn, Sven. EMF risk assessment: Exposure assessment and compliance testing in complex environments. Diss. ETH Zurich, 2009.

[10] A. Kramer, P. Muller, U. Lott, N. Kuster, and F. Bomholt, "Electro-optic fiber sensor for amplitude and phase detection of radiofrequency electromagnetic fields," *Optics letters,* vol. 31, no. 16, p. 2402–2404, 2006

[11] Togo, Hiroyoshi, Naofumi Shimizu, and Tadao Nagatsuma. "Fiber-mounted electro-optic probe with highly stable sensitivity." LEOS 2006-19th Annual Meeting of the IEEE Lasers and Electro-Optics Society. IEEE, 2006.

[12] Kuehn, Sven, et al. "A novel automated phasor measurement system for validated and traceable EMC/EMI near-field analysis." *IEEE Electromagnetic Compatibility Magazine* 5.2 (2016): 41-47.

[13] Kapteos EOprobe data sheet. Accessed online (2021/09/27): https://aea767a7-99c2-4382-9003-3151c2724389.filesusr.com/ugd/e79c35_9f4e1fbb342b4e0c9405ed059bdd0895.pdf

[14] MAGPy Systems for Evaluations of WPT and other Sources. Accessed online (2021/09/27): https://speag.swiss/products/magpy/overview-2/

[15] K. Cujia, A. Fallahi, N. Kuster, "Fast Antenna Characterization Using a Phaseless Based Source-Reconstruction Algorithm, BIOEM 2021 proceedings, Gent, 2021

Fiber-Optic System for S-parameter Measurement of Electrically Small Antennas

Sven KÜHN*[1], Beyhan KOCHALI[2], and Niels KUSTER[1]
[1]IT'IS Foundation, 8004 Zurich, Switzerland
[2]Schmid&Partner Engineering AG, 8004 Zurich, Switzerland

*Corresponding author: kuehn@itis.swiss

Abstract – A measurement system for S-parameter measurements of electrically small antennas employing miniature photonically powered radio frequency over fiber links to ensure minimum electrical footprint of the measurement device. The challenge to achieve accurate measurements of electrically small antennas for communications bands up to 6 GHz is demonstrated along with the ease of obtaining erroneous results for the impedance and resonant frequency when using traditional methods. This paper applies this low perturbation method of complex impedance measurement to a test handset antenna.

Keywords – antenna; s-parameter; radiofrequency; photonic (5 maximum)

1. Introduction

Most antenna designs today are electrically small and integrated into electrically small devices. Measuring them in their native environments is impossible as connecting radio-frequency cables extend the electrical size and affects the antenna performance. Traditional measures to mitigate this effect include the use of chokes or ferrites. These solutions are, however, highly unreliable and often too bulky. A measurement system able to test those electrically small antennas without perturbation is desirable. This paper presents and evaluates a miniaturized fiber-optic s-parameter measurement for electrically small antennas and devices.

2. Methods

The system (Fig. 1) uses direct laser modulation for signal transmission of the RF signal fed to the 50Ω input of the Optical Head and from the Remote Unit to the Optical Head [1]. The Optical Head and the Remote Unit are exclusively optically linked by fiber optics. A power laser is used to illuminate a photovoltaic converter inside the Optical Head via fiber optics. The electrical energy from the photovoltaic cell drives all the active components inside the Optical Head.

The RF output (port 1) of the vector network analyzer (VNA) modulates the output of a VCSEL (vertical cavity surface emitting LASER) inside the Remote Unit. This signal is demodulated with a high-speed photodiode inside the Optical Head to provide the local reference forward signal into the device under test. The reflected signal modulates the optical output of a VCSEL inside the Optical Head. This signal is then transmitted to the remote unit over an optical fiber. At the remote unit, the optical signal is demodulated again using a fast photodiode. The received RF signal is amplified by a transimpedance amplifier and made available using a standard 50Ω output connector to the receiving port (port 2) of the VNA. The system can be seen as a miniature, broad-band, electrically isolated VNA port extension. Therefore, we named the system optical head for VNA (OH4VNA).

Fig. 2 shows the OH4VNA system in operation with the VNA and the PC used to obtain S11 measurement from the 2-port VNA measurement after open-short-load (OSL) calibration.

To test the performance of the OH4VNA system in comparison with traditional measurement methods, we designed, simulated, manufactured, and measured a test antenna (Fig. 3).

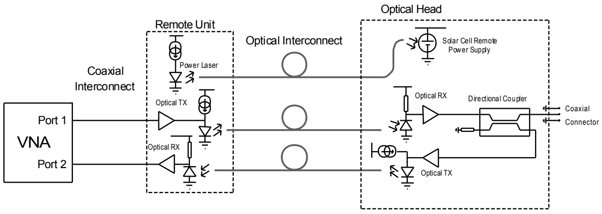

Figure 1. Schematic diagram of the miniature active fiber-optic port extension for S-parameter measurement of electrically small antennas.

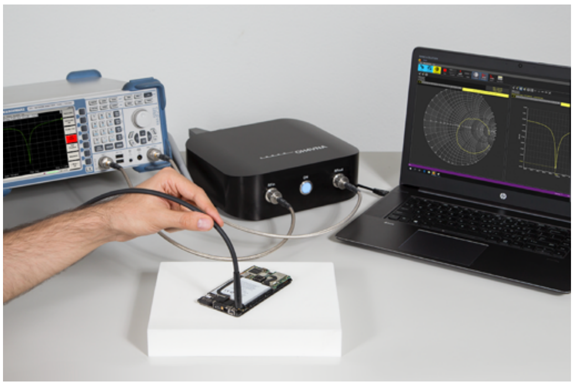

Figure 2. OH4VNA measurement system

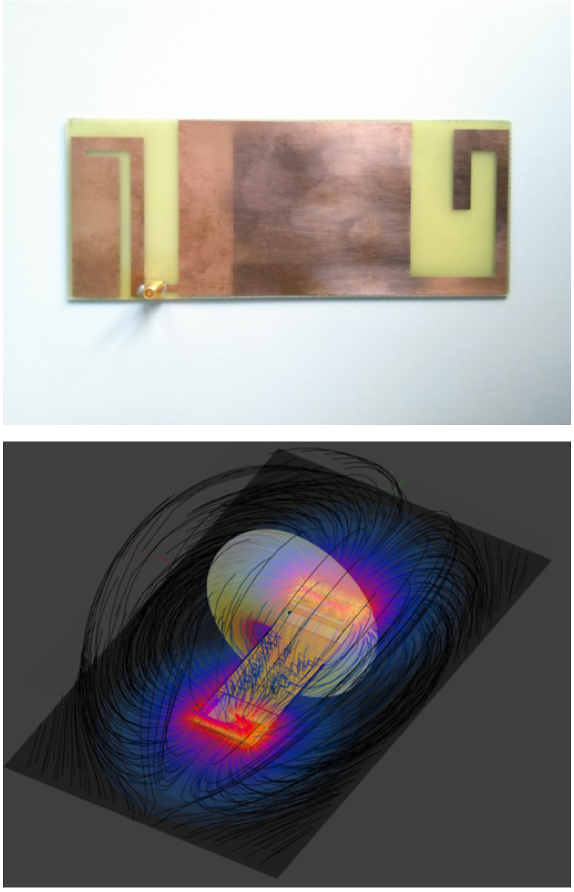

Figure 3. Manufactured (top) and simulated (bottom) model of the test antenna.

3. Results

The test antenna was simulated using SIM4LIFE by ZMT Zurich MedTech AG. We used a network analyzer with a cable connected to measure the antenna feed point impedance. Figure 4 shows the results of the complex impedance measurement using the traditional method with an RF coaxial cable connected to the antenna compared to the simulated results. It is evident that the connected cable significantly modifies the impedance measurement results.

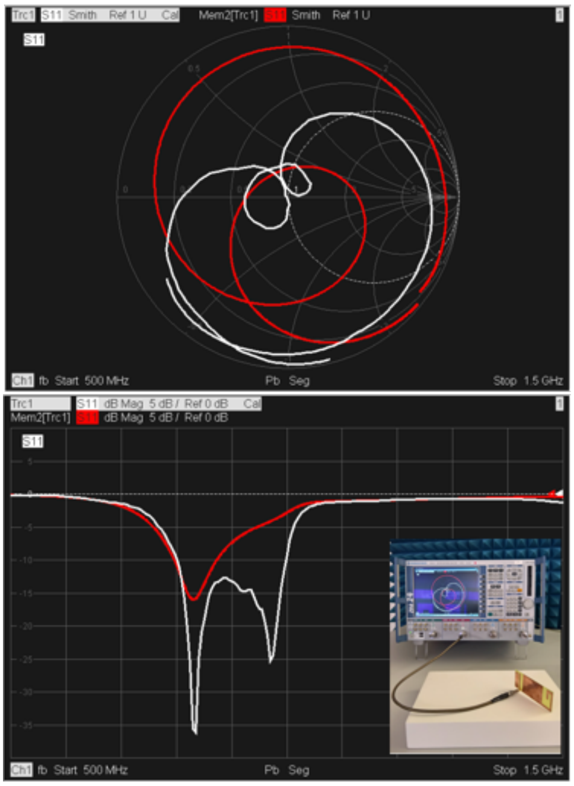

Figure 4. Comparison of the simulated antenna S11 (red) with the measured S11 (white) using a traditional VNA and RF cable setup.

Fig 5 shows the antenna measurement setup and S11 results when OH4VNA is used to measure the electrically small antenna. In this case, the effect of the RF cable on the antenna is removed and the measured complex S11 matches with the simulated results within a small phase-shift due to the RF connector used.

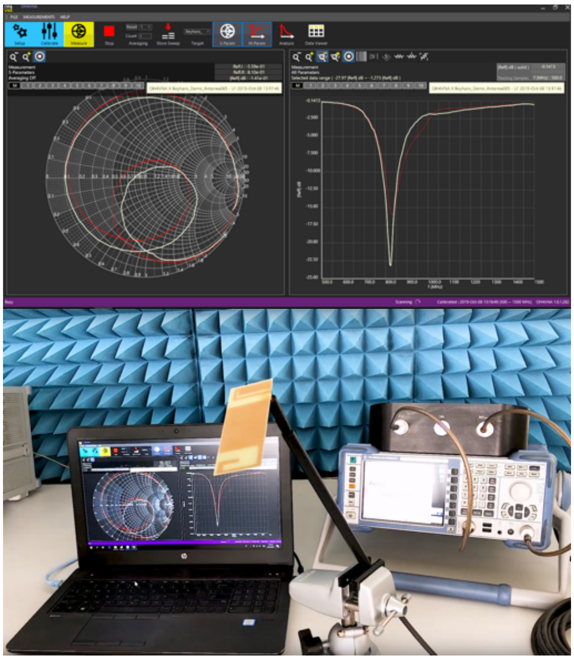

Figure 5. S11 measurement setup with OH4VNA (bottom) and S11 measurement results when measured with OH4VNA (white) in comparison to the simulation results (red).

4. Conclusions

This paper demonstrates an exclusively optical system to measure the complex-valued impedance of electrically small antennas without perturbation of connected cables.

Based on a modeled handset antenna, we demonstrated the influence of a connected cable on the impedance measurement results.

We demonstrated that cable effects when measuring electrically small antennas can be removed with the optical impedance measurement system

References

[1] A. Kramer, P. Muller, U. Lott, N. Kuster, and F. Bomholt, “Electro-optic fiber sensor for amplitude and phase detection of radiofrequency electromagnetic fields,” *Optics letters,* vol. 31, no. 16, p. 2402–2404, 2006

Alternative Cable to Antenna Gain Measurement System Using Optical Fiber Link Technologies

Yuanfeng SHE[1], Michitaka AMEYA[1] and Satoru KUROKAWA[1]
[1]NMIJ, AIST, 305-8563 Tsukuba, Ibaraki, Japan
*Corresponding author: yuanfeng.she@aist.go.jp

Abstract – This article introduced the optical fiber as the alternative to the coaxial cable in the extrapolation method measurement system using the optical fiber link technologies. The gain of the antennas has been measured by the proposed optical fiber link system in the 26.5 – 40 GHz band. The proposed system is a reliable candidate for the antenna gain measurement system.

Keywords – coaxial cable; gain; optical fiber link; extrapolation method

1. Introduction

The 5G mobile network in Japan service uses frequencies up to 40 GHz band [1]. The measurement demand for the 40 GHz antennas has become very large. However, the aging cables have large transmission loss and bad stability. [2] If the transmission loss is too large, the signal becomes weak to the boundary of the dynamic range of the VNA (Vector Network Analyzer), which will cause inaccurate measurement.

This article gives the optical fiber as an alternative to the coaxial cable for the antenna gain system in the 26.5 – 40 GHz band.

2. System

Fig.1 shows the extrapolation method measurement system for the antenna calibration. It needs a 10-meter-long cable to the transmitter and a 3-meter-long cable to the receiver. We use optical fiber to the transmitter side. It consists of an electro-absorption modulator (EAM) with K-connector and a photodiode with trans-impedance amplifier (PD-TIA) with K-connector.[3][4]

Fig.2 shows the transmission loss of the introduced system (10 m fiber + 3 m coaxial) and the previous system (13 m coaxial). The optical fiber has a better transmission performance than the coaxial cable in most frequencies except for those around 40 GHz.

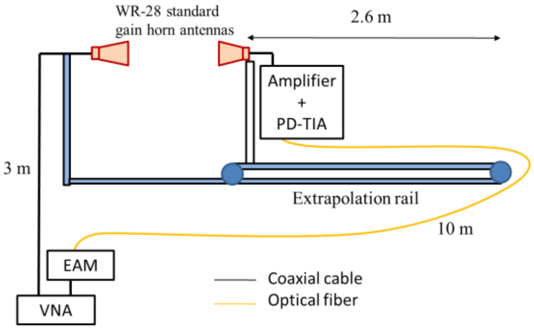

Figure 1. Extrapolation method measurement system using optical fiber link technologies

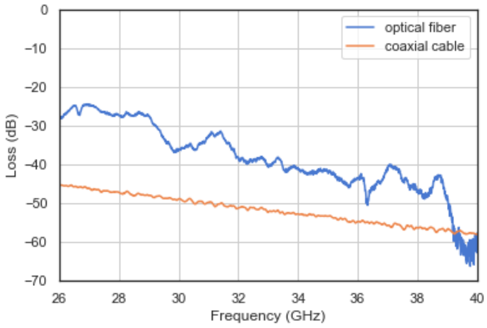

Figure 2. Transmission loss of optical fiber and coaxial cable

3. Measurement

The information of the antennas under test is as follows:

Standard horn: MI Technologies

Model: 12A-26

Aperture size: 69 mm x 56 mm

Wall thickness: 1.5 mm

Nominal gain: 24.7 dBi

Waveguide: WR28

Both the transmitter and the receiver antennas are the same series with the same nominal gain. We did a simple testing experiment.

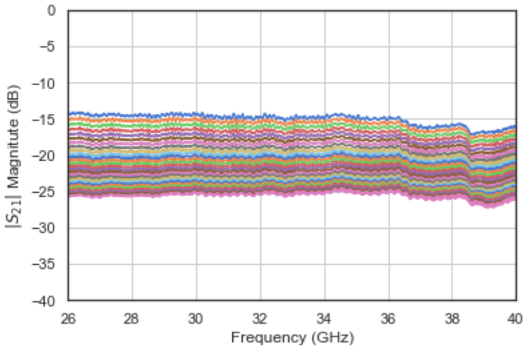

Figure 3. Measured $|S_{21}|$ of two antennas at different distances in extrapolation rail

Fig.3 is the magnitude of S_{21} measured by the VNA, which shows the transmission characteristics. The gain products of both antennas are obtained as in Equation (1). R is the distance of the antennas; $S_{21}(R)$ is the transmission characteristics at different distances. λ is the wavelength; Γ is the reflection.

$$G_1 G_2 = \lim_{R\to\infty} \left(\frac{4\pi R S_{21}(R)}{\lambda(1-\Gamma^2)^2}\right)^2 \qquad (1)$$

Fig.4 shows the linear fitting by different polynomial functions for the gain product at 40 GHz. The blue dots are the measured values. The lines are results of the linear least square fitting curves of different polynomial functions. The gain product of the antennas is the intercept of the curve respectively. We use the linear fitting function as the red line for the experimental results.

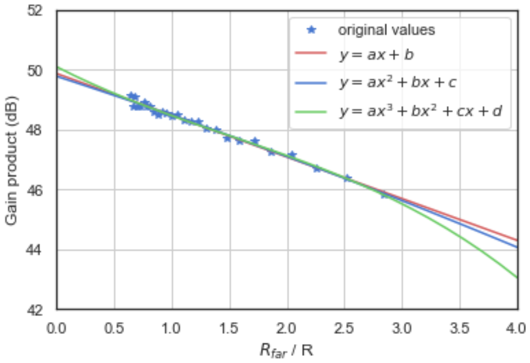

Figure 4. Linear fitting by different polynomial functions for gain product at 40 GHz

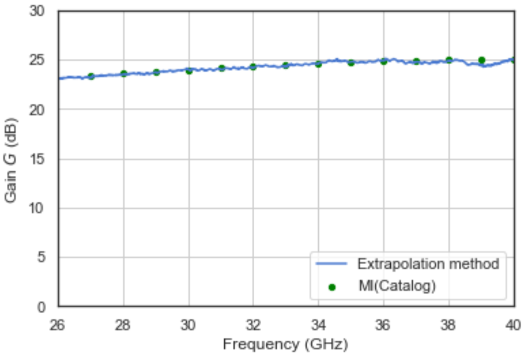

Figure 5. Experiment result of gain and the reference data of catalog.

Fig.5 shows the experiment result of gain and the reference data of the catalog from 26.5 GHz to 40 GHz. The results show us that optical fiber can be a good substitute for coaxial cable.

4. Conclutions

The gain of the antennas has been measured by the proposed optical fiber link system in the 26.5 – 40 GHz band. The proposed system is still under testing and needs to be improved. The reliability of the new system still needs further discussion. But according to this experiment, we think optical fiber is a good substitute for coaxial.

References

[1] Leading towards Next Generation "5G" Mobile Services. Federal Communications Commission, https://www.fcc.gov/news-events/blog/2015/08/03/leading-towardsnext-generation-5g-mobile-services.

[2] She YF, Ameya M, Hirose M, Kurokawa S, Hirokawa J, Ando M. Stability of Coaxial Cable Transmission and Measurement System Using Optical Fiber Link Technologies. Microwave Opt. Technol. Lett. 2017; 59(1): 201–204.

[3] Kurokawa S, Hirose M, Toba Y. Antenna Measrument system Using Bi-directional Optical Fiber Link system. In Proc. EuMC 2016, Oct. 2016.

[4] Kurokawa S, Hirose M, Nishikawa K. Antenna Measurement System using Low Power Consumption Optical Fiber Link up to 40 GHz. International Symposium on Antennas and Propagation (ISAP) 2019.

Electromagnetic environment for a wireless medical telemeter due to surrounding walls

Isao KAYANO[1*], Hisashi MIYAZAKI[1], Takakiyo YAMAMOTO[1], Naoki TAKAHASHI[1],
Aya TAKAYAMA[2] and Seiichi MOCHIZUKI[1]
[1]Department of Medical Engineering, Kawasaki University of Medical Welfare, 701-0193 Okayama, Japan
[2] Kawasaki Medical School Hospital, 701-0192 Okayama, Japan
*Corresponding author: kayano@me.kawasaki-m.ac.jp

Abstract – A wireless medical telemeter, which can remotely monitor a patient's biological information, has been utilized by 80.1% of hospitals in Japan. However, there are some problems such as poor reception conditions, and thus appropriate solutions are needed. In this study, we investigated the electromagnetic interference on a medical telemeter due to the surrounding structures such as walls in a hospital. The measured electromagnetic field in the building with a mesh showed , that the radio waves were attenuated by up to 13% due to the radio wave reflections by the surrounding walls.

Keywords – wireless medical telemeter; EMC; electromagnetic interference

1. Introduction

Wireless medical telemeters that can remotely monitor patients' biological information have been widely used in Japan, 80.1% of hospitals have installed telemeters in 2020; however, 40.9% of them have experienced problems related to radio waves [1, 2].

In this study, we aimed to quantitatively examine the changes in electromagnetic environment caused by the surrounding structures such as walls and measured the electromagnetic fields emitted from medical telemeters either indoors or outdoors. We also experimentally verified the effects of the indoor structures on the electromagnetic environment.

2. Methods

We measured at the center of our university athletic field (Figure 1, outdoor) and inside a classroom with two walls nearby (Figure 1, indoor). In the outdoor setup, a wireless medical telemeter transmitter was placed beside a subject lying on a bed (Figure 1, outdoor) with the transmitter as a reference point, and channel 6003 (420.50 MHz) was measured using a spectrum analyzer (MSA538E; Micronics, Japan) with a mesh every 250 mm from 1000 mm to 4000 mm in the x-direction and from 1000 mm to 5000 mm in the y-direction from the reference point. In the indoor setup, the same mesh area as the outdoor setup was allocated as shown in Figure 3 with the corner the walls as a reference point.

(outdoor)

(indoor)

Figure 1. Experimental setup for outdoors and indoors

3. Results

In the outdoor setup, the received field strength decreased with increasing distance from the telemeter (Figure 2). Similarly, in the indoor setup, the field strength decreased with distance; however, there were also some locations where the received field strength increased or decreased regardless of the distance from the telemeter (Figure 3). The values in Figures 2 and 3 indicate the electric field strength [dBμV/m], respectively.

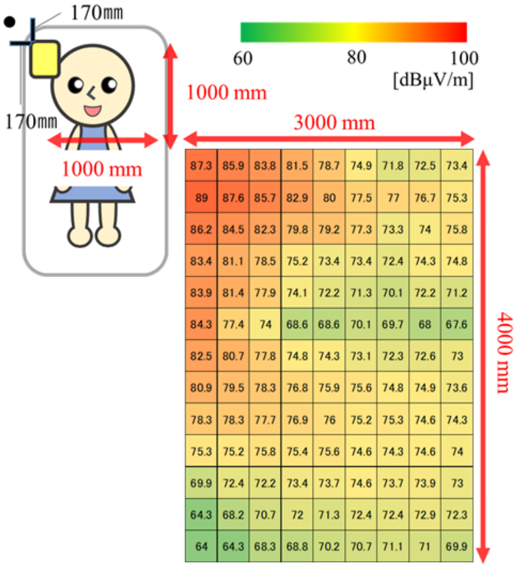

87.3	85.9	83.8	81.5	78.7	74.9	71.8	72.5	73.4
89	87.6	85.7	82.9	80	77.5	77	76.7	75.3
86.2	84.5	82.3	79.8	79.2	77.3	73.3	74	75.8
83.4	81.1	78.5	75.2	73.4	73.4	72.4	74.3	74.8
83.9	81.4	77.9	74.1	72.2	71.3	70.1	72.2	71.2
84.3	77.4	74	68.6	68.6	70.1	69.7	68	67.6
82.5	80.7	77.8	74.8	74.3	73.1	72.3	72.6	73
80.9	79.5	78.3	76.8	75.9	75.6	74.8	74.9	73.6
78.3	78.3	77.7	76.9	76	75.2	75.3	74.6	74.3
75.3	75.2	75.8	75.4	75.6	74.6	74.3	74.6	74
69.9	72.4	72.2	73.4	73.7	74.6	73.7	73.9	73
64.3	68.2	70.7	72	71.3	72.4	72.4	72.9	72.3
64	64.3	68.3	68.8	70.2	70.7	71.1	71	69.9

Figure 2. Result of the outdoor measurement

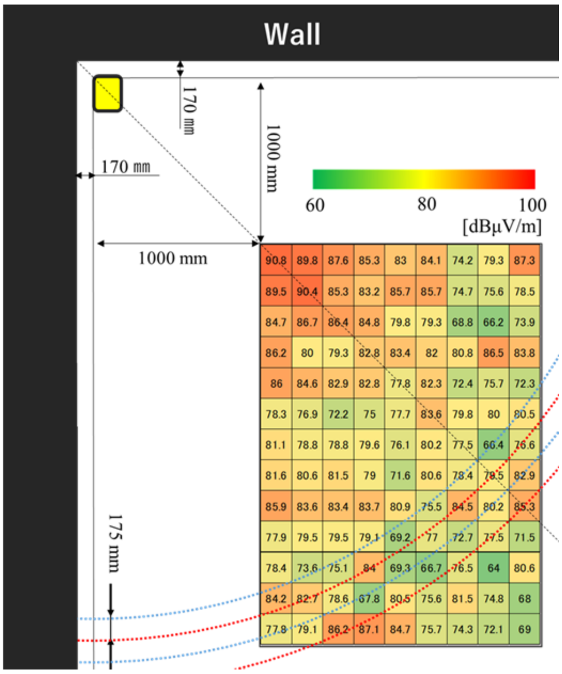

90.8	89.8	87.6	85.3	83	84.1	74.2	79.3	87.3
89.5	90.4	85.3	83.2	85.7	85.7	74.7	75.6	78.5
84.7	86.7	86.4	84.8	79.8	79.3	68.8	66.2	73.9
86.2	80	79.3	82.8	83.4	82	80.8	86.5	83.8
86	84.6	82.9	82.8	77.8	82.3	72.4	75.7	72.3
78.3	76.9	72.2	75	77.7	83.6	79.8	80	80.5
81.1	78.8	78.8	79.6	76.1	80.2	77.5	66.4	76.6
81.6	80.6	81.5	79	71.6	80.6	78.4	78.5	82.9
85.9	83.6	83.4	83.7	80.9	75.5	84.5	80.2	85.3
77.9	79.5	79.5	79.1	69.2	77	72.7	77.5	71.5
78.4	73.6	75.1	84	69.3	66.7	76.5	64	80.6
84.2	82.7	78.6	67.8	80.5	75.6	81.5	74.8	68
77.8	79.1	86.2	87.1	84.7	75.7	74.3	72.1	69

Figure 3. Result of the indoor measurement

4. Discussions

As shown in Figure 3, the electric field strength was +31% at the maximum and -13% at the minimum compared to the same measurement points outdoors as in Figure 2. These discrepancies may be mainly due to the generation of stationary waves caused by the reflection of electromagnetic waves by the indoor structures. The increase and decrease in the electric field strength are estimated to occur in concentric circles, i.e. every half wavelength (about 340 mm) centered on the radiation source. Indeed, the measurement results showed that there were some concentric irregularities every quarter wavelength. Therefore, it is suggested that the poor reception at a particular location be solved by shifting the transmitter a quarter wavelength away from the reference point.

5. Conclusions

We have experimentally examined the difference between indoor and outdoor electromagnetic fields emitted from a wireless medical telemeter. There were some locations indoors where the electromagnetic field was weaker than that outdoors by more than 13% due to the effect of the electromagnetic wave reflection by walls. These data may be useful to properly install reception equipments (such as leaky coaxial cables) in hospitals.

Acknowledgment

This work was supported by JSPS KAKENHI Grant Number 19H03876.

References

[1] Electromagnetic Compatibility Conference Japan [Internet]; 2021 [cited 2021 Aug 18]. Available from: https://www.emcc-info.net/medical_emc/202107/medical_guide_rvsn_20210714.pdf.

[2] Kayano I, Motoishi T, Nishie K, Takayama A, Mochizuki S. Experimental and Theoretical Studies on Communicable Distance for Medical Telemeters between Hospitals Located with a Distance of 1,300 Meters. 2020 International symposium on antennas and propagation (ISAP) Jan 25-28, 2021, Online, pp.639-640.

Exposure Polarization Dependency of Active Implantable Medical Device EMI in 5G Frequency Band

Takuji NISHIKAWA*, Atsuki OHTSUKA, Takashi HIKAGE, and Manabu YAMAMOTO
Graduate School of Information Science and Technology, Hokkaido University, Sapporo 060-0814, Japan
{t_nishikawa, hikage}@wtemc.ist.hokudai.ac.jp

Abstract – The relationship between electromagnetic interference (EMI) characteristics of implantable medical devices and polarization of RF both under near- and far-fields exposure conditions is investigated using numerical simulation. As a numerical model, we prepare an implantable pacemaker embedded in a human phantom used in EMI evaluation tests and analyze the AIMD-EMI characteristics near the transmitter in the 5G Sub6 frequency band by conducting electromagnetic field simulations based on the finite element method.

Keywords – Active Implantable Medical Device; EMI; FEM; Interference voltage

1. Introduction

Wireless devices have potentially trigger electromagnetic interference (EMI) in other electric appliances. EMI impacting implantable medical devices (AIMD) such as implantable cardiac pacemakers and implantable cardioverter defibrillators (ICDs) is one of the most critical issues needing investigation [1-3]. Recently, the use of the fifth-generation mobile communication system (5G) is expanding, but the EMI characteristics for AIMD in the high-frequency band used in this system have not been sufficiently investigated. Although there are some reports on evaluating interference voltage in pacemaker circuits using numerical simulations [4-6], there are not many on the relationship between polarization and interference voltage. In this paper, the EMI characteristics for each polarization near the antenna in the 5G Sub6 frequency band (3.7GHz, 4.5GHz) are analyzed by electromagnetic field simulation based on the finite element method (FEM) using a numerical model of a pacemaker and a flat torso phantom for pacemaker EMI testing.

2. Simulation Model and Condition for Interference Voltage Estimation

The pacemaker EMI evaluation test for mobile devices is performed using the flat torso phantom shown in Fig.1(a). This phantom is developed based on Irnich's model [1]. It is composed of an acrylic case and saline solution (NaCl 1.8g/l). The pacemaker should be placed on the holding panel so that its upper surface is 5 mm from the phantom surface. The numerical model simulates the experimental model, as shown in Fig.1(b). In this pacemaker model, a ventricular lead (VVI mode) is connected to the pacemaker body (CAN), and its shape and size are reproduced based on the actual device.

Additionally, it substitutes the internal circuitry with a terminating resistor. The voltage induced in its resistor is evaluated as interference voltage. Also, the antenna used for the experiment and analysis is a half-wavelength dipole antenna.

The electromagnetic field simulation is performed using a FEM solver of the commercial simulator, PathWave EM Design (EMPro) [7]. The center of the antenna is placed in line with the center of the pacemaker connector. The interference voltage at the termination resistor is evaluated by FEM-based analysis. Next, the antenna position is varied in the x-axis direction by 10 mm within a range of ±80 mm, as shown in Figure 2. Then, when the calculation is completed at all points, the polarization is rotated at 45 degrees intervals and analyzed in the same way. Now, the x-axis direction in Figure 2 is 0 degrees, and counterclockwise is positive. The solver is the direct analysis method for the analysis conditions, and the order is second order. The electrical constants are shown in Table 2. Note that the properties of the Saline solution vary with frequency.

3. Results and Conclusions

The analysis results at 3.7 GHz from 0° to 135° in 45° increments are shown in Figure 2. In all cases, the interference voltage has a maximum value around -10 mm to 0 mm where the connector part is located. The maximum value is different for each polarization, being the largest at 90° and the smallest at 45°. The gap between the peak values is about 1.5 times. The peak values for 90° and 135° are almost the same in magnitude, but the voltage becomes larger for 90° when the antenna position is on the minus side and larger for 135° when the antenna position is on the plus side. The reason for this is that the connector part is curved, which may change the state of the electric field coupling.

We investigated the interference voltage when the antenna was placed near the AIMD to consider antenna position and polarization dependencies on EMI characteristics. As a result, we found that the peak value and the coupling characteristics depending upon the polarization.

In the future, we plan to analyze the case at other frequencies and study them in more detail based on the electric field distribution and other factors.

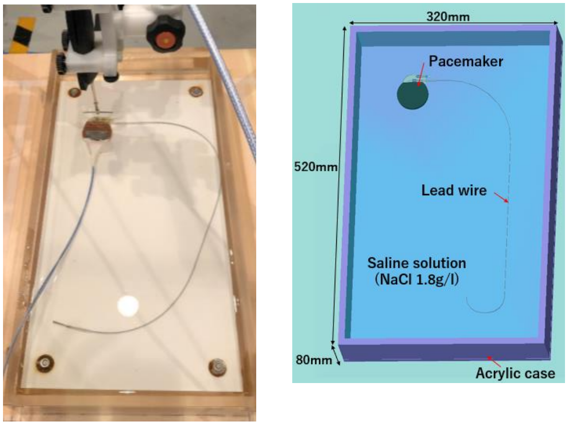

(a)Experimental model (b)Numerical model

Figure 1. Flat torso phantom for pacemaker EMI estimation

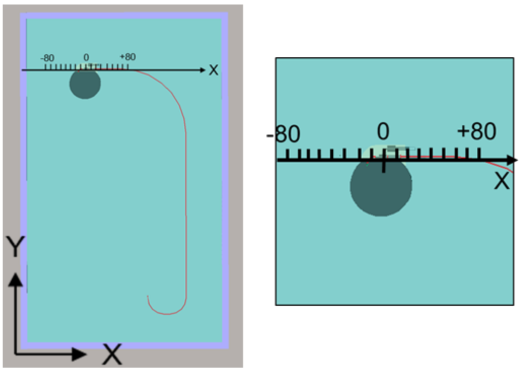

Figure 2. Antenna position

Table 1. FEM simulation specifications

FEM Solver	Direct Solver
Order of Basis Function	2nd
Boundary Condition	Absorbing
Estimation Frequency	3.7, 4.5 [GHz]
FEM Mesh	Cond. Edge: 0.2 × estimation conductor width Cond. Vertex: 0.2 × 0.3 × estimation conductor width

Table 2. Electrical constants

Material		ε r	σ (S/m)
Pacemaker CAN, Lead		Perfect Electric Conductor (P.E.C.)	
Saline Solution (1.8g/l)	3.7GHz	76.89	2.966
	4.5GHz	75.81	4.349
Silicone		2.7	0
Acrylic Case		3	0

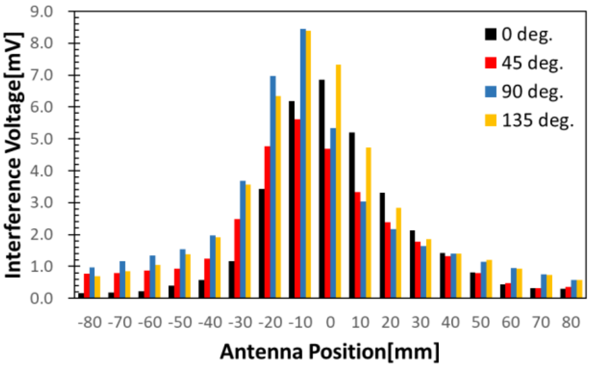

Figure 3. Relationship between antenna position and interference voltage at 45deg. and 90deg. (3.7GHz)

Acknowledgment

This work was partially supported by JSPS KAKENHI JP19K04504.

References

[1] W. Irnich, L. Bats, R. Muller, and R. Tobisch, "Electromagnetic interference of pacemaker by mobile phones", PACE, vol. 19, pp. 1431-1446, Nov. 1996.

[2] T. Toyoshima, M. Tsumura, T. Nojima and Y. Tarusawa, “ Electromagnetic interference of implantable cardiac pacemakers by portable telephones,” Japanese J. Cardiac Pacing and Electrophysiology, vol. 12, no.5, pp. 488-497, 1996.

[3] S. J Seidman, R. Brockman, B. M. Lewis, J. Guag, M. J Shein, W. J Clement, J. Kippola, D. Digby, C. Barber, D. Huntwork: “In vitro tests reveal sample radiofrequency identification readers inducing clinically significant electromagnetic interference to implantable pacemakers and implantable cardioverter-defibrillators,” Heart Rhythm, vol.7(1), pp.99-107, 2010.

[4] S. Futatsumori, Y. Kawamura, T. Hikage, T. Nojima, B. Koike, H. Fujimoto, T. Toyoshima, “"In vitro Assessment of Electromagnetic Interference Due to Low-Band RFID reader/writers on Active Implantable Medical Devices", Journal of Arrhythmia, Vol.25, No. 3, pp. 142-152, Jan. 2010.

[5] N. Tanaka, T. Hikage, T. Nojima: "FEM Simulations of Implantable Cardiac Pacemaker EMI Triggered by HF-Band Wireless Power Transfer System, "IEICE TRANSACTIONS on Electronics, Vol.E99-C, No.7, pp.809-812, July 2016.

[6] S. ITO, J. SUN, T. HIKAGE, J. HIAGASHIYAMA, T. ONISHI: " Interference Voltage Measurement Set-up for Beam-Type WPT Using an Electro-Optic Converter for Active Implantable Medical Device EMI Assessment," proc. of 3rd PEM International Workshop in Ise (PEM2019),PE-10, pp.1-3, Nov. 2019.

[7] https://www.keysight.com/us/en/lib/resources/software-releases/pathwave-em-design-empro-2020.html

Characterization of Human Body Blockage in 5G Frequency Bands for Epidemiologic Research on Association Between Radio Frequency Wave Exposure and Children Health

Kohei YAMAMOTO[1*], Ryunosuke OZAKI[1], Takashi HIKAGE[1], Keiko YAMAZAKI[2],
Atsuko ARAKI[2], Chihiro MIYASHITA[2], Naomi TAMURA[2], and Reiko KISHI[2]
[1]Graduate School of Information Science and Technology, Hokkaido University, 〒060-0814, Sapporo, Japan
[2]Center for Environmental and Health Sciences, Hokkaido University, 〒060-0812, Sapporo, Japan
{k_yamamoto, hikage}@wtemc.ist.hokudai.ac.jp

Abstract – Children and adolescents are much more often exposed to RF-EMF due to spreading smartphones and other wireless devices and declining the age of starting to use these devices. It is required to accumulate epidemiologic research data about the effect on children's higher nerve functions by RF exposure in the general environment. To develop a novel exposure dosimetry model for the epidemiologic research, we evaluate the effect of human body blockage on reception characteristics at 5G Sub6 frequencies by using three-dimensional full-wave numerical simulation based on the finite-difference time-domain (FDTD) method.

Keywords – RF-EMF; SAR; Human body blockage; Exposure dosimetry; FDTD Method

1. Introduction

In recent years, the age of starting to use wireless devices such as smartphones is declining. Additionally, a growing number of wireless LAN systems are installed indoors so that children and adolescents are much more often exposed to RF-EMF (Radio Frequency Electro Magnetic Fields). Hence, it is required to accumulate epidemiological research data about the effect on the development of children's nerves due to RF exposure in the general environment.

There are several previous studies [1-4] about that, but there is no concrete conclusion about the effect on children's health, such as higher nerve functions by RF exposure. Moreover, there has been no research reported in Japan.

The Epidemiologic research to evaluate the effect on adolescent's health due to RF exposure using prospective cohort study design is now being carried out by the research group of Hokkaido University [5-7]. Since accurate RF exposure dosimetry is crucial in this research, we quantitatively measure RF exposure in the living environment by having subjects carry a portable EMF device [8]. The Received EMF intensity of this device includes the effect of human body blockage of the subjects. Therefore, it is important to understand the characteristics of human body blockage to accurate exposure dosimetry.

In this study, we evaluate the effect of human body blockage on its reception characteristics due to deploying an EMF device near the subject's body. The Finite-difference time-domain (FDTD) method solver is used for the analysis.

2. Estimation model of human body blockage characteristics by numerical analysis

Here, we use a numerical human of a 6-year-old boy [9], as shown in Figure1. The EMF device carried by the subjects has a triaxial isotropic antenna and records synthesized EMF intensities of each direction. In the simulation, a spatial sensor simulating the dimensions of the EMF device and a point sensor simulating the receiving antenna is set up to obtain the electromagnetic fields, and human body blockage characteristics are evaluated using

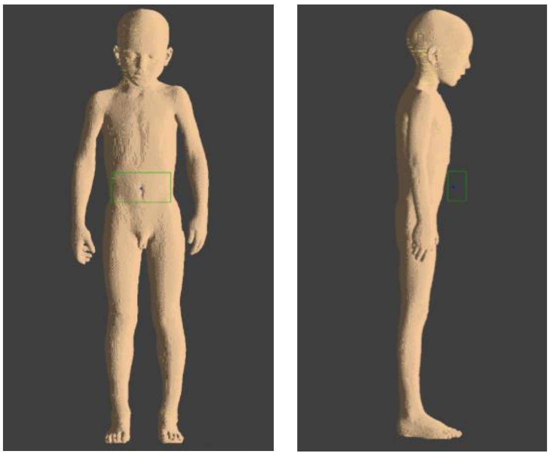

Figure 1. Numerical human model

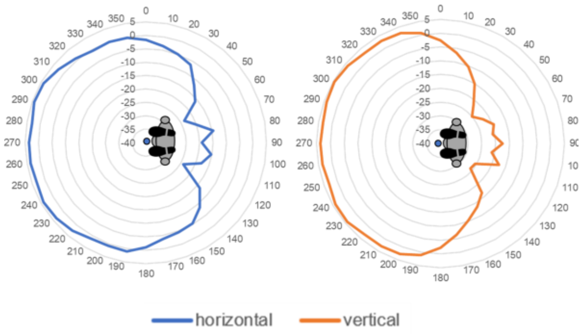

Figure 2. Estimation results (@3.7GHz)

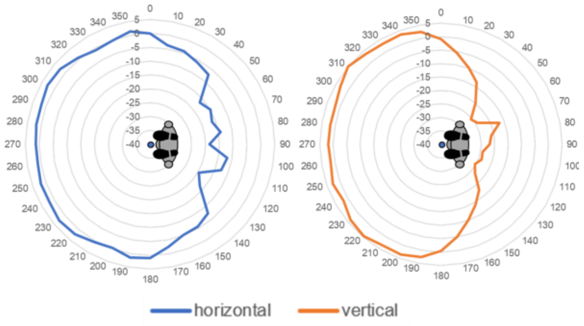

Figure 3. Estimation results (@4.5GHz)

the electric field strength at the point. The evaluation point is placed on the midline of the front of the human abdomen. The distance between the evaluation point and the human body surface is 28mm.

3. Results

Using the simulation model shown in the previous section, we evaluate the human body blockage characteristics by changing the direction of the exposure plane wave in 10-degree steps. We analyze each case that the direction of oscillation of the electric field is vertical and horizontal at 3.7GHz and 4.5GHz. The human model assumes the electrical constants of each biological tissue in each 5G Sub-6 GHz frequency band. The estimation results at 3.7GHz and 4.5GHz are shown in Figure2 and Figure3, respectively. The dosimetry protocol for epidemiological studies on RF exposure and adolescent health will be discussed based on the estimation results.

Acknowledgements

This work was supported by Ministry of Internal Affairs and Communications Grant Number JPMI10001.

References

[1] Abramson, M. J., Benke, G. P., Dimitriadis, C., Inyang, I. O., Sim, M. R., Wolfe, R. S., & Croft, R. J.:"Mobile telephone use is associated with changes in cognitive function in young adolescents," Bioelectromagnetics, 30(8), 678-686 (2009).

[2] Divan, H. A., Kheifets, L., Obel, C., & Olsen, J.:"Cell phone use and behavioural problems in young children." Journal of Epidemiology and Community Health, 66(6), 524-529 (2012).

[3] Schoeni, A., Roser, K., & Roosli, M.:"Memory performance, wireless communication and exposure to radiofrequency electromagnetic fields: A prospective cohort study in adolescents," Environment International, 85, 343-351 (2015).

[4] Birks, L. E., Struchen, B., Eeftens, M., van Wel, L., Huss, A., Gajsek, P., . . . Guxens, M. :"Spatial and temporal variability of personal environmental exposure to radio frequency electromagnetic fields in children in Europe," Environ Int, 117, 204-214 (2018).

[5] Keiko Yamazaki, Atsuko Araki, Chihiro Miyashita, Sachiko Itoh, Sonomi Nakajima, Reiko Kishi, "ERP P3 during visual 3-stimulus oddball task and intelligence at school aged children: the Hokkaido Study" 26th Annual Meeting of Cognitive Neuroscience Society, Mar 2-5. 2019 (virtual).

[6] R. Ozaki et al., The Philippines-Japan Workshop on Wireless, Radio and Antenna Technologies, Dec. 2019.

[7] Toru Ishihara, Keiko Yamazaki, Atsuko Araki, Yuri Teraoka, Naomi Tamura, Takashi Hikage, Manabu Omiya, Masahiro Mizuta, Reiko Kishi: Exposure to Radiofrequency Electromagnetic Field in the HighFrequency Band and Cognitive Function in Children and Adolescents: A Literature Review," International Journal of Environmental Research and Public Health, 17(24), 9179, Dec. 2020.

[8] https://fieldsatwork.ch

[9] https://itis.swiss/virtual-population/virtual-population/

Numerical Estimation of Indoor Propagation Characteristics Considering Shadowing due to Human Bodies in Local-5G Frequency Band

Kazuki YOSHIDA[1*], Takashi HIKAGE[1], Manabu YAMAMOTO[1], and Manabu OMIYA[2]
[1]Graduate School of Information Science and Technology, Hokkaido University, 〒060-0814, Sapporo, Japan
[2]Information Initiative Center, Hokkaido University, 〒060-0808, Sapporo, Japan
{k_yoshida, hikage}@wtemc.ist.hokudai.ac.jp

Abstract – This study focuses on human body shadowing on the propagation characteristics of local-5G frequency bands in indoor environments. We modeled an indoor propagation environment assuming a conference room containing human bodies and evaluated the propagation characteristics through a large-scale 3D numerical analysis based on the FDTD method. The electric field distribution in the conference room environment exited by the 4.7GHz transmitting antenna, which is used as the local-5G frequency, was calculated, and the propagation characteristics with and without the human bodies were compared. Shadowing and scattering effects due to multiple human bodies in standing and sitting postures were evaluated in the simulations.

Keywords – Human body shadowing; Propagation characteristics; FDTD method; Local-5G frequency band

1. Introduction

With the rapid progress of wireless communication technology and the sophistication and diversification of people's needs for wireless services, communication speeds have been increasing, and the volume of information has increased. Currently, communication needs are diversifying, as typified by the spread of IoT, and it is assumed that they will become even more diversified in the 5G era. In addition, the development and verification of local 5G, a 5G system that can be flexibly constructed on a spot basis within the premises of local companies, local governments, and other various entities following the individual needs of communities and industries, has been carried out [1].

This study uses the FDTD method to evaluate the propagation characteristics in the 4.7 GHz band used in local 5G. In evaluating propagation characteristics in an indoor environment, it is necessary to take into account the effects of absorption and shadowing of radio waves by the human body [2-5]. In addition, the propagation characteristics in an actual indoor environment are complex and multi-reflective because of the reflected waves from the surrounding fixtures and walls. In this paper, we evaluate the radio propagation characteristics in the 4.7GHz band in a conference room environment.

2. Estimation model for indoor propagation characteristics including multiple humans

The conference room model used in the evaluation and the location of the transmitting antenna is shown in Fig. 1. The model is based on an actual conference room in the building of Hokkaido university, which includes a projector, desk, chair, blackboard, and screen. The dimensions are 7500 mm in the x-direction, 7000 mm in the y-direction (1500 mm at the veranda), and 3510 mm in the z-direction. As shown in the figure, the transmitting antenna was placed at the height of 2.0 m from the floor and set as vertical polarization parallel to the z-axis direction. The discussion will compare the case where the humans [6] exist in the conference room and the case where no one exists. We achieved FDTD simulation to obtain and evaluate the electric field distribution.

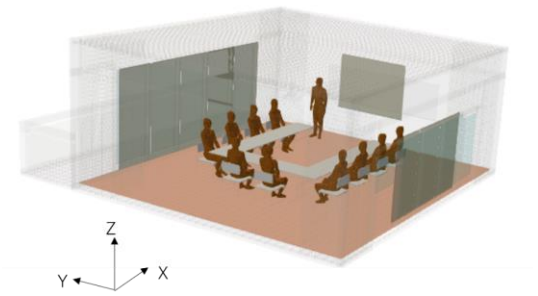

(a) Model Overview

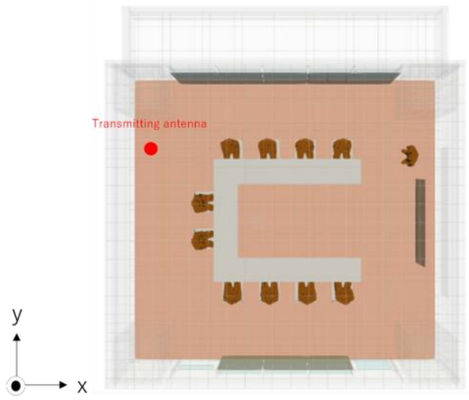

(b) View from above

Fig.1 Conference room model

3. Results and Summary

Examples of simulated results of electric field distributions are shown in Fig. 2. Here, Fig. 2 (b) shows 2-dimensional field distribution in the xy-plane. It could be clearly found that the value of the electric field was slightly lower due to the effect of shadowing when many humans exited. Also, Fig. 2 (d) shows the distributions in the xz-plane; from the figure, radio waves propagated between human bodies due to multipath effects caused by transmission, diffraction, and reflection. It can also be seen that the electric field values are generally lower when the height is 80 cm than when the height is 120 cm because the distance from the antenna is farther.

This paper evaluated the effect of human shadowing on the propagation characteristics of the local-5G frequency band 4.7GHz in the indoor environment. FDTD simulation was used to obtain the electric field distribution in a conference room, and we discussed the effect of human shadowing. In the future, we plan to conduct simulations in urban areas to evaluate and study the propagation characteristics over a wider area.

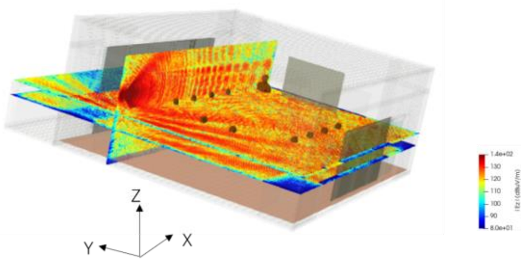

(a) Overview of field distribution

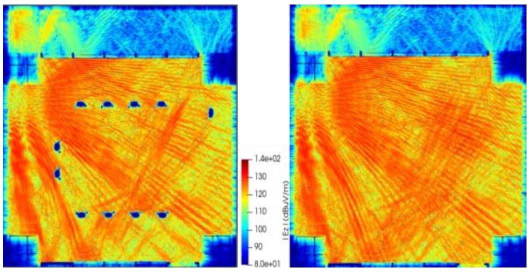

(b)xy plane at 80cm

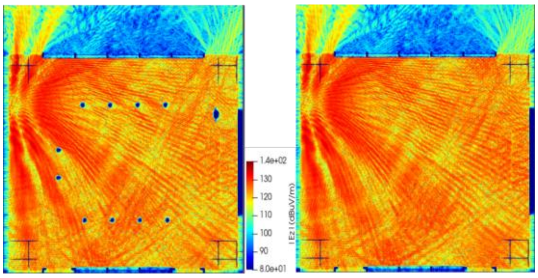

(c)xy plane at 120cm

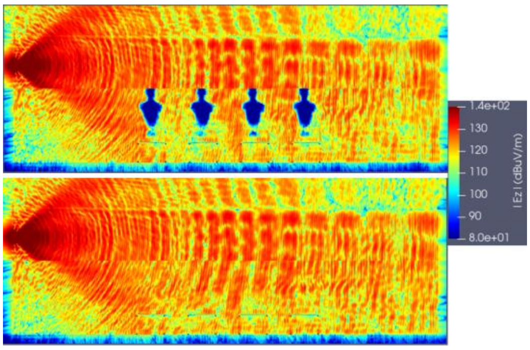

(d)xz plane

Fig.2 Estimation Results

Acknowledgments

This work was supported by JSPS KAKENHI Grant Numbers 19K04385, 19K04504.

References

[1] https://www.soumu.go.jp/menu_news/s-
[2] news/01ryutsu06_02000291.html
[3] L. Harris et al., "Using Large-Scale FDTD Method to Obtain Precise Numerical Estimation of Indoor Wireless Local Area Network Office Environment," IEICE Trans. On Fundamentals, Vol. E92-A, No.9, Sep. 2009.
[4] T. Sekiguchi et al., "Numerical Estimation of Indoor Propagation Characteristics for Microwave Wireless Power Transfer," proc. of 2018 Asian Wireless Power Transfer Workshop (AWPT2018), SA-5-O1, Nov. 2018.
[5] T. Hikage, "Numerical Estimation on Indoor Propagation Characteristics for RF Wireless Power Transfer," proc. of 2019 URSI Asia-Pacific Radio Science Conference (AP-RASC 2019), We-DO6-4, Mar. 2019.
[6] Electromagnetic Compatibility Laboratory Biomedical EMC. Available from: https://emc.nict.go.jp/bio/model/model01_1.html

[Invited Talk] Optical MIMO Signal Processing Based on Planar Lightwave Circuit

Takanori Sato*
Graduate School of Information Science and Technology, Hokkaido University, 060-0814, Sapporo, Japan
*Corresponding author: tksato@ist.hokudai.ac.jp

Abstract – Generally, in the mode division multiplexing technology, the multiple-input multiple-output (MIMO) processing is executed by the digital signal processor (DSP). Universal linear optical circuit, which enables the basis conversion of optical signals, can be used as an optical matrix multiplier, namely, simple optical DSP for MIMO. It may overcome the limit of speed and energy consumption in the conventional signal processing because the optic-electric conversion is not required. In this paper, the operation principle of the universal linear optical circuit and its potential are discussed.

Keywords – Optical communication, MIMO signal processing, Universal linear optical circuit.

1. Introduction

Mode division multiplexing (MDM) is a key technology to manage the increasing big data communication. In the optical MDM transmission system, since there are the differential mode delay and the modal crosstalk, their multiple-input multiple-output (MIMO) compensations are required [1]. Generally, in the optical receiver, all multiplexed modes are converted into fundamental modes. After the optic-electric (O/E) conversion by photodetectors, the MIMO compensations are electrically executed by the digital signal processor (DSP). Recently, many types of the optical MIMO device are reported [2]–[5], in which an input multiple optical signals are converted into another one with an arbitrary matrix. It is called a universal linear optical circuit, and it may be called an optical DSP. Such a device can reduce the calculation cost of the electric DSP.

In this paper, an overview of the universal linear optical circuit is written. After explained the principle of the universal linear optical circuit, an example of its applications is demonstrated.

2. Principle of universal linear optical circuit

The universal linear optical circuit is originally proposed by Reck *et al.* in 1994 [6] and is composed of lots of Mach-Zehnder interferometers (MZIs) and phase shifters (PSs). The MZI is an optical power splitting device that has two input ports and two output ports. The 2×2 transfer matrix of the push-pull MZI is expressed as

$$\begin{aligned}\mathbf{T}_{\mathrm{MZI}}(\theta) &= \mathbf{T}_{\mathrm{3dB}}\mathbf{T}_{\mathrm{ARM}}(\theta)\mathbf{T}_{\mathrm{3dB}} \\ &= C_0\begin{pmatrix} \cos\theta & -j\sin\theta \\ -j\sin\theta & \cos\theta \end{pmatrix}\end{aligned} \tag{1}$$

where

$$\mathbf{T}_{\mathrm{3dB}} = \frac{C_1}{\sqrt{2}}\begin{pmatrix} 1 & -j \\ -j & 1 \end{pmatrix}, \tag{2}$$

$$\mathbf{T}_{\mathrm{ARM}}(\theta) = C_2\begin{pmatrix} \exp\left[j\left(\theta+\frac{\pi}{2}\right)\right] & 0 \\ 0 & \exp\left[-j\left(\theta+\frac{\pi}{2}\right)\right] \end{pmatrix}. \tag{3}$$

and C_i is a constant value (loss and phase shift for waveguide propagation) and omitted as below. Whereas, the 2×2 transfer matrix of the PS is expressed as

$$\mathbf{T}_{\mathrm{PS}}(\varphi_1,\varphi_2) = \begin{pmatrix} \exp(-j\varphi_1) & 0 \\ 0 & \exp(-j\varphi_2) \end{pmatrix}. \tag{4}$$

From now, the 2×2 arbitrary optical transformation is explained. Suppose that an arbitrary unitary matrix is given as

$$\mathbf{U}(a,b,c,d) = \begin{pmatrix} a\exp(jb) & a'\exp(jc) \\ a'\exp(jd) & a\exp(j\psi) \end{pmatrix} \tag{5}$$

$$a' = \sqrt{1-a^2} \tag{6}$$

$$\psi = -b+c+d+\pi \tag{7}$$

where a ($0 \leq a \leq 1$), b, c, and d are real variables for giving arbitrary unitary matrix. Here, to apply the Gaussian elimination method, $\mathbf{T}_{\mathrm{MZI}}\mathbf{T}_{\mathrm{PS}}$ is multiplexed to $\mathbf{U}$, namely,

$$\mathbf{X} = \mathbf{T}_{\mathrm{MZI}}(\theta)\mathbf{T}_{\mathrm{PS}}(0,\varphi)\mathbf{U}(a,b,c,d) \tag{8}$$

and the (i, j) element of $\mathbf{X}$ (x_{ij}) is given as

$$x_{11} = a\cos\theta\exp(jb) - ja'\sin\theta\exp\left[j(d-\varphi)\right], \tag{9}$$

$$x_{12} = a'\cos\theta\exp(jc) - ja\sin\theta\exp\left[j(\psi-\varphi)\right], \tag{10}$$

$$x_{21} = -ja\sin\theta\exp(jb) + a'\cos\theta\exp\left[j(d-\varphi)\right], \tag{11}$$

$$x_{22} = -ja'\sin\theta\exp(jc) + a\cos\theta\exp\left[j(\psi-\varphi)\right]. \tag{12}$$

Therefore, the condition to satisfy $x_{21} = 0$ is found as

$$\theta = \tan^{-1}\left(\frac{a'}{a}\right), \qquad \because \begin{cases} a' = \sin\theta \\ a = \cos\theta \end{cases} \tag{13}$$

$$\varphi = d - b - \frac{\pi}{2}. \tag{14}$$

If these values are substituting into Eq. (8), x_{ij} becomes

$$x_{11} = \exp(jb), \tag{15}$$

$$x_{21} = x_{12} = 0, \tag{16}$$

$$x_{22} = -j\exp(jc). \tag{17}$$

Finally, the 2×2 matrix for Gaussian elimination to $\mathbf{U}$ is obtained as

$$\mathbf{U}^{\dagger}(a,b,c,d) = \mathbf{T}_{\mathrm{PS}}\left(-b, -c + \frac{\pi}{2}\right)\mathbf{T}_{\mathrm{MZI}}(\theta)\mathbf{T}_{\mathrm{PS}}(0,\varphi). \tag{18}$$

From the above equation, two PSs and one MZI work as the optical 2×2 unitary converter as shown Fig. 1. Similarly, the n×n conversion can also be done by the cascaded connection of $n(n+1)/2$ PSs and $n(n-1)/2$ MZIs (details are in [6]). For example, the 4×4 converter can be constructed by the configuration as shown in Fig. 2 (a).

Figure 1. Configuration of 2×2 optical unitary conversion.

In 2016, Clements *et al.* proposed the modified configuration of the universal linear optical circuit as shown in Fig. 2(b), corresponding to one just before the final equation in [7]. Compared with Reck's configuration, the imbalance of loss is improved, and the device length is shorter.

Until now, the optical unitary conversion is explained. It is known that non-unitary conversion can be also done [8]. Any matrix $\mathbf{M}$ can be expanded by the singular value decomposition as $\mathbf{M} = \mathbf{USV}^{\dagger}$ where $\mathbf{S}$ is the singular value matrix and $\mathbf{U}$, $\mathbf{V}$ are unitary matrices. $\mathbf{U}$, $\mathbf{V}$ are corresponding to the universal linear optical circuits. On the other hand, the diagonal elements of $\mathbf{S}$ are corresponding to the optical amplifiers or attenuators. Ignoring the loss, $\mathbf{S}$ can be normalized, and thus the optical amplifier is not required. As the result, any optical conversion (matrix multiplication) can be realized.

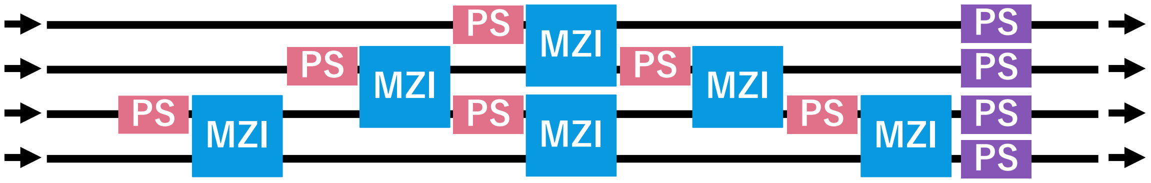

(a) Reck's configuration

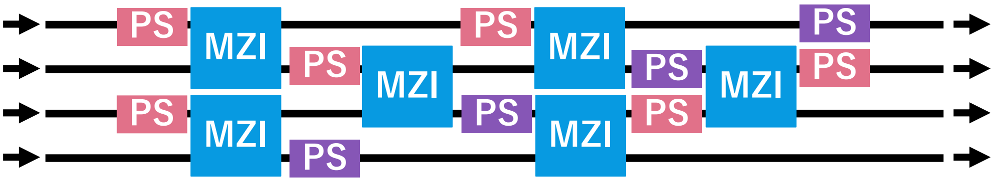

(b) Clements's configuration

Figure 2. Configuration of 4×4 optical unitary conversion.

3. Example of application to MIMO processing

The simplest one of MIMO processing is the matrix multiplication to the multiple signals. As explained in the previous section, the matrix multiplication of optical signals can be executed by universal linear optical circuits and optical attenuators. As shown in Fig. 3, for the MDM transmission, the mixed optical channels can be divided and restored by optical MIMO processor. Fig. 4 shows the example of 3×3 optical MIMO operation, where MZIs and PSs are composed with silicon ring resonators [4]. It is demonstrated that the mixed channels are successfully divided.

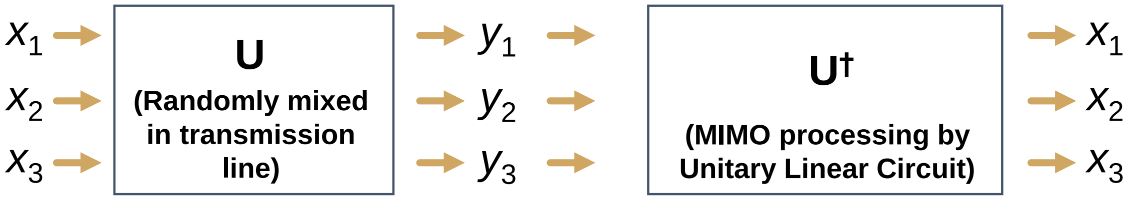

Figure 3. Optical MIMO processing for MDM transmission.

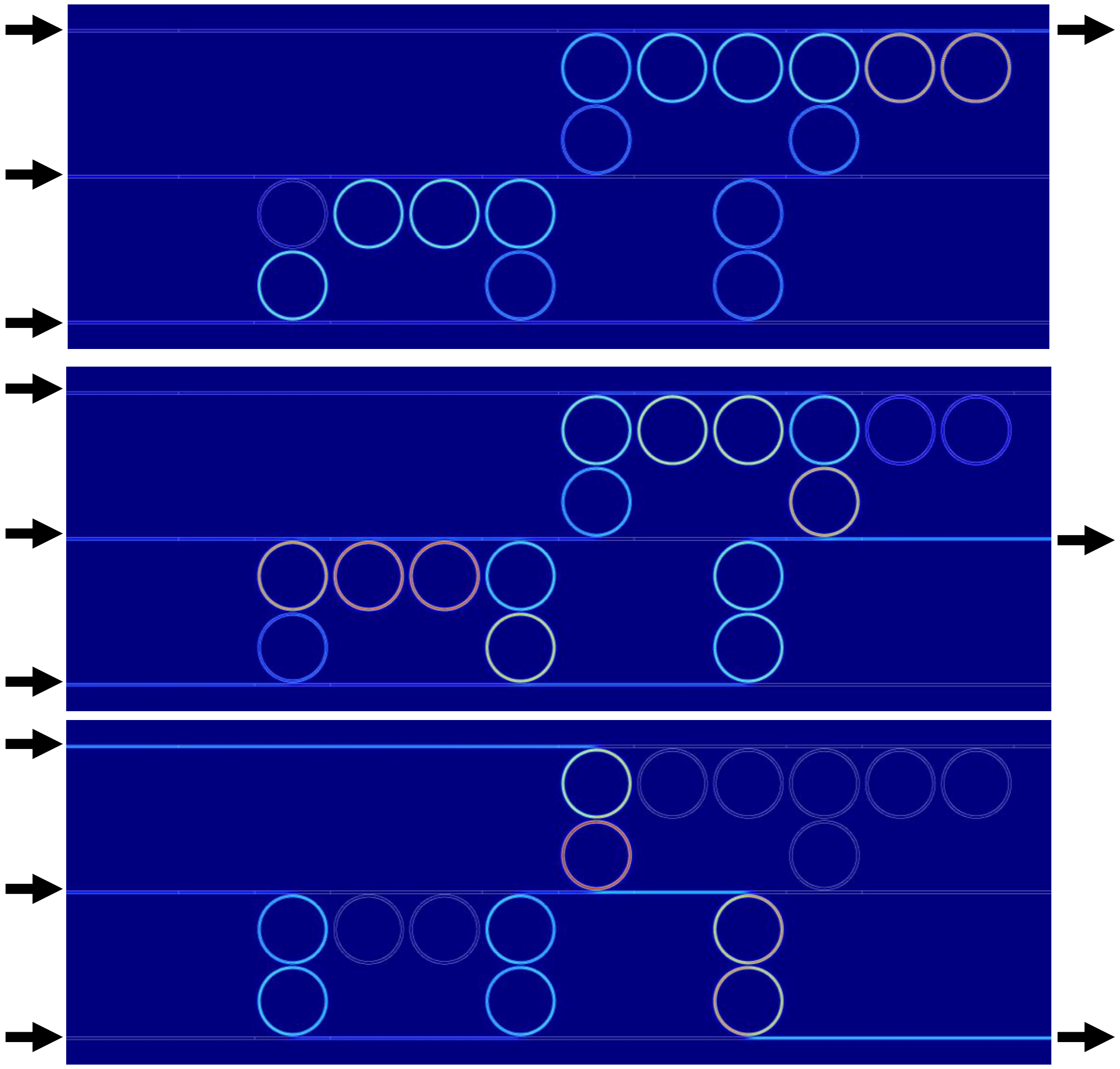

Figure 4. Example of 3×3 optical MIMO operation.
(Mixed three lightwaves input from the left side are output to one port of right side.)

4. Sumarry

The optical MIMO processing based on the universal linear optical circuit is explained. By cascading MZIs, PSs, and attenuators, arbitrary optical matrix multiplication is realized. The example of the use of the optical MIMO processor is also shown. I would consider that such an optical MIMO device may be a key of the manipulation of optical signals in the future.

References

[1] R. Ryf, S. Randel, A. H. Gnauck, C. Bolle, A. Sierra, S. Mumtaz, M. Esmaeelpour, E. C. Burrows, R. J. Essiambre, P. J. Winzer, D. W. Peckham, A. H. McCurdy, and R. Lingle, “Mode-division multiplexing over 96 km of few-mode fiber using coherent 6×6 MIMO processing,” *J. Lightw. Technol.*, vol. 30, no. 4, pp. 521–531, Feb. 2012.

[2] A. Ribeiro, A. Ruocco, L. Vanacker, and W. Bogaerts, “Demonstration of a 4×4-port universal linear circuit,” *Optica*, vol. 3, no. 12, pp. 1348–1357, Dec. 2016.

[3] R. Tang, T. Tanemura, and Y. Nakano, “Reconfigurable integrated MIMO optical mode demultiplexer using MMI couplers,” *IEEE Photonics Technol. Lett.*, vol. 29, no. 12, pp. 971–974, Jun. 2017.

[4] T. Sato and A. Enokihara, “Ultrasmall design of a universal linear circuit based on microring resonators,” *Opt. Express*, vol. 27, no. 23, pp. 33005–33010, Nov. 2019.

[5] W. Bogaerts, D. Pérez, J. Capmany, D. A. B. Miller, J. Poon, D. Englund, F. Morichetti, and A. Melloni, “Programmable photonic circuits,” *Nature*, vol. 586, no. 7828, pp. 207–216, Oct. 2020.

[6] M. Reck, A. Zeilinger, H. J. Bernstein, and P. Bertani, “Experimental realization of any discrete unitary operator,” *Phys. Rev. Lett.*, vol. 73, no. 1, pp. 58–61, Jul. 1994.

[7] W. R. Clements, P. C. Humphreys, B. J. Metcalf, W. S. Kolthammer, and I. A. Walsmley, “Optimal design for universal multiport interferometers,” *Optica*, vol. 3, no. 12, pp. 1460–1465, Dec. 2016.

[8] D. A. B. Miller, “Self-configuring universal linear optical component,” *Photonics Res.*, vol. 1, no. 1, pp. 1–15, Jun. 2013.

Binary Classification of Uplink-Channel States for Secure Body-Coupled Communication

Akinori BAN and Ai-ichiro SASAKI*
Dept. of Electronic Engineering and Computer Science, Kindai University, Higashi-Hiroshima, 739-2116 Japan
*Corresponding author: aisasaki@hiro.kindai.ac.jp

Abstract – Body-coupled communication (BCC) is a short-range wireless technology that can link communication devices with a human body. The BCC channel is formed by capacitive coupling among the body, devices, and earth. When another person approaches the BCC system, he is inevitably involved in the system because of the coupling. In this situation, eavesdropping and accidental data transmission can occur. A feasible approach to this security problem is detecting the existence of the undesirable person based on the information of received signals. We emphasize that fiber-optic EO-OE converters are indispensable for correctly evaluating the received signals in BCC uplink channels because they are affected by electronic apparatuses. It was demonstrated that the undesirable person can be detected with an accuracy of 96% by using machine learning.

Keywords – body-coupled communication; channel gain; classification; EO-OE converter; machine learning

1. Introduction

The idea of body-coupled communication (BCC) was proposed in 1996 for realizing smart communication among multiple wearable devices [1]. Its basic concept is that a human body can be utilized as data communication paths like cables. This novel idea can be applied also to communication between fixed and mobile devices [2]. Today, BCC technologies are being studied by many researchers because of their fascinating natures [3]–[6].

A weak point of BCC is that eavesdropping and accidental data transmission can easily occur. Recently, we proposed a method to address this security problem [7]. The basic concept of the method is that the existence of the undesirable person involved in eavesdropping or accidental data transmission can be detected by analyzing received signals. If the undesirable persons are correctly detected, the security problem can be avoided by system level measures. From a practical viewpoint, it is preferable to analyze signals received by fixed devices instead of mobile devices. In other words, the analysis should be performed for received signals in uplink channels.

By considering the above reason, we investigated the feasibility of detecting the undesirable person in BCC uplink channels. It is emphasized that photonic techniques play an important role in correct evaluation of received signals. Furthermore, machine learning effectively works for detecting the undesirable person.

2. Concepts & Models of BCC Channels

Figure 1 shows a conceptual image of a BCC uplink channel, which we call an “ordinary state.” Data signals generated by a mobile transmitter (M-TX) are applied between a pair of electrodes (M+ and M–). A human body can be regarded as a conductor covered by insulators, which are skin, clothes, and shoes. When M-TX is existing in the vicinity of the human body, conduction currents flow inside the body. A fixed receiver (F-RX) is connected to a pair of electrodes (F+ and F–). When person 1 equipped with M-TX rides on F+, received currents are induced inside F-RX and they flow within earth. Since M– and earth form a capacitor, the currents return to M– in the form of electric fields, which are called displacement currents. The BCC uplink channel under the ordinary state is expressed by a circuit model shown in Figure 2.

Figure 3 shows a conceptual image of the BCC uplink channel when the undesirable person (Person 2) is involved. Let’s call the situation an “extraordinary state.” Here Per-

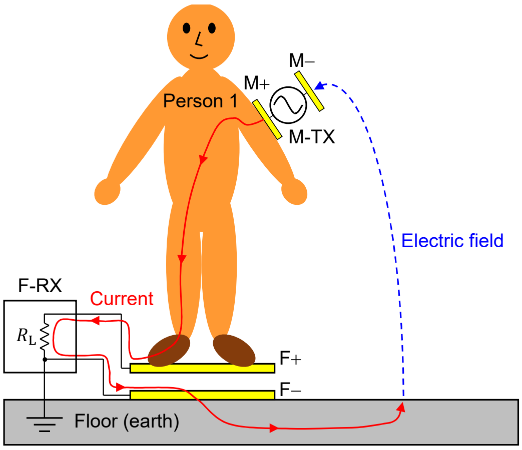

Figure 1. Conceptual image of a BCC uplink channel in an ordinary state.

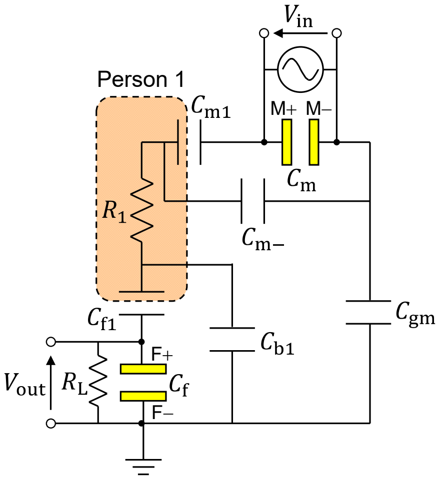

Figure 2. Equivalent circuit model of a BCC uplink channel in an ordinary state.

son 1 without M-TX stands on F+ and Person 2 equipped with M-TX exists in the vicinity of Person 1. Although Person 2 does not stand on F+, he can communicate with F-RX via Person 1. From a viewpoint of communication security, this is an undesirable situation because eavesdropping and accidental data transmission can occur. The BCC uplink channel under the extraordinary state can be represented by a circuit model shown in Figure 4.

Here we define channel gain $G(f)$ of the BCC channels as

$$G(f) \triangleq \left|\frac{V_{out}(f)}{V_{in}(f)}\right|. \quad (1)$$

Note that $G(f)$ is equivalent to $V_{out}(f)$ because $V_{in}(f)$ is known in advance. Furthermore, we denote channel gains under

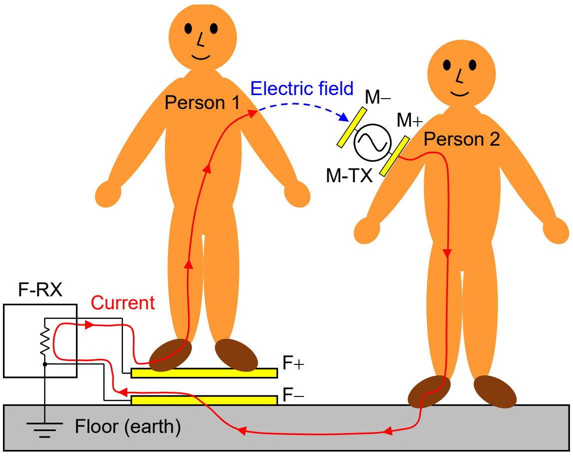

Figure 3. Conceptual image of a BCC uplink channel in an extraordinary state.

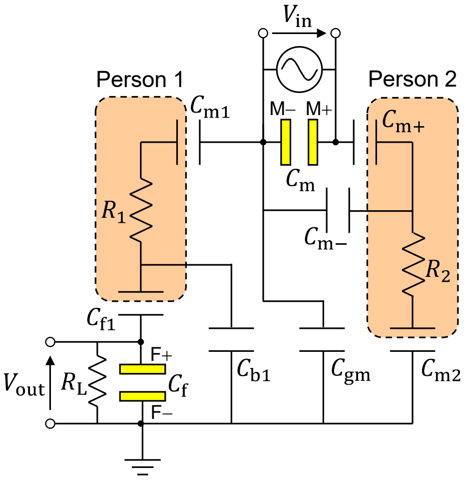

Figure 4. Equivalent circuit model of a BCC uplink channel in an extraordinary state.

ordinary and extraordinary states by $G_o(f)$ and $G_e(f)$, respectively. It is considered that the traces of the ordinary and extraordinary states are contained in $G_o(f)$ and $G_e(f)$, respectively. This suggests that we can predict the unknown state (ordinary/extraordinary) by analyzing $G(f)$ obtained by F-RX. This is a binary classification problem and nothing but detecting the undesirable person.

3. Setup for Channel Gain Masurements

To investigate the feasibility of the binary classification, $G(f)$ must be experimentally obtained under various conditions. Before the measurement of $G(f)$, we must pay attention to influences of electronic apparatuses on BCC channels. Figure 5 shows the setup for measuring $G(f)$ with purely electronic apparatuses. In this setup,

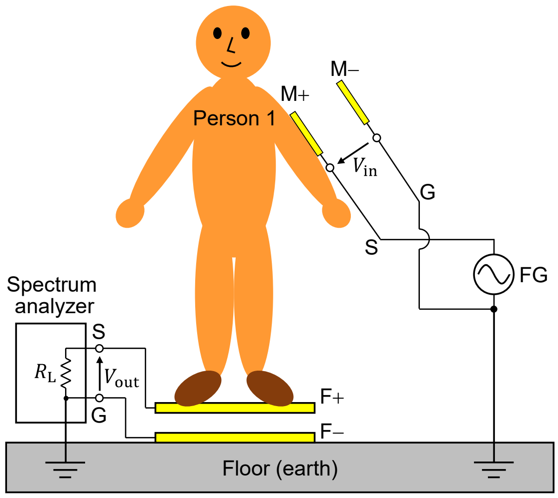

Figure 5. Setup for measuring BCC uplink channel gain by using purely electronic apparatuses.

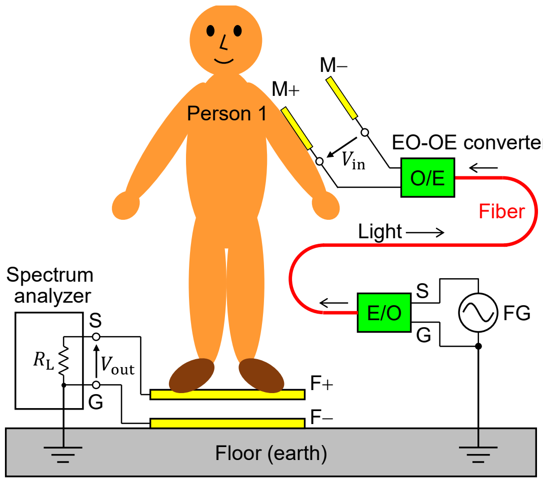

Figure 6. Setup for measuring BCC uplink channel gain by using an EO-OE converter.

M− is inevitably earthed because ground of a function generator (FG) is connected to M−. However, in real situations, M− is electrically isolated from earth because mobile devices are powered by batteries. Therefore, the setup shown in Figure 5 is invalid. Measurements must be done while keeping M− isolated from earth.

To correctly evaluate $G(f)$, photonic techniques are effective. In this case, an EO-OE converter is suitable for feeding input signals. The setup for measuring $G(f)$ with the EO-OE converter is shown in Figure 6. Electrical signals generated by FG are once transformed into optical signals by the EO converter (E/O). The optical signals are delivered to the OE converter (O/E) by an optical-fiber cable. The OE converter transforms the optical signals into electrical signals, which are applied between M+ and M−. Because of the isolation nature of the optical-fiber cable, M− is electrically isolated from GND of FG. Therefore, it becomes possible to correctly evaluate $G(f)$ while keeping M− isolated from earth owing to the EO-OE converter.

4. Classification of BCC Channel States

Figure 7 shows examples of measured $G(f)$. The black curves indicate $G_{\mathrm{o}}(f)$. Other colored curves show $G_{\mathrm{e}}(f)$ and d represents the distance between Person 1 and M-TX attached to Person 2. It is observed that $G_{\mathrm{o}}(f)$ is smooth and $G_{\mathrm{e}}(f)$ undulates wildly. It will be easy to correctly classify $G(f)$ into $G_{\mathrm{o}}(f)$ or $G_{\mathrm{e}}(f)$ as long as these general features are reflected in $G(f)$. Figure 8 shows $G(f)$ measured under various conditions. Although most of $G_{\mathrm{o}}(f)$ and $G_{\mathrm{e}}(f)$ exhibit the general features, some of them do not seem to possess the features. Therefore, it is not always easy to correctly classify $G(f)$ into $G_{\mathrm{o}}(f)$ or $G_{\mathrm{e}}(f)$.

It is well-known that machine learning is effective for solving classification problems. Therefore, we applied machine learning for predicting ordinary/extraordinary states based on measured $G(f)$. In this study, we used Mathematica 12 as a tool for machine learning. Various learning algorithms can be used with the tool. As shown in Figure 8, the numbers of measured G_{o} and G_{e} samples are 48 and 64, respectively. To effectively increase the numbers of samples, a 2-fold cross-validation was applied.

The prediction accuracies obtained with several machine-learning algorithms are summarized in Table 1. The results obtained in this study are listed in "Uplink" column. For reference, results reported in [7] is also shown in "Downlink" column. The maximum accuracy reached 96% with logistic regression and neural network. However, several other algorithms also exhibited the prediction accuracy of approximately 90%.

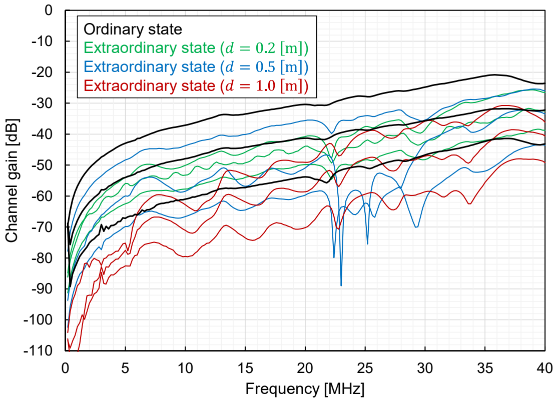

Figure 7. Examples of BCC uplink channel gain measured under ordinary and extraordinary states.

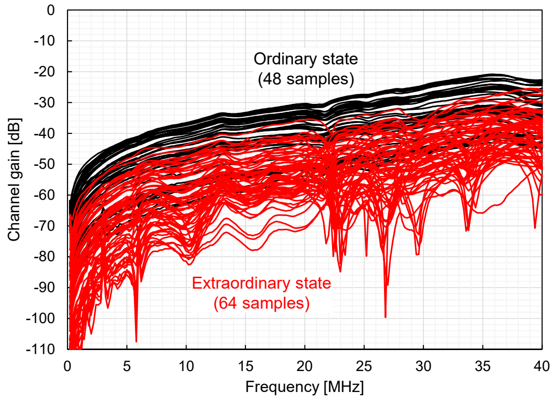

Figure 8. BCC uplink channel gain measured under various conditions.

Table 1. Prediction accuracy obtained by using machine learning.

Algorithm	**Prediction Accuracy**	
	Uplink (this study)	**Downlink** [7]
Logistic regression	96%	94%
Neural network	96%	89%
Support vector machine	82%	89%
Decision tree	91%	86%
Nearest neighbors	93%	84%

This fact indicates that the prediction accuracy does not depend significantly on learning algorithms. These results demonstrated the effectiveness of our proposed method for detecting the undesirable person.

5. Conclusion

We investigated a method for detecting the existence of an undesirable person involved in BCC uplink channels. The key idea of the method is detecting the undesirable person based on the information contained in signals received by fixed devices. This is equivalent to binary classification problems, i.e., classifying measured $G(f)$ into $G_\mathrm{o}(f)$ or $G_\mathrm{e}(f)$. It is emphasized that an EO-OE converter is indispensable for correctly evaluating $G(f)$ because mobile devices are not earthed but are kept floating in real situations. Photonic techniques are effective not only in measurements of microwave-frequency ranges but also in that of lower-frequency ranges. We applied machine learning for the binary classification and the prediction accuracy reached 96% in BCC-uplink channels. The experimental results support the validity of our proposed method in establishing secure BCC systems.

References

[1] T. G. Zimmerman, "Personal area networks: Near-field intrabody communication," IBM Syst. J., vol.35, nos.3/4, pp.609–617, 1996.

[2] Y. Kado et al., "Special feature: Trends and business prospects for human-area networking technology – Connecting people, objects, and networks," NTT Tech. Rev., vol.8, no.3, Mar. 2010. https://www.ntt-review.jp/archive/2010/201003.html

[3] D. Naranjo-Hernández, A. Callejón-Leblic, Ž. L. Vasic, M. Seyedi, Y.-M. Gao, "Past results, present trends, and future challenges in intrabody communication," Wireless Commun. Mobile Comput., vol.2018, Art. no.9026847 Mar. 2018.

[4] W. J. Thomlinson, S. Banou, C. Yu, M. Stojanovic, and K. R. Chowdhury, "Comprehensive survey of galvanic coupling and alternative intra-body communication technologies," IEEE Commun. Surveys Tuts., vol.21, no.2, pp.1045–1164, 2nd Quart., 2019.

[5] I. Culjak, Ž. L. Vasic, H. Mihaldinec, and H. Džapo, "Wireless body sensor communication systems based on UWB and IBC technologies: Stete-of-the-art and open challenges," Sensors, vol.20, no.12, Art. no.3587, Jun. 2020.

[6] M. Nath, S. Maity, S. Avlani, S. Weigand, and S. Sen, "Inter-body coupling in electro-static human body communication: theory and analysis of security and interference properties," Sci. Rep., vol.11, Art. no.4378, Feb. 2021.

[7] A Sasaki, K. Morita, and A. Ban, "Machine-learning approach for binary classification of signal transmission modes in human body communication channels," Proc. 2020 Int. Conf. Emerg. Technol. Commun. (ICETC 2020), B2-4, Dec. 2020.

Measurement of Reflected Microwave Guided-Mode Signal Propagating along FRPM Pipe-Wall Using Electro-Optic Sensor for Non-Destructive Remote Pipeline Inspection

Kosuke YOSHIDA[1] Sayaka MATSUKAWA[1,2] Satoru KUROKAWA[2]
Tadahiro OKUDA[1,3] Masaya HAZAMA[3] and Hiroshi MURATA[1]

[1]Graduate School of Engineering, Mie University 1577 Kurima-Machiya-Cho, Tsu-City, Mie 514-8507 Japan.
[2]AIST 1-1 Umezono, Tsukuba-City, Ibaraki 305-8568 Japan.
[3]Kurimoto Ltd. 1 Koyagi-Cho, Higashi-Ohmi-City, Shiga, 527-0108 Japan.

*Corresponding author: murata@elec.mie-u.ac.jp

Abstract – We have proposed and developed the non-destructive inspection method for buried fiberglass reinforced plastic mortar (FRPM) pipelines utilizing microwave guided-modes propagating along FRPM pipe walls. The key point of this method is to detect the microwave guided-mode signal reflected by a foreign object on the outer surface of the buried FRPM pipeline or a crack in the pipe wall, which enables us to have non-destructive inspection of underground pipelines remotely. In this paper, we report microwave time-domain analysis results of reflected microwave signals using an electro-optic (EO) sensor. Rather clear images of the reflected signals are obtained compared to the results using a standard dipole antenna.

Keywords – Non-destructive inspection; microwave guided-mode; FRPM pipeline, time-domain analysis; EO-sensor.

1. Introduction

Fiberglass reinforced plastic mortar (FRPM) is widely used for pipelines in a lot of infrastructures owing its excellent mechanical and chemical characteristics. For example, the total length of underground FRPM pipelines for agriculture water supply is ~50,000 kilometers in Japan. However, at present, there is no practiced method for non-destructive inspection of buried FRPM pipelines under-ground. Therefore, there is a demand for a method to perform inspection and diagnosis of buried FRPM pipelines nondestructively and remotely.

Possible candidates of a non-destructive inspection method for FRPM pipelines may be to use MRI, X-rays, and ultrasound [1]-[3]. However, inspections using MRI or X-rays are not suitable for under-ground pipelines because of the large and rigorous equipment required. In addition, in the case of ultrasonic waves, the energy of the ultrasonic waves is stored in the inner space of a pipeline filled with air or water. Therefore, it is not easy to obtain detailed information of the inside of the pipe wall and the outer surface the pipeline with a high signal-to-noise (S/N) ratio.

Recently, we found an interesting phenomena in a standard FRPM pipe, that is, microwaves of 1 ~ 9 GHz are well-confined in the FRPM pipe-wall with a thickness of ~20 mm and are propagating along the FRPM pipe walls with a rather low propagation loss. Utilizing these interesting characteristics, we have proposed the non-destructive inspection method for FRPM pipelines [4]-[5]. The key point of this method is to detect the microwave signals reflected by a foreign object or a crack in the pipeline. By utilizing the photonics-based microwave measurement techniques such as an electro-optic (EO) sensor and an optical fiber link, it is possible to inspect FRPM pipelines non-destructively and remotely.

In this paper, we report a time-domain analysis of a reflected microwave guided-mode signal by use of an EO sensor. By using an EO sensor for the measurement of the reflected microwave signals, clear images to measure the conditions of FRPM pipelines.

2. Experiment

Figure 1 shows the experimental set-up. A FRPM pipe with a length of 1,000 mm, an inner diameter of 250 mm, and a thickness of 18 mm was used for the experiment. The effective dielectric constant value of the FRPM used in the experiment was about 4.6.

A simple dipole antenna was attached on the end of the FRPM pipe along the pipe-wall to input and to supply microwave signals propagating as TE guided-modes. The microwave signal was supplied from a vector network analyzer (VNA) via a standard microwave amplifier. In the preliminary experiment, we confirmed that a microwave is rather tightly confined to the inside of the FRPM region (waveguide core) and that a microwave guided-mode signal propagating along the FRPM core is reflected at the other end of the pipe. In addition, if a foreign object is attached on the surface of the FRPM pipe-wall, a microwave signal is also reflected by the object. Therefore, by measuring the reflected signals precisely, remote and non-destructive inspection of the FRPM pipe is expected.

In the experiment, the frequency of the microwave signal from the VNA was swept from 1 to 9 GHz and the reflected signal was measured by use of a commercially available EO sensor, SH-10 from SEIKOH GIKEN, Co. Ltd. To obtain the temporal echo signal, the measured signals were analyzed using the Fourier transformation.

Typical examples of the measured time domain signals are shown in Figs. 2 (a) and (b). The vertical axes are corresponding to the position of the EO sensor along the circumstantial direction in the measurement. We can see that clear reflected (echo) signals are observed at the time of ~13 ns in Figs. 2 (a) and (b), which are due to the reflection from the other end of the FRPM pipe. On the contrary, another clear echo signal is observed only in Fig. 2 (b), with a foreign object (concrete block) on the surface of the pipe-wall at the middle of the pipe as shown in Fig. 1. These time values of the measured echo signals were in good agreement with the calculated delay time values taking into account of the length of the pipe, the position of the attached object, and the group velocity of the microwave guided-modes measured in the preliminary experiment [4], [5].

Compared with the time domain signals using a standard dipole antenna to measure the microwave reflected signals [5], the time resolution and S/N ratio were rather improved in the measurement with the EO sensor, which may be due to the excellent characteristics of the EO sensor for the microwave field measurement with low-immunity and low distortion, we believe.

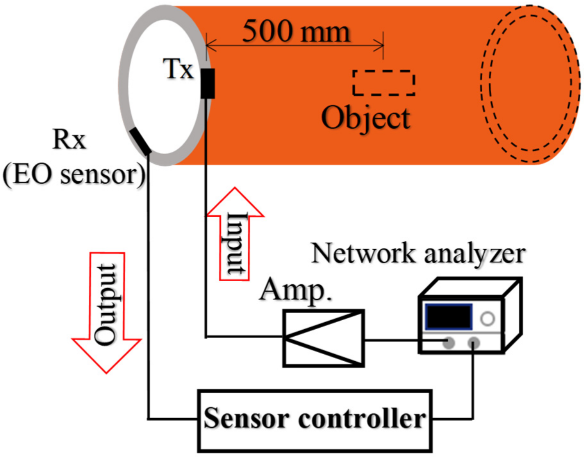

Figure 1. Experimental set-up for the reflected microwave guide-mode signal using an EO sensor.

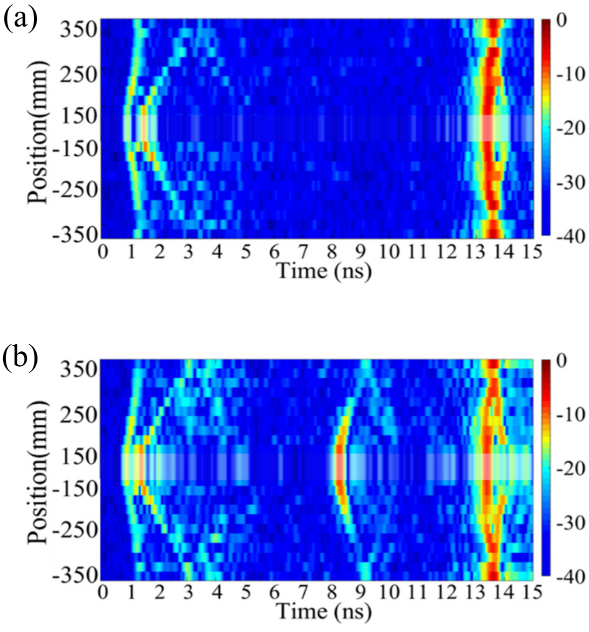

Figure 2. Time domain responses of the reflected signals measured by use of the EO sensor.
(a) No object. (b) With an object (concrete block) at the center of the FRPM pipe.

3. Conclusion

By using the EO sensor, rather clear images of the time domain echo signals were obtained with a good time resolution (~0.5 ns) and high S/N ratio (>30 dB), which are useful for the remote inspection of FRPM pipelines. By combining a radio-over-fiber (RoF) link to supply microwave signals to the input dipole antenna from the microwave signal source, a pipeline remote measurement system can be obtained. This system is suitable for remote inspection and diagnosis of FRPM pipelines under-ground by using a RoF link with an optical fiber cable over 1 km owing to the extremely small propagation loss of a silica fiber.

Now we are trying to prepare this remote inspection experiment of FRPM pipes using a RoF link.

References

[1] E. Marfisi, C. J. Burgoyne, M. H. G. Amin, and L. D. Hall, "Use of the MRI technique to study concrete and FRP reinforced concrete behavior," Resuarch Leading to the Development of Design Guideline for the Use of FRP in Concrete Structure -2nd Con Fiber Crete Youn Researcher Conference, June 2002, Corfu, Greece.

[2] Y. Yokono, S. Matsubara, S. Matsui, M. Kitajima, H. Yabushita, S. Utoyama and N. Wakita, "Air-coupled Ultrasonic Inspection Technique for FRP Structure," Asia-Pacific Conference on NDT, 2006.

[3] M. J. S. Lowe, D. N. Alleyne, P. Cawley, "Defect detection in pipes using guided wave," Ultrasonics, Vol. 36, Issues 1-5, pp. 147-154, Feb. 1998.

[4] S. Matsukawa, K. Yoshida, T. Okuda, M. Hazama, S. Kurokawa, and H. Murata, "Non-destructive inspection method for FRPM pipelines utilising time-domain responses of microwave guided-modes," Electronics Letters, vol. 56, no. 19, pp. 982-985, Sep. 2020.

[5] K. Yoshida, S. Matsukawa, S. Kurokawa, T. Okuda, M. Hazama, and H. Murata, "Microwave Time-Domain Analysis for Non-Destructive Inspection of FRPM Pipelines Using Electro-Optic Sensor," MWP 2020, P.36, Nov. 2020, Matsue, Shimane, Japan.

[Invited Talk] Microwave Photonic Signal Processing Towards Remote RF Spectrum Sensing

Chao Wang[1*], Chaitanya K. Mididoddi[1,2], and Yuanli Yue[1]
[1]School of Engineering, University of Kent, CT2 7NT Canterbury, United Kingdom
[2]Department of Physics and Astronomy, University of Exeter, EX4 4PY Exeter, United Kingdom
*Corresponding author: c.wang@kent.ac.uk

Abstract –RF sensing and surveillance systems and networks have become increasingly more complex and expensive, especially in scenarios where many large-bandwidth RF signals need to be handled. Thanks to the unique advantages of photonics techniques, microwave photonics provides a promising solution to enhance the overall performance of remote RF spectrum sensing networks. In this paper, recent advancements of photonic-assisted microwave spectrum sensing are reviewed, with particular focus on microwave photonic channelization, real-time Fourier transform, compressive sensing, and weak signal detection.

Keywords – microwave photonics, RF spectrum sensing, photonic signal processing, compressive sensing

1. Introduction

Microwave photonics provides a promising solution for the processing of high-frequency and broadband microwave signals [1], as it overcomes the bottleneck due to the limited sampling speed of digital electronics. Other advantages of processing microwave signals in the optical domain include large tunability and immunity to electromagnetic interference (EMI). Concepts and systems to achieve microwave photonic signal processing have been actively applied in remote RF spectrum sensing.

Benefits of using optical fibres for transporting remote RF sensor signals include low loss and low distortion propagation in optical fibres, reduced cabling size and weight, physically isolated signal in different optical channels, extremely broad bandwidth to support a wide range of RF spectrum, and design flexibility in optical signal processing systems. In addition to the normal role of transporting RF signals through long distance, the optical fiber link can also provide signal processing functions that reduce the challenging requirements to both analog electronics and digital signal processors at centralized backend receivers. In this paper, recent development of applying various microwave photonics signal processing approaches in remote RF spectrum sensing are reviewed.

2. Photonic RF spectrum sensing based on channelisation

One of the most promising microwave photonic solutions for RF spectrum sensing is the photonic channelisation approach as it enables simultaneous sensing of multiple-frequency or broadband RF sensor signals. To form the equivalent detection channels in the RF frequency bands of interest, an optical wavelength scanning scheme or a dual optical frequency comb approach is normally implemented. These photonics assisted approaches are based on direct RF frequency domain channelisation. Alternatively, optical channelisation can also be used to equivalently sample the broadband RF signal in the time domain [2]. This is made possible in a dispersion-induced photonic time-stretch system, where the optical carrier is a stretched ultrashort optical pulse such that its temporal waveform mirrors its spectrum shape. If the temporal waveform is carrying the unknown RF signals, the pulse spectrum will hold the same shape as the temporal RF signals. Therefore, an optical channeliser, such as a DWDM, not only splices the optical spectrum, but also equivalently samples the temporal RF signal. The benefits of this approach include stable sampling (totally passive), and better frequency measurement resolution than the actual channel space, and real-time operation.

3. Photonic RF spectrum sensing based on real-time Fourier transform

RF spectrum sensing can be done via Fourier transform analysis. However, direct sampling and digital Fourier analysis of broadband RF sensor signals suffer from challenges of bandwidth limitation of front-end analogue and sampling electronics. On the other hand, microwave photonic provides a promising solution to these challenges via real-time Fourier transform [3]. Also known as balanced temporal pulse shaping, this approach incorporates two dispersive elements having exactly opposite dispersion values. Photonic time-stretched optical pulses by the first dispersive element is modulated by the incoming RF signal, which will also modulate the pulse spectrum due to one-to-one mapping between wavelength and time. The second dispersive element with the opposite dispersion completely compresses the stretched and modulated optical pulse. The resultant optical pulse will have a temporal shape that is Fourier transform of the incident RF signal. In this way, no computation heavy digital FFT is needed and the RF spectrum of the incident signal can be obtained in the optical domain in real-time.

4. Photonic compressive sensing for RF spectrum sensing

Compressive sensing (CS) has been recently proved as a promising data compression method in imaging and signal processing. The CS approach is based on the proposition that natural images/signals have a sparse representation in a transformation domain and can be reconstructed from down-sampled data. It is a promising solution for detection of large-bandwidth and high-frequency RF signals as it will reduce the detection bandwidth requirement.

The concept of CS has been implemented using photonic hardware for real-time operation. A most straightforward photonic CS method is time-domain implementation approach [4], where random mixing is achieved by modulating the optical carrier signal with a Pseudo-Random Bit Sequence (PRBS) generated at the Nyquist rate. The main challenge associated with this approach is that high-speed electronics, such as a PRBS generator and a temporal mixer (modulator) with a speed matched to the uncompressed Nyquist rate are always required.

Another photonic CS method we recently demonstrated is based on spectral domain solution using a special optical spectral filter having random spectral response [5]. Compared to the time-domain CS method, spectral domain method does not require high-speed PRBS generator and modulator and eliminates the challenging high-frequency sample-and-hold integration devices. More importantly, the random mixing is completely implemented in the optical domain through passive filtering, the equivalent Nyquist sampling rate could be extremely high.

5. Weak RF signal detection via optoelecronic oscillator

One challenge in RF spectrum measurement is detection of low-power RF signal from noisy environment. Normal RF amplifiers, even the low-noise amplifiers, fall short in this particular scenario as they also amplify the noise and usually make the noise performance even worse. One promising solution to this challenge is selective amplification via a frequency scanning Optoelectronic Oscillator (OEO) [6]. The oscillating frequency of an OEO is determined by the narrowband RF band-pass filter inside the OEO cavity. By implementing a tunable microwave photonic filter, a frequency scanning OEO can be achieved. The input RF signal is fed into the OEO cavity via an antenna and a modulator. Only if the frequency of the weak input RF signal under detection matches with the oscillation frequency of the OEO, it is selectively detected and amplified due to strong oscillation.

6. Conclusion

Microwave photonic signal processing has become a promising solution for challenges in broadband RF spectrum sensing and surveillance thanks to the unique advances brought by optics such as broad bandwidth, better flexibility, and inherent immunity to EMI. In this paper, several microwave photonic approaches for photonic assisted RF spectrum sensing have been briefly introduced. As a step further, photonic RF spectrum sensing can be employed for cognitive radio applications, where microwave photonic cannot only perform broadband real-time RF spectrum sensing, but also frequency-agile broadband RF waveform generation. This concept provides an effective solution to overcome the limitations of current systems in terms of frequency of operation, bandwidth and processing speed for future intelligent RF systems.

References

[1] J. P. Yao, "Microwave Photonics," J. Lightwave Technol., vol. 27, no. 1-4, pp. 314-335, Feb 2009.

[2] C. Wang and J. Yao, “Ultrahigh-Resolution Photonic-Assisted Microwave Frequency Identification Based on Temporal Channelization,” IEEE Transactions on Microwave Theory and Techniques, vol. 61, no. 12, pp. 4275-4282, 2013.

[3] C. Wang, M. Li and J. Yao, “Continuously Tunable Photonic Microwave Frequency Multiplication by Use of an Unbalanced Temporal Pulse Shaping System,” IEEE Photonics Technology Letters, vol. 22, no. 17, pp. 1285-1287, 2010.

[4] C. K. Mididoddi, F. Bai, G. Wang, J. Liu, S. Gibson, and C. Wang, "High-throughput photonic time-stretch optical coherence tomography with data compression," IEEE Photonics J, vol. 9, no. 4, pp. 1-15, 2017.

[5] C. K. Mididoddi, E. J. Ahmed, and C. Wang, "All-optical random sequence generation for compressive sensing detection of RF signals," in 2017 International Topical Meeting on Microwave Photonics (MWP), 2017, pp. 1-4.

[6] Y. Shao, X. Han, Q. Ye, B. Zhu, Y. Dai, C. Wang, and M. Zhao, "Low-Power RF Signal Detection Using a High-Gain Tunable OEO Based on Equivalent Phase Modulation," J. Lightwave Technol., vol. 37, no. 21, pp. 5370-5379, 2019.

Millimeter-Wave D-band Antenna-Coupled Electrode Electro-Optic Modulator

Shotaro Kodama*, Takuto Mori, Yui Otagaki, Hiroshi Murata
Graduate School of Engineering, Mie University, 1577 Kurima-Machiya-Cho Tsu-City 514-8507 Japan
*Corresponding author: 420M223@m.mie-u.ac.jp

Abstract –A new antenna-coupled electrode EO modulator for direct conversion of D-band wireless signals to optical signals is analyzed and designed. In this EO modulator, the modulation efficiency in the D-band is increased by using a thin $LiNbO_3$ film and fluorine based resin substrate. In the simulation, modulation electric field of about 2500 times larger than received D-band signal at the antenna was observed at the metal surface of the resonant electrode, which enable to have effective signal conversions from D-band wireless to optical signals.

Keywords –$LiNbO_3$, EO modulator, D-band, antenna, radio-over-fiber

1. Introduction

In recent years, the 5th generation (5G) wireless communication system using millimeter wave has been launched in many countries. Since millimeter-wave has high propagation loss in free space and cables, radio over fiber (RoF) technology is useful to convert millimeter-wave radio signals into optical signals for propagation. In the future, the wireless frequency will move to the higher and reach to the THz band.

We have developed a passive antenna-coupled electrode EO modulator that can directly convert wireless signals into optical signals without external power supply.[1,2] In this paper, we report on the analysis of an antenna-coupled electrode EO modulator operating in the D-band (120 GHz).

2. EO Modulator

Fig. 1 shows the configuration of the 120 GHz band antenna-coupled electrode EO modulator. A pair of patch antennas and a standing-wave resonant modulation electrode are coupled by a microstrip line to form the antenna-coupled electrode. The antenna-coupled electrode is sandwiched between a $LiNbO_3$ crystal substrate (t_{LN} = 10 μm) and a low dielectric constant Fluorine-based resin (t_F = 30 μm) substrate in the device configuration. The optical waveguide is formed along the resonant electrode on the backside of the $LiNbO_3$ crystal film. On the surface of a standing-wave resonant electrode, a strong electric field is induced that is several thousand times stronger than the millimeter-wave electric field received by the antenna. By using this strong electric field to successively modulate optical waves propagating in the optical waveguide, millimeter-wave radio signals can be converted into optical signals.

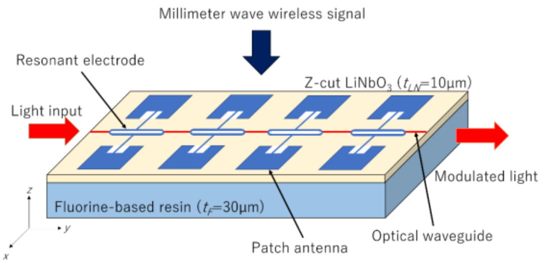

Fig. 1. 120 GHz band antenna-coupled electrode EO modulator.

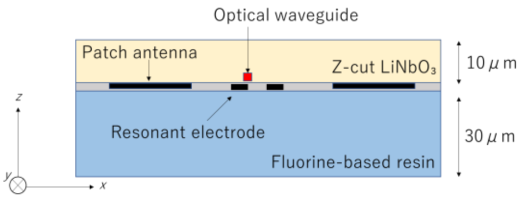

Fig. 2. Cross sectional view of the 120 GHz band antenna-coupled electrode EO modulator.

3. Analysis

The Analysis and design of the D-band antenna-coupled electrode EO modulator were carried out using the electromagnetic field simulator, HFSS.

The resonant electrode analysis model and electric field distribution are shown in Fig.3, and the analysis results of the resonant electrode are shown in Figs. 3-5. Fig. 4 shows the S_{11} parameter of the resonant electrode and Fig. 5 shows the Smith chart of the resonant electrode.

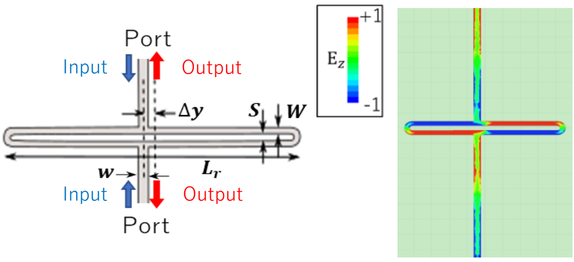

Fig. 3. The resonant electrode analysis model and calculated surface electric field distribution.

Table 1. Analysis parameters for resonant electrode

Resonant electrode length L_r	819μm
Resonant electrode width W	30μm
Resonant electrode gap S	30μm
Microstrip line feeding position Δy	43μm
Microstrip line width w	40μm

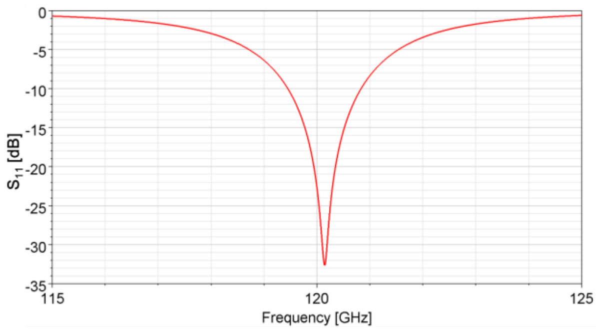

Fig. 4. S_{11} parameter of the resonant electrode.

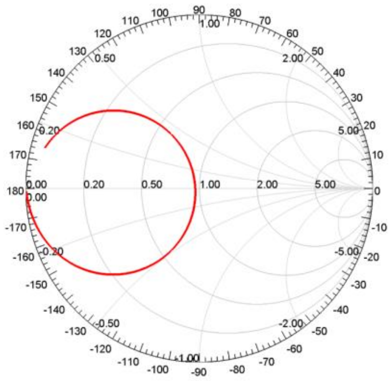

Fig. 5. Smith chart of the resonant electrode.

From Figs. 4 and 5, we can see that the good resonance and impedance matching were confirmed at around 120 GHz. The obtained design parameters of the resonant electrode is summarized in Table 1.

Next, the patch antenna analysis model and electric field distribution are shown in Fig. 6 and the analysis results of the patch antenna are shown in Fig. 6-8. Fig. 7 shows the S_{11} parameter of the patch antenna and Fig. 8 shows the Smith chart of the patch antenna.

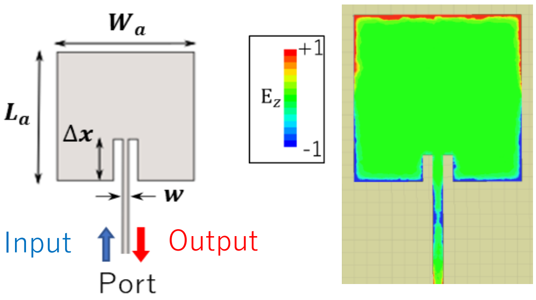

Fig. 6. The patch antenna analysis model and calculated electric field distribution.

Table 2. Analysis parameters for patch antenna

Patch antenna length L_a	668μm
Patch antenna width W_a	668μm
Microstrip line feeding position Δx	107μm
Microstrip line width w	40μm

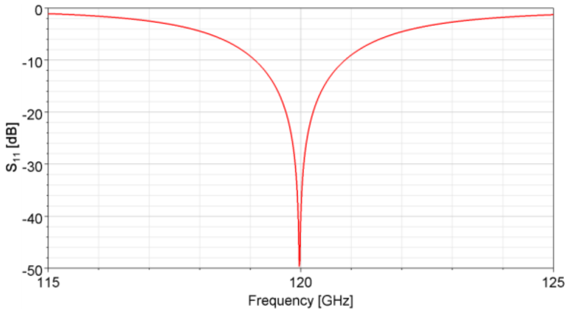

Fig. 7. S_{11} parameter of the patch antenna.

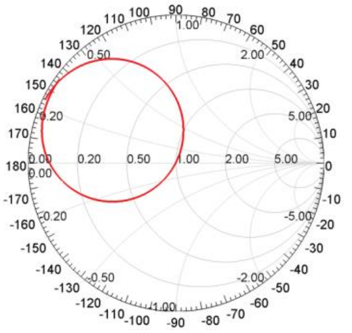

Fig. 8. Smith chart of the patch antenna.

From Figs. 7 and 8, we can see that the good resonance and impedance matching were confirmed at 120 GHz. The obtained design parameters of the antenna are summarized in Table 2.

Finally, the antenna-coupled electrode analysis model was formed by connecting the designed resonant electrode and two patch antennas through microstrip lines. Then the HFSS analysis was carried out by irradiating a D-band plane-wave signal to the antenna-coupled electrode normally. The antenna-coupled electrode model and electric field distribution are shown in Fig. 9 and, the analysis results of the antenna-coupled electrode are shown in Figs. 9-11.

Fig.10 shows the calculated field distribution along the resonant electrode electric field at the frequency of f = 120 GHz. In Fig. 10, A modulated electric field of about 2500 times of the wireless signal received at the antenna part was observed at the metal surface of the resonant electrode. With this strong electric field, it is possible to modulate the input light around 120 GHz effectively by using array of the antenna-coupled electrodes as shown in Fig. 1. The parameters of the designed antenna-coupled electrode are summarized in Table 3.

Now we are trying to prepare the fabrication of the designed D-band EO modulator.

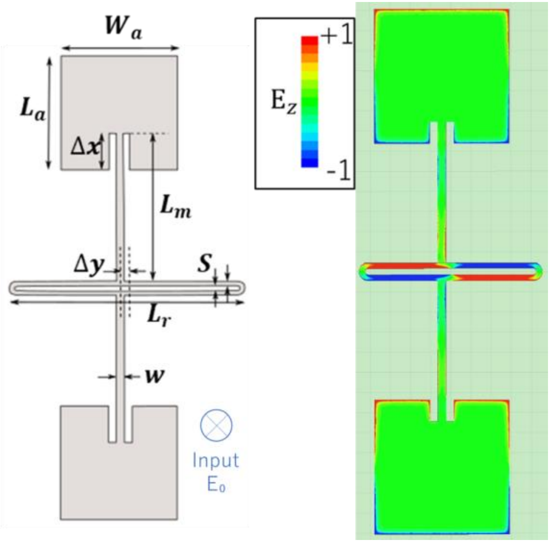

Fig. 9. Calculated field distribution on the surface of the designed antenna-coupled electrode (f = 120 GHz).

Table 3. Analysis parameters for antenna-coupled electrode

Patch antenna length L_a	668μm
Patch antenna width W_a	668μm
Microstrip line feeding position Δx	107μm
Resonant electrode length L_r	819μm
Resonant electrode width W	30μm
Resonant electrode gap S	30μm
Microstrip line feeding position Δy	43μm
Microstrip line width w	40μm
Microstrip line length L_m	700μm

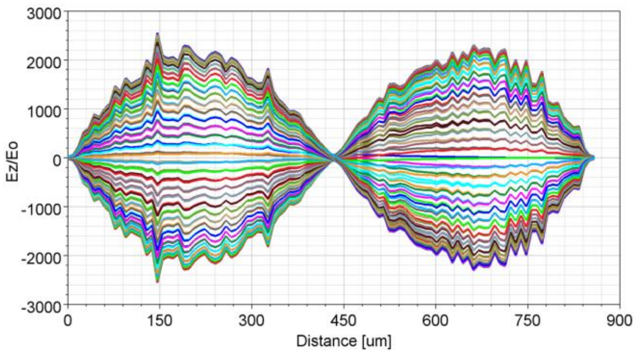

Fig.10 Calculated field distribution along the resonant electrode electric field (*f* = 120 GHz)

References

[1] H. Murata, “Millimeter-wave-band electro-optic modulators using antenna-coupled electrodes for microwave photonic applications,” J. Lightwave Technol.. vol. 38, pp. 5485-5491, 2020.

[2] H. Murata, S. Kodama, and H. Yokohashi, “W-band antennacoupled-electrode electro-optic modulator for millimeter-wave radar systems,” MWP 2020, Th1.4, Nov. 2020, Matsue, Japan.

28 GHz-Band Antenna-Coupled-Electrode Electro-Optic Modulator for Converting Two Orthogonal-Polarization Field Components Simultaneously for 5G Mobile Systems

Yui Otagaki[1,2*], Shunsuke Nakamori[2], Hiroto Yokohashi[1], Sayaka Matsukawa[1,3],
Satoru Kurokawa[3], Masahiro Sato[4], Masatoshi Onizawa[4], and Hiroshi Murata[1,2]
[1]Graduate School of Engineering, Mie University, 1577 Kurimamachiya-Cho, Tsu-City, Mie, 514-8507 Japan
[2]Faculty of Engineering, Mie University, 1577 Kurimamachiya-Cho, Tsu-City, Mie, 514-8507 Japan
[3]AIST, 1-1-1 Umezono, Tsukuba, Ibaraki, 305-8563 Japan
[4]SEIKOH GIKEN Co. Ltd., 296-1 Matsuhidai, Matsudo, Chiba, 270-2214 Japan
*otagaki@elec.mie-u.ac.jp

Abstract –Antenna-coupled-electrode electro-optic modulator has been developed to simultaneously receive and convert orthogonal polarization wireless signals into different optical signals, which can be used for 5G mobile communication systems and antenna measurements. The electro-optic modulator is designed to modulate the light waves propagating in the optical waveguides corresponding to the orthogonal polarization of the irradiated wireless signals, so that the wireless signals of different polarizations are simultaneously received, converted into optical signals, and separated at the output. Using the prototype electro-optic modulator, we have succeeded in simultaneously receiving and converting orthogonal polarization 28 GHz wireless signals into optical signals and have also measured the electrical conversion characteristics.

Keywords –Optical modulator; $LiNbO_3$; Radio-over-fiber system; EO sensor; Antenna measurement

1. Introduction

In recent years, the demand for high-speed wireless data transfer has been increasing in mobile communication services, and 5th generation (5G)/ Beyond-5G mobile communication systems using quasi-millimeter and millimeter-wave have been introduced and studied. Although quasi-millimeter and millimeter-wave signals have large propagation loss in free space and cables, the loss can be significantly reduced by radio-over-fiber technology, which uses optical fiber cables with an energy loss of 0.2 dB/km for standard single-mode silica cables [1]. Therefore, the technology to convert and control them freely through optical fiber networks is considered to be effective [2]. Wireless-optical fusion technology is also important for the precise measurement of antennas in the quasi-millimeter and millimeter-wave bands [3].

We have been developing antenna-coupled-electrode electro-optic (EO) modulators that directly convert wireless signals into optical signals without power supply and are effective for precise antenna measurements [1, 4, 5]. In addition, the new design of the antenna-coupled-electrode EO modulator that can receive two orthogonal polarization field components simultaneously is being developed [6]. The results of the measurements of simultaneous reception and electrical conversion characteristics of the two orthogonal polarization field components are reported in this paper.

2. Basic structure of the antenna-coupled-electrode EO modulator for receiving two orthogonal polarization field components simultaneously

The basic structure of the EO modulator is shown in Figure 1. The EO modulator is composed of an electro-optic crystal substrate of $LiNbO_3$ and a base low-dielectric constant substrate of SiO_2 glass bonded together [4]. The antenna-coupled-electrode consists of four microstrip square patch antennas and four standing wave resonant electrodes connected by eight feed lines, which is symmetrical to the center. In addition, two optical waveguides are arranged orthogonally along with the two sets of resonant electrodes.

The basic operation of the device is as follows. When a millimeter-wave wireless signal is irradiated to the device, each antenna receives the signal. The incident waves enter the electrode from two directions and their phases become opposite to each other (out-of-phase) at the resonance frequency. The odd mode is induced at the resonant electrodes, where the electric field concentrates to a small region just near the resonant electrodes. The light wave propagating above the resonant electrodes is modulated by the Pockels effect of $LiNbO_3$. In the proposed device, the feedline and the resonant electrode to be fed are automatically selected according to the polarization of the wireless signal, and the light waves in the optical waveguides corresponding to the X and Y polarization are modulated. Therefore, it is possible to simultaneously receive wireless signals of two orthogonal polarizations, convert them into different optical signals, and output them separately.

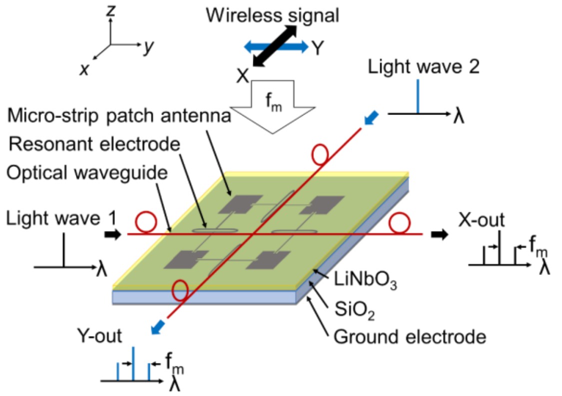

Figure 1. Basic structure of the proposed EO modulator.

3. Experiments

The experimental set-up shown in Figure 2 was used to measure the wireless signal conversion characteristics. C-band laser beams were input to the EO modulator, and a 28 GHz-band signal from port 1 of the vector network analyzer (VNA) was irradiated using a horn antenna from above the EO modulator (~10 dBm). The output light was measured using an optical spectrum analyzer. The output light from the EO modulator was the phase-modulated light, which was converted into amplitude-modulated light by passing it through a single-mode silica optical fiber (SMF) using the wavelength dispersion of the optical fiber. The amplitude-modulated light was then re-converted into an electrical signal by the high-speed photodiode (PD). While sweeping the signal from port 1 of the VNA, the output signal of the PD was connected to port 2 of the VNA and the frequency characteristics (amplitude and phase) of S_{21} was observed. Furthermore, the S_{21} signals for the different polarizations of the wireless signals irradiated to the EO modulator were obtained by switching the input signal to the PD using the optical switch.

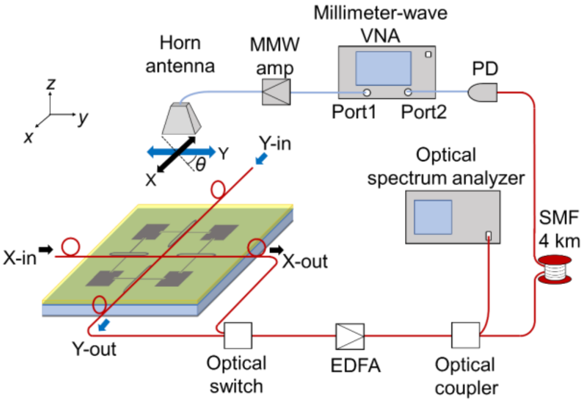

Figure 2. Experimental set-up for the measurement of signal conversion characteristics.

Examples of the results are shown in Figure 3. Clear characteristic of polarization separation was observed. When the polarization of the wireless signal was 45-degrees as in Figure 3(b), the X and Y output components were almost at the same level of amplitude. The results of the polarization dependence are shown in Figure 4. 0° and 180° correspond to Y polarization, and 90° corresponds to X polarization. Polarization dependence was observed as expected.

4. Conclusions

Using our developed EO modulator, we have demonstrated that the EO modulator can simultaneously receive and convert two orthogonal polarization wireless signals into optical signals. After re-conversion to the electrical signals, the frequency characteristics and the polarization dependence were measured. The EO modulator is expected to be used for data transmission and the precise sensor for antenna measurements in the 28 GHz-band. We are now developing a modulator with a further improved characteristic of polarization separation.

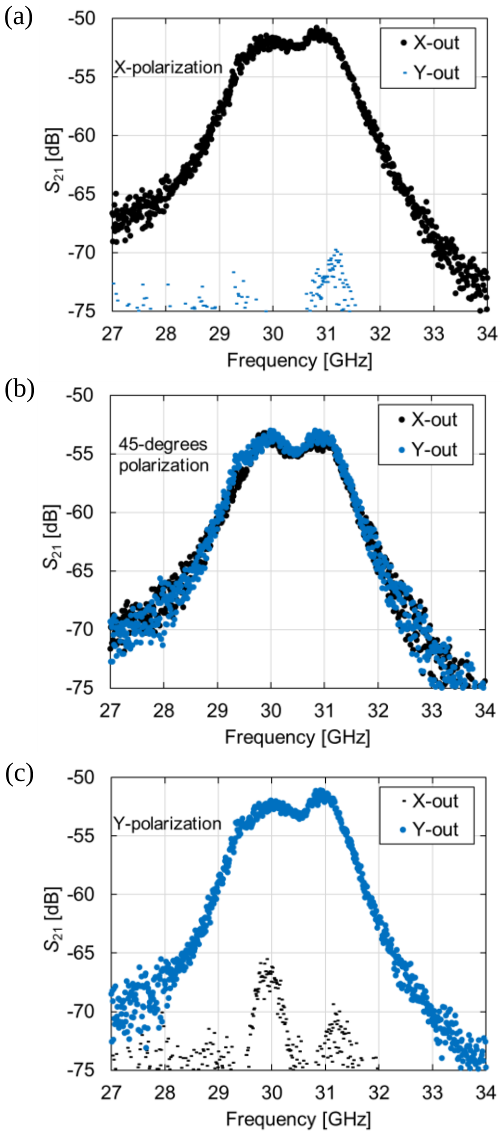

Figure 3. Measured frequency response of the re-converted electrical signals corresponding to the irradiated wireless signals (a) X-polarization, (b) 45-degrees polarization, and (c) Y-polarization.

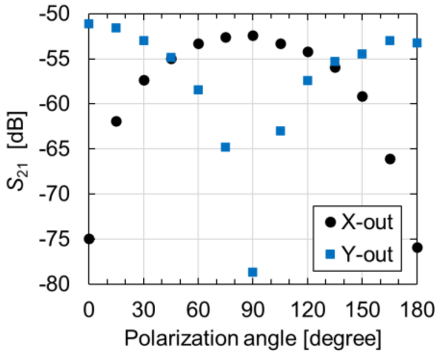

Figure 4. Polarization dependence of the re-converted electrical signal

References

[1] Murata H, Miyanaka R., Okamura Y. Wireless space-division-multiplexed signal discrimination device using electro-optic modulator with antenna-coupled electrodes and polarization-reversed structures. Int. J. Microw. Wirel. Technol. 2012; 4(3): 399-405.

[2] Capmany J, Novak D. Microwave photonics combines two worlds. Nature photonics. 2007; 1: 319-330.

[3] Kurokawa S, Hirose M, Ameya M. Precision antenna measurement using optical fiber link technologies. 2015 IEEE CAMA. November 20 - December 2, 2015, Chiang Mai, Thailand, pp. 1-4.

[4] Murata H, Yokohashi H, Matsukawa S, Otagaki Y, Shiomi H, Sato M, Toba Y, Kurokawa S. Antenna-coupled electrode electro-optic modulator and 28 GHz-band wireless signal transfer over fiber for 5G mobile systems. OECC/PSC 2019. July 7-11, 2019, Fukuoka, Japan, WF1-5.

[5] Inoue T, Ikeda T, Murata H, Okamura Y. Wireless data transfer in 60 GHz-band using array-antenna-electrode electro-optic modulator. 2016 IEEE Photonics Conf. October 2-6, 2016, Waikoloa, U.S., pp. 21-22.

[6] Yokohashi H, Matsukawa S, Sato M, Toba Y, Kurokawa S, Murata H. Antenna-coupled-electrode electro-optic modulator for converting two orthogonal-polarization field components simultaneously for 5G mobile systems. CLEO-PR 2020, August 2-6, 2020, Sydney, Australia, C8F-3.

7Gaa

Antenna measurement using precision antenna measurement technology and Radio over Fiber technology.

7G aa Co. LTD. (7th Generation in Automation and Antenna Measurement

CEO：Dr. Masanobu Hirose email: masa-hirose@7gaa.jp, **mobile: +70-8409-2886, TEL & Fax: +29-819-2174**

Product and consulting

1. Antenna near field to far field transformation software and consulting

- **Planer near field antenna measurement, Cylindrical near field antenna measurement, Spherical near field antenna measurement. (IEEE 1720-2012 – IEEE Recommended Practice for Near-Field Antenna Measurements.)**
- **Single cut near field antenna measurement**
- **Several cut near field antenna measurement**

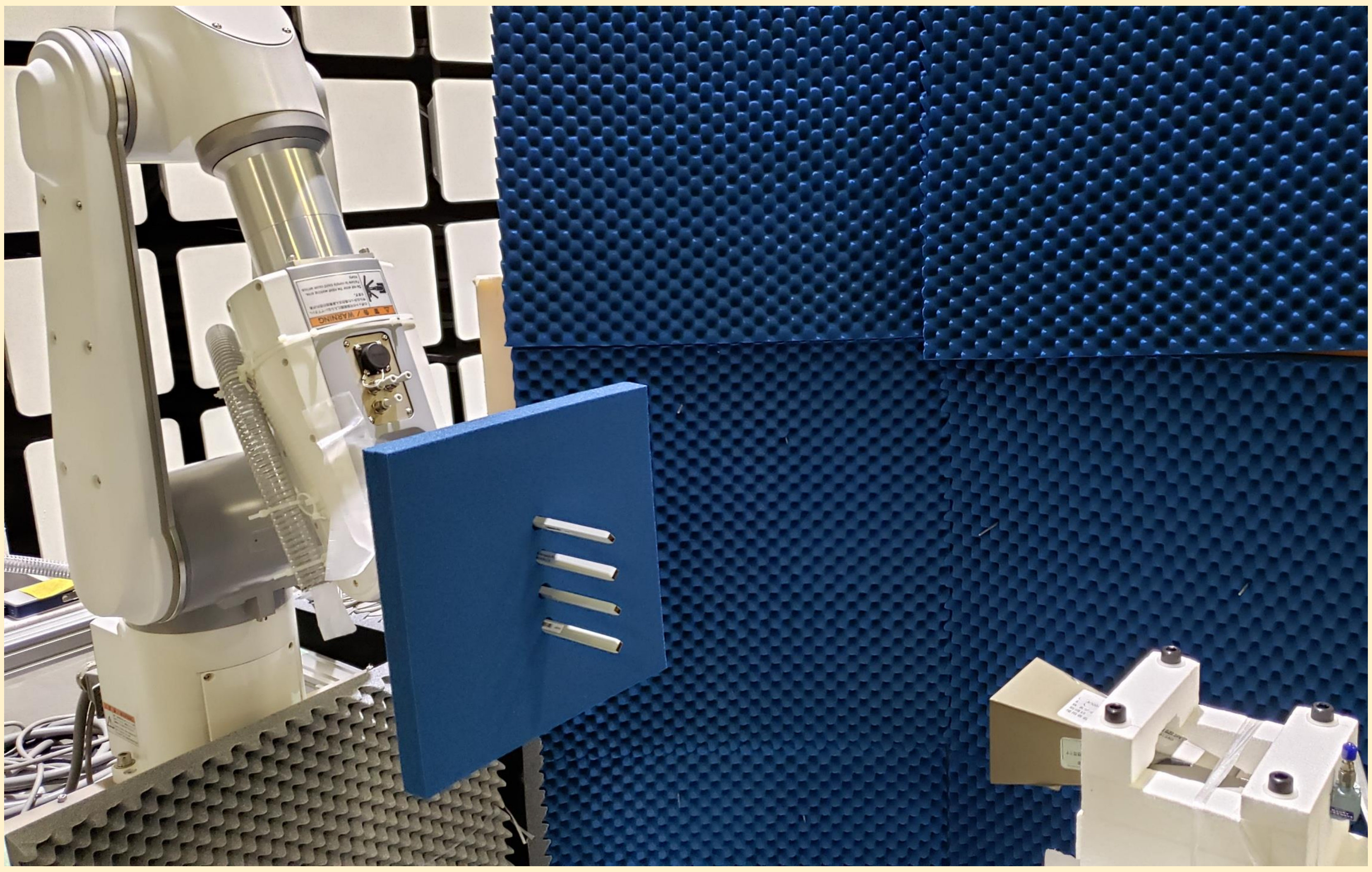

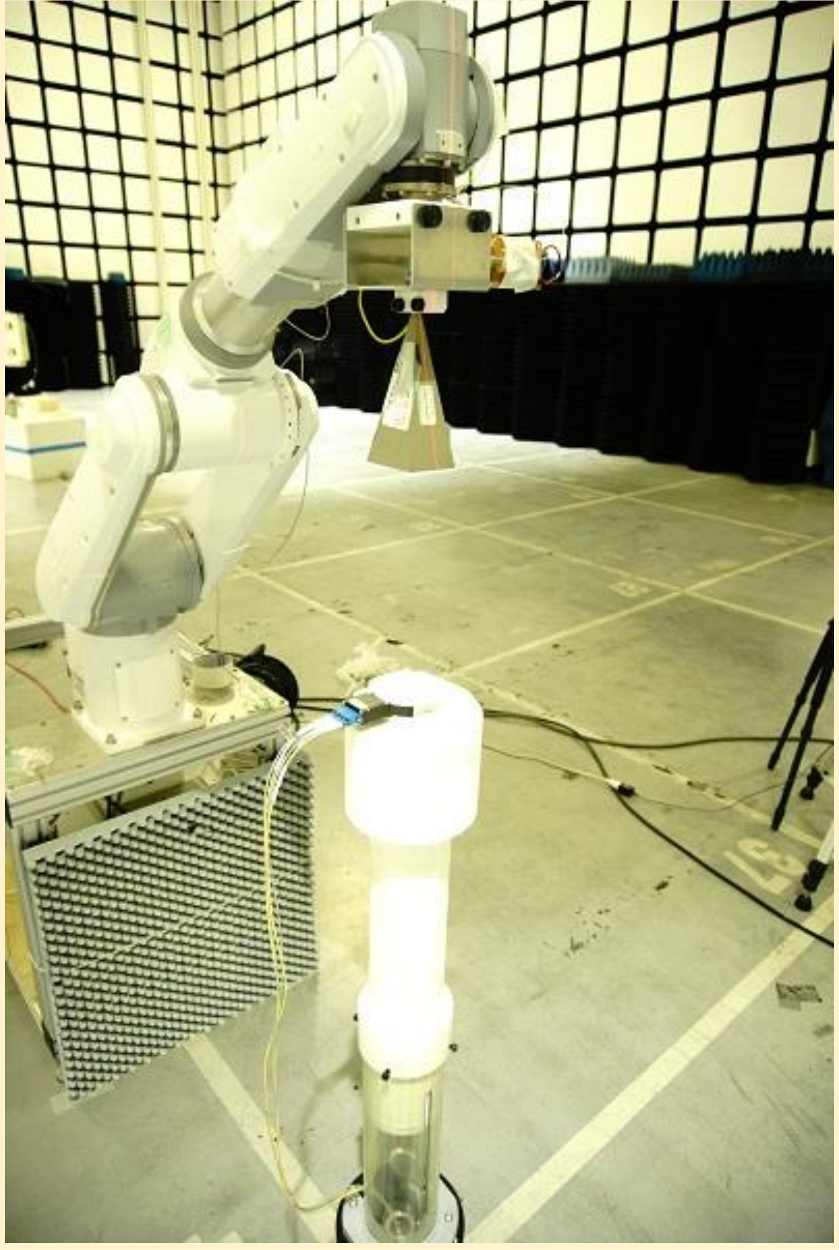

2. Antenna measurement consulting and uncertainty estimation consulting

3. Radio over Fiber devices for antenna measurement (IEC TR 63099-1:2017)

- **Optical reflection type EA modulator for 40 GHz (1550 nm, DC Bias= 0 V, No temperature control needed)**
- **VCSEL for 25 GHz, VCSEL for 30 GHz (850 nm)**
- **PD-TIA (1300 nm to 1550 nm), PD-TIA (850 nm)**

4. Port extender for Vector Network Analyzer (IEC TR 63099-1:2017)

You can measure S-parameter (S_{11}, S_{21}, S_{12}, S_{21}) using our system in full-2-port calibration

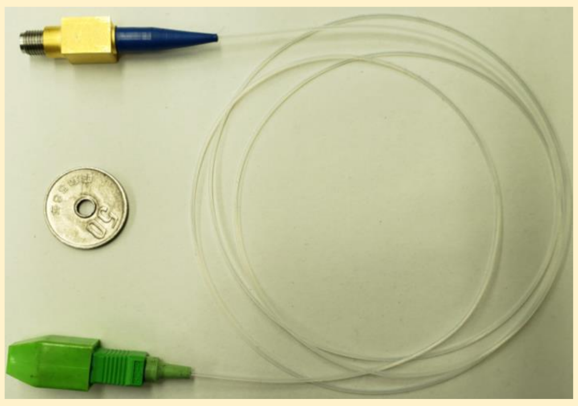

Optical reflection type EAM

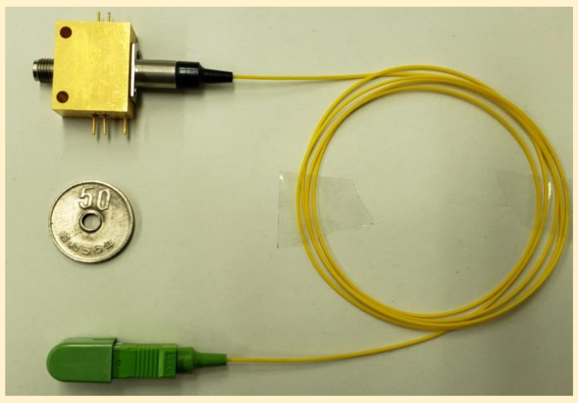

VCSEL and PDTIA
(using the same metal case)

IEC TC103 WG6 Japan National Committee

Scope and Structure

International standardization body for the electrical and electronic sectors.

Technical Committee 103:
Transmitting and Receiving Equipment for Radiocommunication
Working Group 6:
Radio-Over-Fibre Technologies

Development of international standards and technical reports related on RoF systems for wireless communication, radar, sensing, measurement technique, and other applications.

Chair: Seung-Hyun Cho (ETRI, Korea)
Secretary: Satoru Kurokawa (AIST, Japan)
WG6 Convener: Hiroyo Ogawa (NICT, Japan)

P-members: China , Germany , Italy, Japan, Korea, Pakistan, Poland, Romania, Russian Federation, Switzerland, UK

IEC TC103 Japan National Committee
Convener: Hiroyo Ogawa (NICT, Japan)
Secretary: Masafumi Yamamoto (Ministry of Internal Affairs and Communications, Japan)

Working Group 6 JNC
Head: Atsushi Kanno (NICT, Japan)
Secretary: Junichiro Ichikawa (Sumitomo Osaka Cement, Japan)

Published Standards and Technical Reports

International Standards
IEC 62801:2020 Measurement method of a half-wavelength voltage for Mach-Zehnder optical modulator in wireless communication and broadcasting systems
IEC 62802:2017 Measurement method of a half-wavelength voltage and a chirp parameter for Mach-Zehnder optical modulator in high-frequency radio on fibre (RoF) systems
IEC 62803:2016 Transmitting equipment for radiocommunication - Frequency response of optical-to-electric conversion device in high-frequency radio over fibre systems - Measurement method

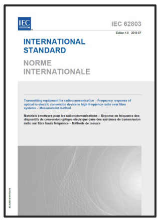
IEC 62803
INTERNATIONAL STANDARD
NORME INTERNATIONALE

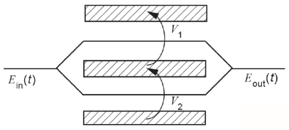

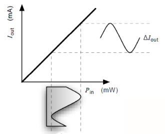

Technical Reports
IEC TR63098-1:2017 Radio-over-fibre technologies and their performance standard - Part 1: System applications of radio over fibre technology
IEC TR63099-1:2017 Radio-over fibre technologies for electromagnetic-field measurement - Part 1: Radio-over-fibre technologies for antenna measurement
IEC TR63099-2:2020 Radio-over-fibre technologies for electromagnetic-field measurement - Part 2: Radio-over-fibre technologies for electric-field sensing
IEC TR63100-1:2017 Radio-over-fibre technologies for spectrum measurement - 100-GHz spectrum measurement equipment


IEC TR 63099-2
TECHNICAL REPORT

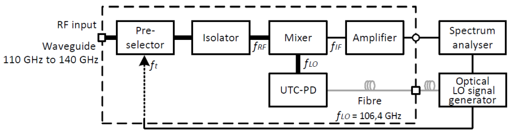

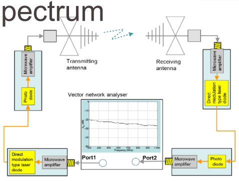

On-going Projects

300GHz Antenna Measurement by EO technique,
System application of short range radar system
RoF network for high-speed railway communication
RoF-based 5G indoor DAS system

and more

If interests, please join us.

Contact: Atsushi Kanno (NICT, Japan)
email: kanno@nict.go.jp

International
Electrotechnical
Commission

Leaflet

Anritsu Advancing beyond

電波伝搬測定に最適な ベクトルネットワークアナライザシステム

長距離を測定する画期的なVNA

ShockLine™ ME7868A
モジュールベクトルネットワークアナライザシステム
周波数範囲 :1 MHz ～ 8 GHz / 20 GHz / 43.5 GHz

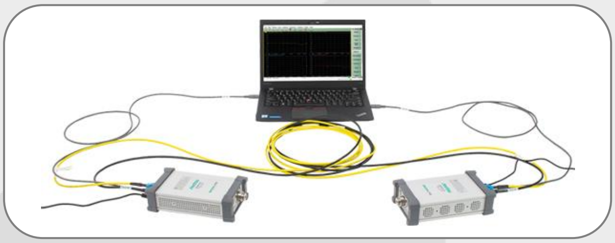

ポートの配置が自由なVNA

ME7868Aは、2台のMS46131A 1ポートUSBベクトルネットワークアナライザを使って2ポートVNAを構成し、ベクトルSパラメータ測定を実現したVNAです。1 MHzから8/20/43.5 GHzの3つの周波数で利用可能で、測定対象物に合わせた測定ポートの配置を可能にした非常にユニークな2ポート測定ソリューションを提供します。

主な特長：

- 測定ポートが独立した2ポートVNA
- 1MHz～8GHz, 20GHz, 43.5GHzの３つの周波数範囲
- 非常にコンパクトなパッケージ(縦192 mm×横107 mm×高さ54 mm)でDUTへ直接接続が可能
- 1台のWindows PCに2台のMS46131AをUSBケーブルで接続。互いのVNAに2本のPhaseLyncケーブル(光/電気)をつなぐだけで構成

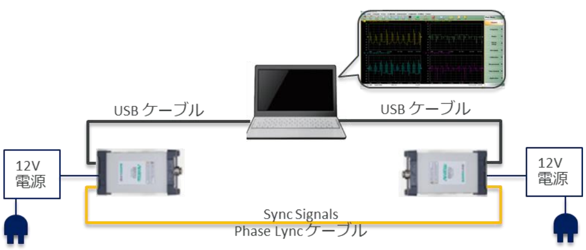

ME7868A接続例
(PhaseLyncケーブル:2 m、5 m)

長いテストポートケーブルによる伝搬測定の課題

伝搬測定ではアンテナ間の距離が離れており、アンテナまで長いテストポートケーブルが必要です。5Gなど高い周波数での測定では、ダイナミックレンジの広い高価なVNAが必要でした。

導波管を使用するケースもありますが、導波管はテストポートケーブルのような柔軟性がないので測定したい位置に置くことが難しくなり、シミュレーション結果との相関取りに工夫が必要になります。

【参考】5 m長さのテストポートケーブル損失
5.9 dB@6 GHz
15 dB@40 GHz
(3670K50A-2の損失から5 m相当に換算)

伝搬測定を容易に

ME7868Aは、小型な本体のためアンテナに直接接続することができ、測定器のダイナミックレンジを最大限に生かすことができます。測定ポートがそれぞれ独立しているため、測定したい位置にアンテナを設置することが可能です。

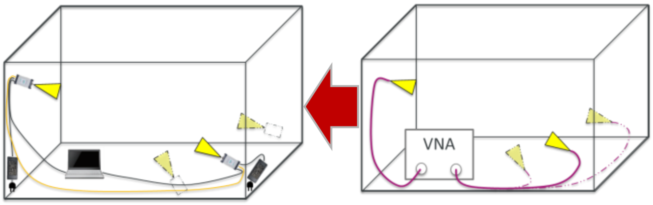

電波伝搬の測定方法　比較

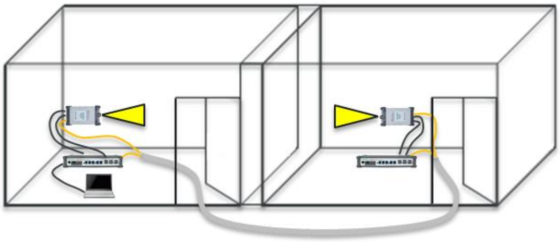

部屋間の伝搬測定例
ME7868A-xxx-25の使用

マルチパスの解析や直接波のみの測定に

タイムドメイン機能を使うことで、時間や距離に応じた応答を解析できます。
ゲート機能を使い直接波だけを取り出し、測定することも可能です。

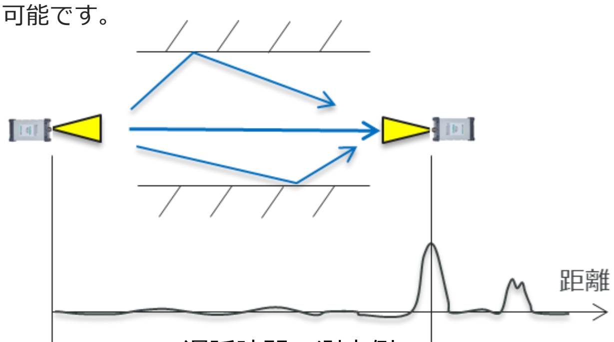

遅延時間　測定例

ME7868A

モジュールベクトルネットワークアナライザシステム

●テストポートケーブルを短くし、システム構成を簡単にするPhaseLyncテクノロジ

PhaseLyncケーブルは3種類(2 m、5 m、25 m)を標準で用意しています。25 m長さではUSBケーブルを延長するためのマルチファンクションエクステンダー 2台を含むPhaseLyncアクセサリーキットが添付されます。
PhaseLyncテクノロジは100 mのPhaseLyncケーブルにも対応しています。

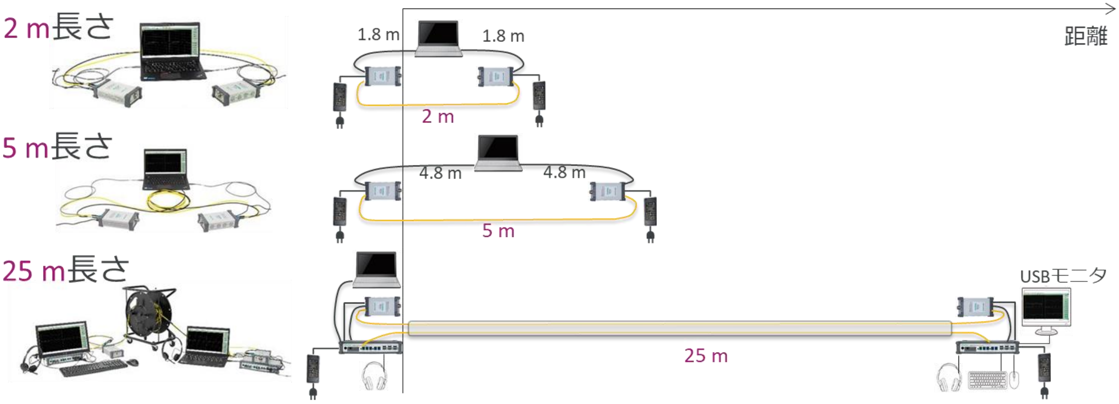

ME7868A 主な仕様：

周波数範囲	1 MHz ～ 8 GHz (オプション010), 1 MHz ～ 20 GHz (オプション020) , 1 MHz ～ 43.5 GHz (オプション043)
ポート出力パワー	High：0 dBm @ 1 MHz ～ 43.5 GHz， Low：-20 dBm @ 1 MHz ～ 43.5 GHz (代表値)
ハイレベルノイズ	振幅：0.009 dB@ 1 MHz ～ 8 GHz , 0.006 dB@ >8 GHz ～ 40 GHz , 0.006 dB@ >40 GHz ～ 43.5 GHz 位相：0.12 deg @ 1 MHz ～ 8 GHz , 0.1 deg@ >8 GHz ～ 40 GHz , 0.12 deg@ >40 GHz ～ 43.5 GHz
方向性（補正後）	42 dB @ 1 MHz ～ 10 GHz , 36 dB @ 10 GHz ～ 20 GHz , 32 dB @ 20 GHz ～ 30 GHz , 30 dB @ 30 GHz ～ 40 GHz , 28 dB @ 40 GHz ～ 43.5 GHz
掃引速度	230 µs/ポイント （代表値)

ShockLine™ ソフトウェア機能：

校正	伝送路： 同軸、マイクロストリップ、導波管　手法：OSL(Open/Short/Load), SST(Offset Short), SmartCal/AutoCal その他： エンベディング/デ・エンベディング機能
マルチチャンネル	1台のPCから最大2台のMS46131Aを制御可能、 2 ～ 16,001ポイント
レスポンス	反射周波数特性 (S11)
掃引タイプ	リニア、ログ、セグメント（周波数/インデックス、最大50セグメント）
表示グラフ	対数振幅、位相、群遅延、リニア振幅、実数、虚数、SWR、インピーダンス、スミスチャート(インピーダンス)、極座標
マーカ	12マーカ+ 1リファレンスマーカ（トレースごと) アドバンスドマーカ機能：マルチピーク、マルチターゲットサーチ、レンジサーチ、トラッキング
リミットライン	Pass/Fail, リップルテストリミット、50個のセグメンリミット（トレースごと）

型名	製品名
ME7868A-010-2	1 MHz-8 GHz 2ポートVNAシステム(2 mケーブル)
ME7868A-010-5	1 MHz-8 GHz 2ポートVNAシステム(5 mケーブル)
ME7868A-010-25	1 MHz-8 GHz 2ポートVNAシステム(25 mケーブル)
ME7868A-020-2	1 MHz-20 GHz 2ポートVNAシステム(2 mケーブル)
ME7868A-020-5	1 MHz-20 GHz 2ポートVNAシステム(5 mケーブル)
ME7868A-020-25	1 MHz-20 GHz 2ポートVNAシステム(25 mケーブル)
ME7868A-043-2	1 MHz-43.5 GHz 2ポートVNAシステム Extended-K(2 mケーブル)
ME7868A-043-5	1 MHz-43.5 GHz 2ポートVNAシステム Extended-K (5 mケーブル)
ME7868A-043-25	1 MHz-43.5 GHz 2ポートVNAシステム Extended-K (25 mケーブル)
他のオプション	
MS46131A-002	ローパスタイムドメイン機能（ME7868A-xxx-xには2セット必要です。）

アクセサリ

手動校正キット

SmartCal
(自動校正キット)

アンリツ株式会社　https://www.anritsu.com
計測器営業本部　営業推進部
TEL: 0120-133-099 / FAX: 046-296-1248
E-mail: SJPost@zy.anritsu.co.jp

SPEAG OPTICAL SOLUTION

OH4VNA System

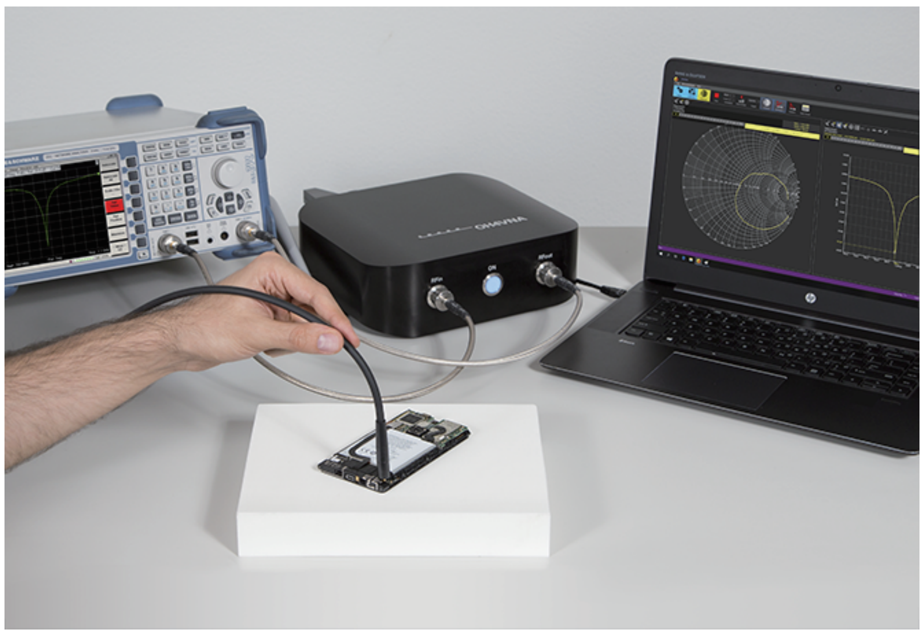

【概要】

小型アンテナの高精度 S11 パラメータ測定

最新のベクトルネットワークアナライザに対応

SIM4Life との連携

サードパーティ製マイクロ波回路設計ツールと連携

【仕様】

- OH4VNA オプティカルヘッド
  周波数範囲：500 MHz〜6 GHz
  RF ダイナミックレンジ：> 100 dB
  電気的サイズ：6×6 mm（シリンダー）
  機械的サイズ：直径 10 mm
  アンテナ相互接続：カプラー経由（Mini-SMP）
- OH4VNA リモートユニット
  OH 相互接続：TDSMU8 光相互接続
  VNA 相互接続：3.5mmRF コネクタ
  周波数範囲：10 MHz〜6 GHz

【アプリケーション】

- 携帯電話
- 補聴器、インイヤーデバイス
- 身に着けているデバイス
- 埋め込まれたデバイス
- バーコードリーダーなどのハンドヘルドデバイス

TDS SNI

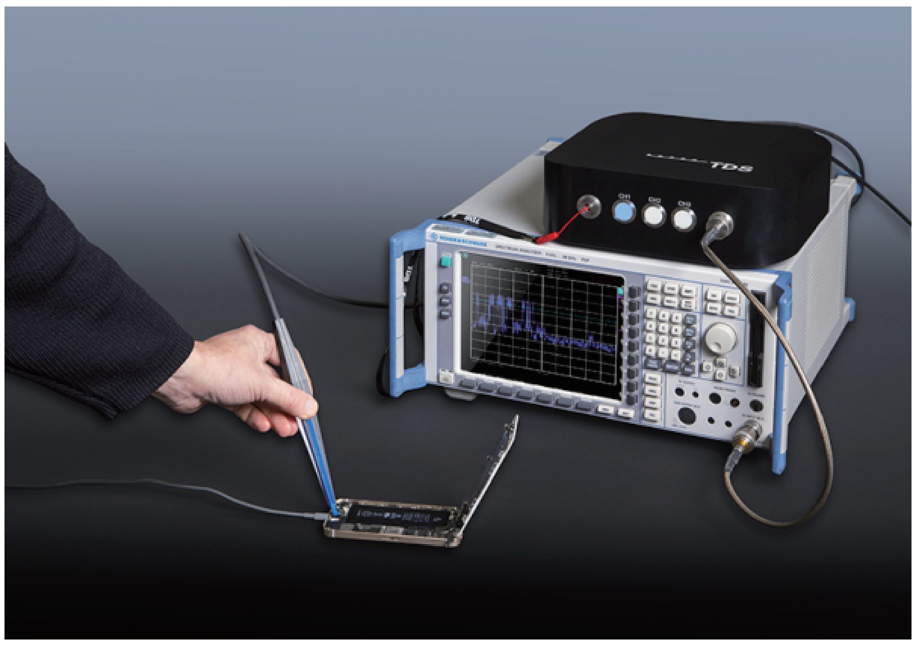

【概要】

時間領域センサー技術を使用して、
近接場 EMC / EMI / ESD スニッフィング用に
最適化されています。

【仕様】

- H1TDS SNI 磁場プローブ
  周波数範囲：10 MHz〜6 GHz
  ダイナミックレンジ：1 μ A/m-≥1A/ m（2 GHz）
  電界抑制：> 20dB（2 GHz）
  センサーサイズ：2×2 mm2　チップサイズ：4×4 mm2
- E1TDS SNI 電界プローブ
  周波数範囲：10 MHz〜6 GHz
  ダイナミックレンジ：0.3 mV /m-≥150V/ m
  センサーサイズ：2.8mm　チップサイズ：4×4 mm2

【アプリケーション】

- EM 過酷な環境での測定
- EMC / EMI / ESD 近接場定量測定
- EMC / EMI / ESD プレコンプライアンステスト
- その場基地局コンプライアンス測定

お問い合わせ

株式会社レスターコミュニケーションズ
第四営業部門 計測営業部 営業一課

〒141-0001　東京都品川区北品川 5-9-11 大崎 MT ビル
TEL：03-3445-2091 E-mail：info.web@restarcc.com

TDS RFoF1P and MED

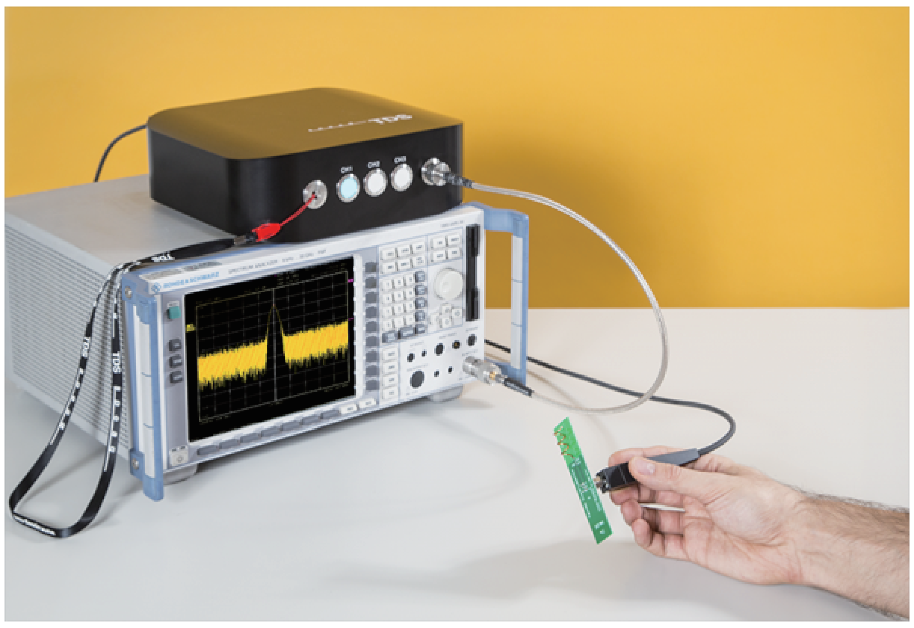

【概要】

アクティブフォトニック TDS 1 ポート RF-over-Fiber リンクシステムです。

小型のメディアコンバーター（SMA から光ファイバー）と標準の TDS リモートユニット（光ファイバー～ 3.5mm）で構成されています。

【仕様】

- TDS RFoF1P トランスデューサー
  周波数範囲：100 kHz～10 GHz
  ダイナミックレンジ：-120dBm-≥0dBm
  電気的サイズ：8×8×5 mm3
  トランスデューサーハウジングサイズ：16×16×90 mm3
- TDS リモートユニット
  入力：TDSMU8 光インターコネクト
  出力：3.5mmRF コネクタ
  周波数範囲：100kHz（10Hz）～10 GHz
  ダイナミックレンジ：> 130 dB
  P1dB：> 0dBm
  リターンロス：> 10 dB
  電源と制御：USB

【アプリケーション】

- 無線パフォーマンス
- アンテナ相関測定
- 信号と電力の整合性
- MRI 信号リンク
- EMP / ESD テスト

SIM4LIFE

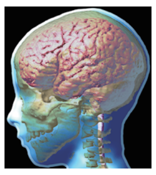

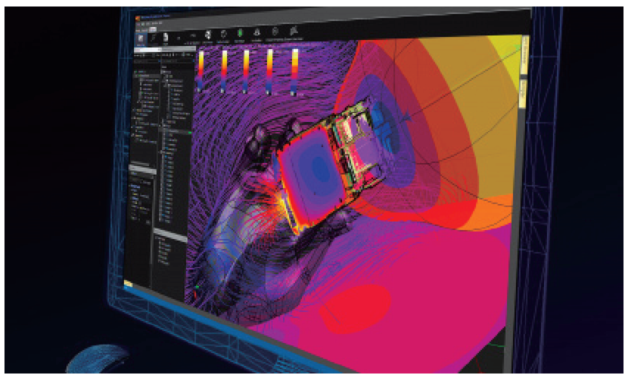

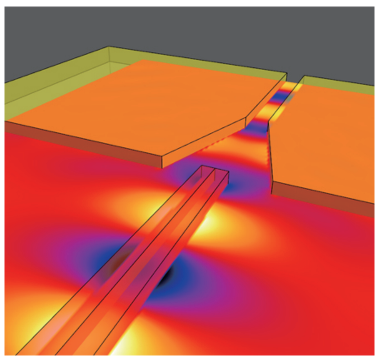

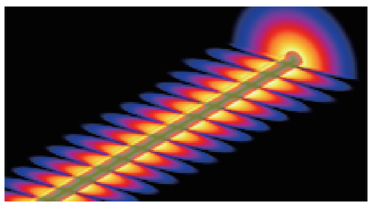

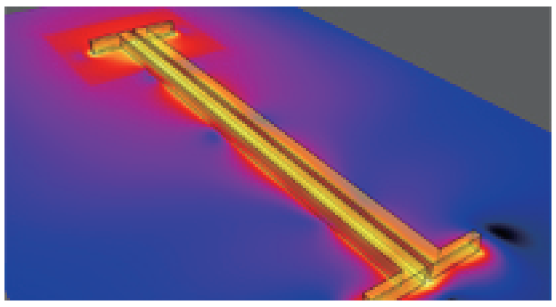

【概要】

- FDTD/FEM 計算ソルバーと高精度人体モデルを組み合わせた
  マルチフィジックスシミュレーター

【アプリケーション】

- 電子機器・アンテナ（5G ソリューション）・EMC
- マイクロ波・人体通信（BAN）・自動車、航空、他・WPT
- 人体通信・電磁波安全性評価・レーダーなどミリ波解析

【オプティカル アプリケーション】

- 光リング共振器の設計
- 光導波路とフィルターの分析
- フォトニック結晶導波路の曲がりの分析
- フォトニック結晶パワースプリッターの分析
- デジタルマイクロミラーアレイの設計
- イメージセンサー設計の最適化
- CMOS および CCD イメージセンサーのモデリング
- ナノ粒子とプラズモン共鳴構造のモデリング

Issue date: November 24, 2021
IEICE Technical committee on Photonics-applied Electromagnetic Measurement

PEM 2021

4th International Workshop on **P**hotonics applied to **E**lectromagnetic **M**easurements

Technical committee on Photonics-applied Electromagnetic Measurement

https://www.ieice.org/~pem/